MAGNETIC PHASES OF THE FRUSTRATED SPIN DIMER COMPOUND $Ba_3Mn_2O_8$

A DISSERTATION
SUBMITTED TO THE DEPARTMENT OF APPLIED PHYSICS
AND THE COMMITTEE ON GRADUATE STUDIES
OF STANFORD UNIVERSITY
IN PARTIAL FULFILLMENT OF THE REQUIREMENTS
FOR THE DEGREE OF
DOCTOR OF PHILOSOPHY

Eric C. Samulon
December 2010

This dissertation is online at: http://purl.stanford.edu/qh243cb9446

I certify that I have read this dissertation and that, in my opinion, it is fully adequate in scope and quality as a dissertation for the degree of Doctor of Philosophy.

Ian Fisher, Primary Adviser

I certify that I have read this dissertation and that, in my opinion, it is fully adequate in scope and quality as a dissertation for the degree of Doctor of Philosophy.

Malcolm Beasley

I certify that I have read this dissertation and that, in my opinion, it is fully adequate in scope and quality as a dissertation for the degree of Doctor of Philosophy.

Zhi-Xun Shen

Approved for the Stanford University Committee on Graduate Studies.

Patricia J. Gumport, Vice Provost Graduate Education

This signature page was generated electronically upon submission of this dissertation in electronic format. An original signed hard copy of the signature page is on file in University Archives.

Abstract

Spin dimer compounds are based on pairs of spins with antiferromagnetic exchange. At low fields the ground state is a product of singlets, with excited triplet states at higher energies. Application of a magnetic field closes the spin gap between the excited triplet state and singlet state. Interactions between dimers broaden the triplet bands, such that above a critical field where the minimum of the triplet band crosses the singlet, long range magnetic order (LRMO) can arise. The ordered states can take several novel forms, including a spin superlattice or a Bose-Einstein condensate of magnons, depending upon the spin Hamiltonian describing the system.

$Ba_3Mn_2O_8$ is a spin dimer system based on dimers of $S = 1$, $3d^2$, Mn^{5+} ions arranged on a triangular lattice. A pair of antiferromagnetically linked $S = 1$ ions has total spin 0, 1 or 2, leading to, in zero field, excited quintuplet states in addition to the excited triplet states above the singlet ground state. The triangular lattice is composed of vertical dimers on hexagonal layers which are stacked according to an 'ABC' structure. In this thesis, I describe the results of experiments which probed this system via different thermodynamic measurements of single crystals, revealing at least three novel ordered states.

Measurements of heat capacity, magnetocaloric effect, torque magnetometry and magnetostriction revealed significant anisotropy in the singlet-triplet regime, with a single ordered state observed for fields along the easy c axis and two states observed for fields away from that direction. Analysis of the minimal spin Hamiltonian yields candidate phases for the canted antiferromagnetic order observed, including incommensurate order close to the archetypal 120° order for triangular systems as well as modulated order for fields away from the c axis.

The triplet-quintuplet regime was probed via heat capacity, magnetocaloric effect and magnetization measurements, the first experiments to probe such ordered states of a spin dimer compound. A significant asymmetry in the quintuplet condensate was revealed in both the magnetization and the phase boundary. This asymmetry is understood as a consequence of zero point phase fluctuations, which are absent at the saturation field but present everywhere else.

Finally, the effect of disorder in this spin dimer compound was studied by substitution of non-magnetic $S = 0$ $3d^0$, V^{5+} ions for the $S = 1$, $3d^2$, Mn^{5+} ions in $Ba_3(Mn_{1-x}V_x)_2O_8$. This work was motivated in part by theoretical predictions that substitution of non-magnetic species on a square lattice of dimers would result in a low-temperature ordered magnetic state, for which interactions between the unpaired magnetic moments is mediated by short range correlations of the background singlet ground state. We do not find any evidence for such a state down to 50 mK. Rather, the magnetic entropy is progressively removed over an extended range of temperature, from $\sim$2 K down. The temperature and doping dependence of the heat capacity do not conform to expectations for a spin glass, leading us to suggest that $Ba_3(Mn_{1-x}V_x)_2O_8$ manifests a random singlet state for the range of compositions and temperatures studied.

Acknowledgments

My journey doing this dissertation work has required lots of help along the way. I've done work at Stanford and at labs across the country and around the world and without the help I received from people in all those places I couldn't accomplished much of what I've done.

I will first and foremost thank my advisor Ian. He's been patient with me through many long years, and his help has been invaluable. From the beginning, he has been completely as available I could have reasonably expected. Choosing to work in his group was the most important decision I made in grad school and it was the right one.

I've also been in the Fisher group since a very early time meaning I've met most of the people who passed through the group who have all helped me in many different ways. Max has helped me the most of anyone - really far and above what could be expected from undergrad. When he wasn't talking about baseball or Bob Dylan he did all the tasks I asked of him, including the crystal synthesis stuff I tried to avoid, without complaint. I took over my project from Suchitra, and she and her undergrads Philip and Peter gave me quite a bit of my basic spin dimer technique knowledge. Yana was really helped me a lot by showing me many of the ropes of the lab, especially the basic stuff that I should have known but didn't. Kyun was around for quite a few years and always fun to talk with in lab. Nancy helped me learn the SQUID and was around a lot to help answer lots of questions . I overlapped the longest with Ann so we had a lot that we worked on together, including fixing the PPMS too many times to count. Jiun-Haw was the first younger student but he also helped with lots of lab stuff and particularly computer questions. James has always

been fun to talk to and really knowledgeable outside source. Also younger students like Felipe, Hsueh-Hui, and Paula have been fun to talk to and meet.

I've been helped by many different people in GLAM, and they make things much more bearable. Starting first with the main admins I worked with - Cyndi, Angela, and Stephen (who is sorely missed) all helped me when I needed to be reimbursed for a trip, or when I needed to know some account info, or even if I just needed to borrow their fax machine. Other Stanford staff have been so helpful, like Lily and Sybille giving wanting to have a talk, or Roberta helping with the projector, or Corrina helping do those annoying SLAC purchases. Bob always treated me well (and I enjoyed his jelly beans) when working on microprobe for me. Arturas was always obliging in helping when I was having problems with the XRD machines. Mark has always been so great, sending all those samples even with all the annoying paperwork that comes with them. Also all the other students, who have helped with physics questions or even better with distractions from physics questions, including Wei-Sheng, Felix, Steve, Brian, Eugene, Guillaume, Lisa, Clifford and many others on down the list.

Much of my research has been done away from Stanford, and many people have helped make those trips (mostly) successful. The first collaborator I worked extensively with was Zahir at the Advanced Photon Source at Argonne National Lab. When I went out first to Chicago I probably said and did quite a few stupid things out of ignorance and he never laughed at me. He also worked very hard, beam time hours, which I'm sure were very tasking consider his baby at home. Cristian was the most helpful and obliging theorist this experimentalist could ask to work with. He was patient in explaining so much of the calculations that must have been trivial for him - really without him there could not have been much theoretical understanding for most of my work. I did lots of experiments at the National High Magnetic Field Lab, both in Tallahassee and Los Alamos, and there were many people who helped me. I worked extensively with Marcelo, mostly in Tallahasse and he was always ready to talk about spin dimers or drink a beer. Ross was always very helpful in Los Alamos even with those long drives from Santa Fe. Yoshi was fun to talk and work with and

even hang out with a little in Los Alamos. Vivien very nicely did the VSM measurement for me in addition to answering a few more different experimental questions I had. Luis and Youn-Jo were good working companions, even though something bad always seemed to be happening to Luis. Eric and Tim always helped the measurements run smoothly down in Tallahassee. Matt and Mark from Oak Ridge were really fun guys to hang out and they explained a lot about how neutron studies worked. George was very nice to work with, and he gave good advice beyond physics which was much appreciated; I'm still a bit disappointed the dilatometry results never got written up.

It would not be possible to finish all the work for this thesis without the support of people away from the lab. My friends too long to list have made life fun, being a good distraction from my project. My grandparents were always very proud, and my grandfathers in particular set amazing examples to follow. My brother and sister were great connection back home (at least when they were in the country). And my parents were extermely encouraging and helped through the rough patches I encountered making it through this long work.

Finally, I want to thank my wife, Monica. She has been with me since the beginning of grad school, and having that happy face to come home to really made it fun. I am so happy we get to spend the rest our lives together.

Contents

List of Figures

Chapter 1

Introduction

1.1 Motivation

Long range magnetic order is an important and commonplace phenomenon, frequently found in nature, which underlies many everyday applications. For instance, the familiar horseshoe magnet is an example of ferromagnetism, in which all the magnetic moments of a material align to create a large combined external field which can be felt by other nearby magnets. Ferromagnetic materials are used in a wide array of different applications, from the magnetic strips on credit cards which store the personal information of the cardholder, to the basic compass, which comprises a magnetized arrow that aligns with the earth's magnetic field to point north. A slightly different example of long range magnetic order is found in the layered systems which exhibit giant magnetoresistance (GMR). These materials are designed in such a way that thin ferromagnetic layers align naturally in alternate directions. For a sufficiently large external magnetic field, the magnetization of each layer aligns in the same direction, altering the resistance of the device. GMR read heads have been widely used in hard disk drives since the mid 2000's. More recently, variants based on tunnel junction have been used to store as well as read data.

Spin dimer compounds provide a pathway to novel magnetically ordered states. In the simplest case for these compounds, strong antiferromagnetic exchange between pairs of $S = \frac{1}{2}$ spins (dimers) leads to a groundstate that is a product of singlets with

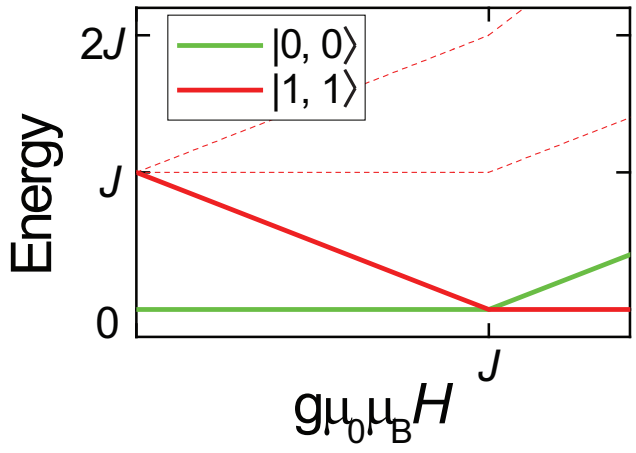

Figure 1.1: Energy spectrum of an isolated spin dimer composed of pair of $S = \frac{1}{2}$ magnetic ions with antiferromagnetic exchange J. Singlet state is solid green line and $S^z = 1$ triplet states is solid red line. Including interactions between dimers causes the triplet lines to broaden into bands, such that as the $S^z = 1$ triplet band crosses the singlet state long range magnetic order can arise.

excited triplets. Application of a magnetic field splits the excited triplet states that are delocazed due to the interdimer exchange due to the basic Zeeman interaction (see Figure 1.1). Exchange between dimers broadens the triplet bands, and under specific conditions long range magnetic order can arise above the critical field where the minimum of the triplet band crosses the singlet band.

A useful analogy can be drawn between a spin dimer system at elevated magnetic fields and a lattice gas of hardcore bosons [1]. In this equivalence a singlet constitutes an empty site while a $S^z = 1$ triplet constitutes an occupied site, with the hardcore repulsion term maintaining no more than one $S^z = 1$ triplet on a given site. In such an analogy the effective J^{xy} exchange between dimers becomes in bosonic language a hopping term, and thus the kinetic energy, while the effective J^z exchange between dimers becomes a nearest neighbor repulsion term, and thus the potential energy. Depending on the interplay between these terms and the local geometry, different novel ordered states can arise [2].

If the potential energy of the system dominates, then the $S^z = 1$ triplets will try to minimize the repulsion term. This is accomplished by forming a spin crystal, in

which $S^z = 1$ triplets crystallize into a spin superlattice at a fractional filling value. In such a case, the magnetization would exhibit multiple magnetization plateaus as successive superlattices are formed for different fractional filling values. Such a state has been observed in the Shastry-Sutherland compound $SrCu_2(BO_3)_2$, for which experiments have revealed several successive magnetization plateaus [3], the spin-structure of which has been determined by NMR measurements [4].

If alternatively the kinetic energy dominates over the potential energy then canted antiferromagnetic order can arise. In such states the $S^z = 1$ triplets are delocalized and each site supports a coherent superposition of singlet and $S^z = 1$ triplet states. $TlCuCl_3$ is a well studied example of such a state, for which canted order develops above 5.7 T at low temperatures [5, 6, 7, 8]. If the spin-Hamiltonian describing a material has a U(1) symmetry for the moments in the plane perpendicular to the field then the canted antiferromagnetic order is a direct realization of a Bose-Einstein condensate (BEC) of magnons [9]. $BaCuSi_2O_6$ is an example of a BEC of magnons [10, 11, 12]; intriguingly, studies of the system revealed dimensional reduction to a transition in the 2D BEC class near 0 K, which was attributed to geometric frustration [13].

One further possibility has been theoretically predicted, in which the interplay between the kinetic energy, potential energy and the lattice lead to a spin supersolid. In this case, for specific field ranges, a spin crystal superlattice forms at a fractional filling value while a magnon BEC superfluid fills in the vacancies [14]. Although this state has been the subject of considerable theoretical investigation, to date no system has been found with such order.

While it is clear that spin dimer compounds can provide access to various kinds of novel ordered states, these systems also have several specific characteristics that differentiate them from simple magnets. First, the entire phase diagram can be explored with the simple tuning parameter of an external magnetic field, in contrast to many other quantum magnets. Specifically, as will be shown in the theory section, the external magnetic field acts as a chemical potential for the triplets, such that the material can be tuned through the quantum critical point separating the quantum paramagnetic singlet state (characterized by short range correlations but no long

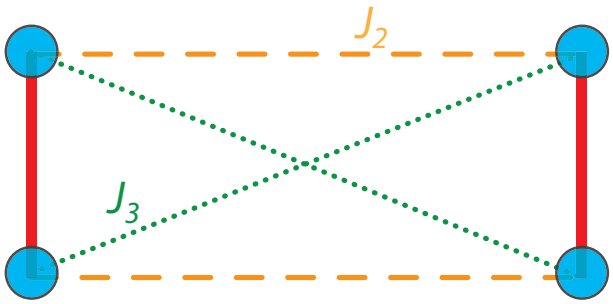

Figure 1.2: Schematic diagram showing interdimer exchange directly (J_2) and diagonally (J_3) across between dimers. Magnetic ions shown in blue connected by intradimer exchange shown in thick red line. Depending on the strength of J_2 and J_3 the effective exchange between dimers can be Heisenberg, Ising or xy-like, which will determine which of the various possible forms of long range order will develop for a lattice of dimers.

range order) to the ordered magnetic state with broken symmetry.

A second intriguing characteristic of spin dimer compounds is that highly anisotropic effective exchanges can be engineered between dimers. This is significant because J^{xy} and J^z component of the effective exchange between dimers set the kinetic and potential energy, respectively, of the $S^z = 1$ triplets, and thus determine the exact form of the ordered states. For instance, in the schematic shown in Figure 1.2, each spin of neighboring dimers has two interdimer exchanges, J_2 directly across between dimers and J_3 diagonally across between dimers. The resulting effective exchange between dimers is given by J^{xy}_{eff}=$J_2 - J_3$ and $J^z_{eff} = J_2 + J_3$. The theoretical predictions of a spin supersolid hinge on this ability to generate an anisotropic exchange with a nearly zero J^{xy}_{eff} between dimers. In such a manner multiple Heisenberg interactions for each magnetic ion can combine to create Heisenberg, Ising or xy-like effective exchanges between dimers, while preserving a weak spin-orbit coupling.

A final important characteristic of spin dimer systems is that they are protected from symmetric anisotropies. Symmetric anisotropies, such as dipole-dipole interactions, can constrain moments by making certain directions energetically unfavorable for the spins to point along relative to the other more favorable directions. This will break the U(1) symmetry and by extension the magnon BEC language for the ordered states. However, in spin dimer compounds symmetric anisotropies cannot

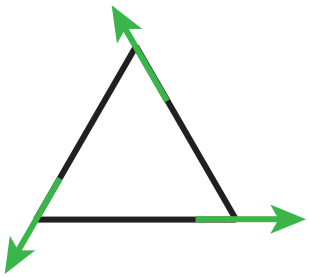

Figure 1.3: Schematic diagram showing how geometrically frustrated triangular lattices composed of Heisenberg spins with antiferromagnetic exchange have a non-collinear 120° groundstate.

directly connect two states of opposite symmetry, and thus cannot directly connect singlet and triplet states (or triplet and quintuplet states). Symmetric anisotropies instead enter the effective spin Hamiltonian in second order; thus their constraints on the ordered states are much smaller and the U(1) symmetry will be preserved to a much lower energy scale.

In this thesis, I describe the results of experiments probing a new spin dimer compound $Ba_3Mn_2O_8$, of particular interest because the dimers occupy a geometrically frustrated lattice, and because the Mn ions carry a higher spin of $S = 1$.

1.2 A New Spin Dimer Compound: $Ba_3Mn_2O_8$

$Ba_3Mn_2O_8$ has several characteristics that make its ordered states unique among currently known spin dimer compounds: a triangular, frustrated structure; magnetic Mn^{5+} ions with $S = 1$, leading to additional quintuplet states; and finally an easy axis single ion anisotropy. In this section I will discuss these unique characteristics as well as a short summary of the previously studies of this system.

The first significant facet of $Ba_3Mn_2O_8$ is its triangular structure. Antiferromagnetic exchange on a triangular lattice leads to geometric frustration, wherein all of the microscopic exchanges cannot be simultaneously satisfied. The classical solution to a Heisenberg antiferromagnet on a triangular lattice with only nearest-neighbor interactions is the well-known 120° structure (Fig. 1.3). In this case, the main effect

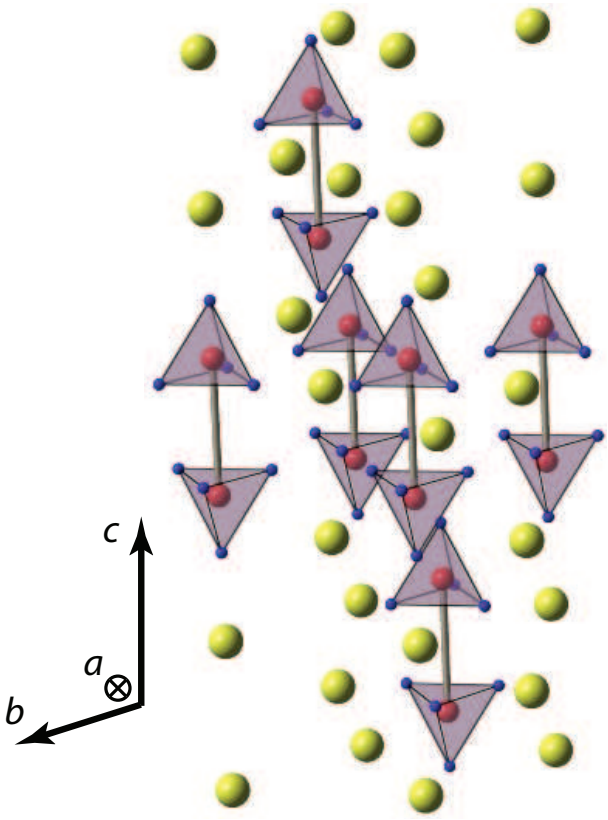

Figure 1.4: Crystal structure of $Ba_3Mn_2O_8$ showing 'ABC' stacking. Red, blue and yellow spheres are Mn, O and Ba ions, respectively, while grey pyramids are MnO4 tetrahedra. Bonds show the Mn dimers, separated 3.985 Å.

of the frustration is simply to produce a non-colinear structure. In an early attempt to find the groundstate of the two-dimensional quantum triangular antiferromagnet, Anderson proposed the Resonating Valence Bond (RVB) spin liquid state [15]. Subsequent theoretical work has indicated that for the simple case with only nearest neighbor interactions the classical solution is in fact stable against quantum fluctuations, but with a much reduced ordered moment [16, 17]. Other models corresponding to more complex lattices and interactions are still the subject of intense theoretical investigation [18]. This thesis will analyze the novel ways that geometric frustration is relieved in the ordered states of a spin dimer system.

$Ba_3Mn_2O_8$ has a rhombohedral $R\bar{3}m$ structure with hexagonal lattice parameters

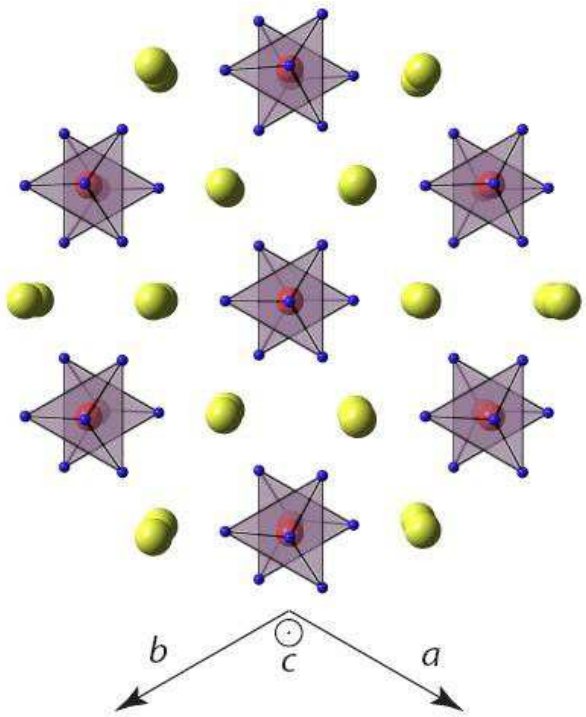

Figure 1.5: Crystal structure of $Ba_3Mn_2O_8$ showing single hexagonal plane. Red, blue and yellow spheres are Mn, O and Ba ions, respectively, while grey pyramids are MnO4 tetrahedra.

of $a = 5.71$ Å and $c = 5.71$ Å [19]. Each hexagonal plane is decorated by vertical dimers which are staggered according to an 'ABC' structure, such that there is geometric frustration both within a single plane and between planes (see Fig. 1.4). The dimers are composed of Mn ions in MnO_4^{3-} distorted tetrahedral coordination, where the Mn-O bond length is shorter to the apical O than to the planar oxygens. The bases of the stacked MnO_4^{3-} tetrahedra both face one another and are rotated 180° with respect to each other (see Fig. 1.5). These stacked Mn ions which form the dimer are separated by 3.985 Å. Each Mn ion has six next nearest neighboring in-plane Mn ions 5.711 Å away; the Ba ions act as spacers both in plane and between planes. Each dimer sits either directly above or below the center of a triangle of Mn ions from an adjacent layer, leading to additional frustrated pathways between planes. The distance between nearest and next nearest neighboring Mn ion on adjacent layers is 4.569 Å and 7.313 Å, respectively.

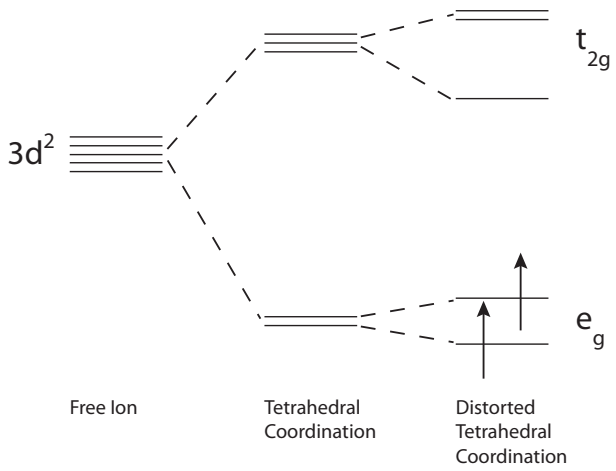

Figure 1.6: Crystal field splitting of $Ba_3Mn_2O_8$ showing how the two spins of the $3d^2$ Mn^{5+} ion are in the e_g states of the distorted tetrahedral coordination.

There is a center of inversion symmetry at the midpoint of the dimer between the Mn ions of the dominant exchange. This crucial symmetry precludes any Dzyaloshinskii-Moriya interaction between those spins. There are several additional symmetries, including a center of inversion symmetry at the midpoint between nearest neighboring Mn ions on adjacent layers and a mirror plane at the midpoint of the next nearest Mn ions in plane, which further constrain possible Dzyaloshinskii-Moriya interactions between Mn ions.

The Mn^{5+} ions of this compound have a electron configuration of $3d^2$, which in this crystal field coordination leads to total spin $S = 1$. The crystal field diagram for a $3d^2$ ion in a distorted tetrahedral environment is shown in Fig. 1.6. The two spins are in the split e_g orbital, which has quenched the orbital contribution to the moment, making the total spin $S = 1$. This larger spin allows for a dimer to have total spin $S = 2$ (quintuplets) in addition to the previously considered total spin states of $S = 1$ (triplets) and $S = 0$ (singlet). The same interactions that broaden the triplet band also broaden the quintuplet band, and for fields above those required to saturate the $S^z = 1$ triplet states there will be an additional critical field for which the $S^z = 2$ quintuplet states start to cross the triplet states (see Fig. 1.7). Under nearly the equivalent energetics as in the lower field regime, new ordered can arise consisting of

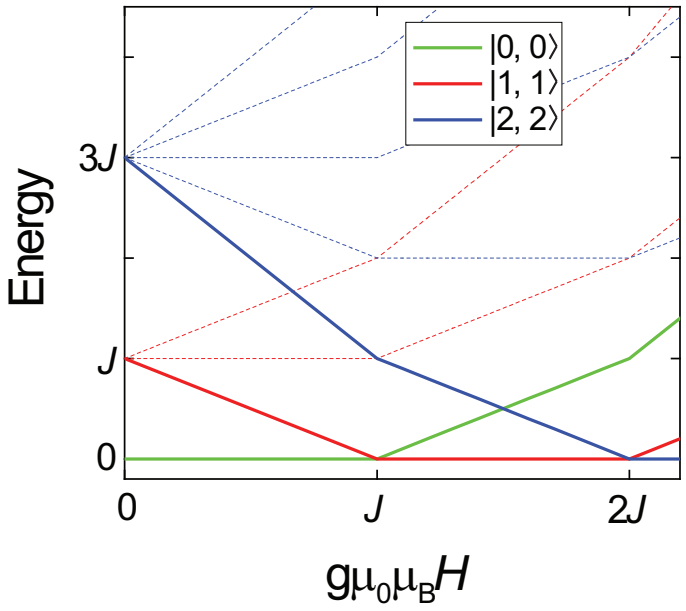

Figure 1.7: Energy spectrum for dimer composed of pair of $S = 1$ magnetic ions with antiferromagnetic exchange J. Singlet state is solid green line, $S^z = 1$ triplet states is solid red line and $S = 2$ quintuplet state is solid blue line.

a coherent superposition of quintuplets and triplets..

Only one previous spin dimer compound with $S = 1$ has been studied, the organic biradical magnet F_2PNNNO [20]. That compound is composed of a strongly ferromagnetically linked spin $\frac{1}{2}$ pair linked antiferromagnetically to another pair such that it acts as a spin 1 dimer [21, 22]. Magnetization measurements on that system showed two separate ranges of linearly increasing magnetization, first between 9 T and 15 T as the $S^z = 1$ triplet band is populated, then between 25 T and 29 T as the $S^z = 2$ quintuplet band is populated.

The total spin of $S = 1$ for each Mn ion also leads to a single ion anisotropy. Previously studied spin dimer compounds have been composed of ions of spin $S = \frac{1}{2}$, which by Kramer's theorem cannot have a single ion anisotropy. This symmetric single ion anisotropy will enter the effective Hamiltonian to second order as previously discussed.

Previous thermodynamic studies of the magnetic properties were performed on polycrystalline $Ba_3Mn_2O_8$. These studies revealed a spin gap in $Ba_3Mn_2O_8$ of $H_{c1} \sim$

9 T [23]. Further studies revealed a magnetization which rises approximately linearly with field from H_{c1} until the eventual triplet saturation field is reached at $H_{c2} \sim$ 26 T [24]. Above H_{c2} there is a plateau for which the system is fully in the triplet state. This plateau extends until the minimum of the quintuplet band at $H_{c3} \sim 32$ T above which there is a second region of linearly increasing magnetization as the quintuplet band is filled, saturating at $H_{c4} \sim 48$ T. Heat capacity measurements of polycrystalline samples revealed tantalizing evidence for two phase transitions in the singlet-triplet regime [25]. Initial calculations of the exchange pathways predicted that this compound falls into the canted antiferromagnetic ordering class where the kinetic energy dominates over the potential energy. This thesis contains the first studies on single crystal $Ba_3Mn_2O_8$, where the effects of the anisotropy are observed and the full phase diagram is established, including the first direct observation of triplet-quintuplet ordered states in a spin dimer system.

1.3 Layout of this Thesis

This thesis will follow the following outline: Chapter 2 contains the material and theoretical background, first detailing the relevant microscopic interactions of $Ba_3Mn_2O_8$, then outlining the energetics of an isolated dimer before finally determining the form of the effective interaction and the relevant second order processes. Chapter 3 contains the crystal synthesis and growth techniques used and single crystal characterization details. Chapter 4 contains the experimental techniques, first detailing the different magnets used to attain high fields and then the different thermodynamic measurements performed. Chapter 5 contains the results of experiments which probed the singlet-triplet ordered states of $Ba_3Mn_2O_8$ and a discussion of those results. Chapter 6 details the results of measurements of the triplet-quintuplet ordered states in this system. Chapter 7 concerns the experiments which probed the ground state of $Ba_3(Mn_{1-x}V_x)_2O_8$ at low fields. Finally, chapter 8 summarizes the results provided here. There are three additional appendices. Appendix A contains a derivation of the triplet dispersion which was utilized in the analysis of inelastic neutron scattering studies (INS) to determine the relevant exchange values of this system [26, 27, 28].

Appendix B contains a derivation of the energy spectrum for a system composed of two spins with exchange and single ion anisotropy. Appendix C contains preliminary studies which probed the singlet-triplet ordered states of $Ba_3(Mn_{1-x}V_x)_2O_8$.

The results presented in this have been published in several references [29, 30, 31, 32]. Additional measurements performed by collaborators on crystals grown as part of this thesis have also been published [26, 27, 28, 33, 34].

Chapter 2

Theory

This chapter will detail the theoretical underpinning of spin dimers and the specific energetics of $Ba_3Mn_2O_8$. First I will outline the basic features of an isolated dimer. Then I will describe the relevant interactions in the system and express the spin Hamiltonian. Finally I will demonstrate the transformation from the individual magnetic ion basis to the dimer basis for $Ba_3Mn_2O_8$ with the use of pseudospins. A crucial part of the transformation is developing the effective exchanges which are necessary to understanding the phase diagram shown later in this thesis.

2.1 Isolated Spin Dimer Comprising $S = 1$ Spins

Isolated spin dimer systems are conceptually simple and illustrate many of the basic properties of interacting spin dimer systems. In this section I will develop several basic thermodynamic properties of the isolated $S = 1$ spin dimer system which are to varying degrees applicable to the interacting dimer system of this work, $Ba_3Mn_2O_8$.

Antiferromagnetic exchange J within an isolated spin dimer composed of two $S = 1$ ion leads to a singlet groundstate with a gap of J to the three excited triplet states and a second gap of $3J$ to the five excited quintuplet states (Fig. 1.7). Application of a magnetic field causes the spin gap between the singlet and the $S^z = 1$ triplet state (as well as the gap between the singlet and the $S^z = 2$ quintuplet state) to decrease. At a critical field of $H_c = J/g\mu_0\mu_B$ the singlet state and the $S^z = 1$ triplet state

become degenerate, and as fields increase above H_c the $S^z = 1$ triplet state is the nondegenerate groundstate. Above H_c the gap between the $S^z = 1$ triplet groundstate and the excited $S^z = 2$ quintuplet state decreases as field is increased until a second critical field $H_c' = 2J/g\mu_0\mu_B$ where the $S^z = 1$ triplet state and the $S^z = 2$ quintuplet state become degenerate. For all fields above H_c' the $S^z = 2$ quintuplet state is the groundstate, with gaps to all other states that grow as field is increased.

Several basic thermodynamic properties can be immediately determined from the isolated dimer energy spectrum through basic statistical mechanics and the canonical partition function. The functional form of the magnetization as a function of field is:

$$\begin{aligned} M &= \frac{\sum_{j,m_j} (Ng\mu_B m_j)\, e^{-(E_j + g\mu_B m_j \mu_0 H)\beta}}{Z} = \frac{Ng\mu_B}{Z} \sum_j e^{-E_j\beta} \sum_{m_j} m_j e^{-g\mu_B m_j \mu_0 H \beta} \\ &= \frac{4Ng\mu_B}{Z} \{\cosh(J\beta) \sinh(g\mu_B\mu_0 H\beta) + e^{-J\beta} \sinh(2g\mu_B\mu_0 H\beta)\} \end{aligned} \tag{2.1}$$

Where Z is the canonical partition function

$$\begin{aligned} Z &= \sum_{j,m_j} e^{-(E_j + m_j g\mu_B\mu_0 H)\beta} \\ &= e^{2J\beta} + 2\cosh(J\beta)\,[1 + 2\cosh(g\mu_B\mu_0 H)] + 2e^{-J\beta}\cosh(2g\mu_B\mu_0 H) \end{aligned} \tag{2.2}$$

, $\beta = 1/k_B T$ and N is Avogadro's number.

The magnetization is plotted for several temperatures in Fig. 2.1. The zero temperature magnetization, shown in black, reveals zero magnetization at low fields as the system is a product of singlets, a step to a plateau of half the full magnetization of 1 μ_B above H_c as the system has an $S^z = 1$ triplet on each site, followed by a second step at H_c', above which the system is fully polarized with $S^z = 2$ quintuplet states at 2 μ_B. At higher temperatures these transitions smear out, starting at zero magnetization at zero field, before eventually asymptotically approaching the saturation magnetization at fields above H_c', and having the maximal change in magnetization at the critical fields.

The susceptibility is also easily calculated provided the applied magnetic field is sufficiently small, $H \ll H_c = J/g\mu_0\mu_B$, and the magnetization is directly proportional

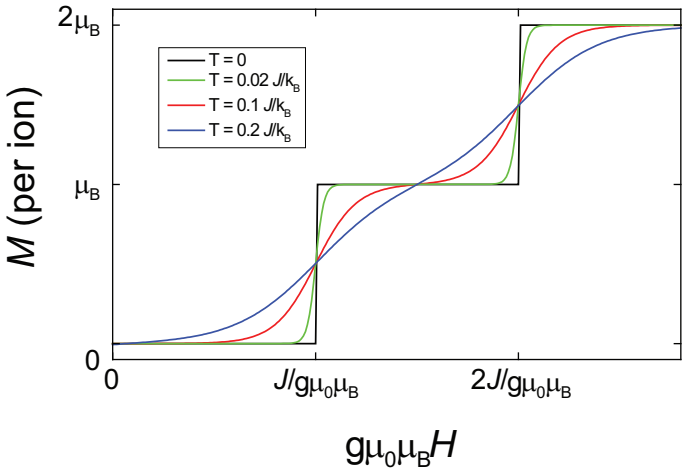

Figure 2.1: Magnetization of isolated dimer composed of $S = 1$ spins at several different temperatures.

to the applied field. The temperature dependence of the low field susceptibility is

$$\chi_d = \frac{dM}{dH} \cong \frac{M}{H} = 2Ng^2\mu_B^2\beta\frac{1+5e^{-2J\beta}}{e^{J\beta}+3+5e^{-2J\beta}} \tag{2.3}$$

and is plotted in Fig. 2.2. The susceptibility has an exponential rise at low temperatures, $T < J/k_B$, as the spin gaps between the singlet state and the excited triplet and quintuplet states are populated. At higher temperatures, $T > 3J/k_B$, the susceptibility shows more Curie-like $1/T$ behavior as all the states are relatively evenly populated and paramagnetic behavior is approximated.

2.2 Spin Hamiltonian

Determining all the terms present in the spin Hamiltonian is crucial for theoretical determination of the ordered ground states. The primary microscopic measurements used to determine the available terms were inelastic neutron scattering and electron paramagnetic resonance.

Inelastic neutron scattering (INS) experiments are a very powerful technique for

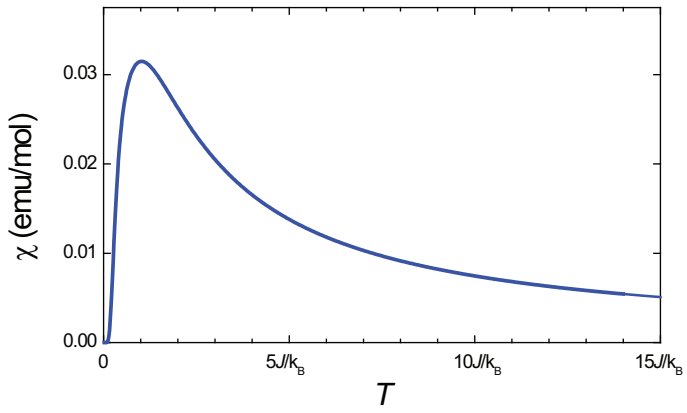

Figure 2.2: Susceptibility of an isolated dimer composed of $S = 1$ spins.

determining the energy spectrum of a system. Both powder and single crystal diffraction studies were undertaken on this system by collaborators using samples prepared as part of this thesis work [26, 27, 28]. In these measurements the magnetic energy dispersion is collected, allowing determination of the relevant exchanges by fitting to the dispersion (see Appendix A). Further study of the experimental dispersion and the theoretical fit to that dispersion is in Appendix A. The single crystal studies yielded a value for the exchange within a dimer, $J_0 = 1.642$ meV, where the nomenclature for the exchanges taken from previous polycrystalline work [24] (see Fig. 2.3). Several higher order exchanges were also determined from the fit: the in-plane exchange between next nearest Mn ions and also between next next nearest Mn ions, $J_2 - J_3 = 0.1136$ meV; the out-of-plane exchange between nearest Mn ions, $J_1 = 0.118$ meV; and the out-of-plane exchange between next nearest Mn ions, $J_4 = 0.037$ meV. While the individual values of J_2 and J_3 could not be fit due to the equivalent functional dependence of those two exchanges in the magnetic dispersion, however, measurements of the critical fields yielded estimates for J_2 and J_3 of 0.256 meV and 0.142 meV, respectively [27, 28]

Electron paramagnetic resonance (EPR) studies measures transitions between different states, from which additional terms in the effective Hamiltonian, such as Dzaloshinskii-Moriya and dipole-dipole interactions, can be revealed. Early EPR

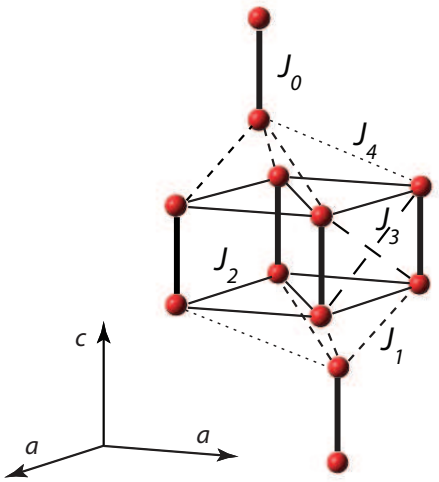

Figure 2.3: Magnetic lattice of $Ba_3Mn_2O_8$ showing various exchanges. Red spheres are magnetic Mn ions. Exchange within a dimer (J_0) shown as thick line. Exchange between dimers within a plane directly between tetrahedra (J_2) and diagonally across neighboring dimers (J_3) shown as thin black line and long dashed lines. Interdimer exchange between planes between nearest neighboring spins (J_1) and next nearest spins (J_4) shown as short dashed lines and dotted lines.

studies were undertaken on lightly doped $Ba_3(Mn_xV_{1-x})_2O_8$ system [35]. These studies showed the presence of both Mn^{5+} and Mn^{4+} with spins of $S = 1$ and $S = \frac{3}{2}$, respectively, where the Mn^{5+} valence is five times more prevalent than the Mn^{4+} valence (the samples used in this thesis were not found to have significant concentrations of Mn^{4+} ions, although a small concentration of such ions cannot be ruled out.) The Mn^{5+} ions were found to have a nearly isotropic g factor, with g_{aa}=1.9608 and g_{cc}=1.9722, and an easy axis single ion anisotropy of D=-5.81 GHz, corresponding to 0.024 meV. More recent EPR studies performed by collaborators on single crystals of $Ba_3Mn_2O_8$ that I grew confirmed the nearly isotropic nature of the g factor [36]. Those measurements also found a zero field splitting of $\|D\|$=0.032 meV; the difference cannot be accounted for by just the intradimer dipolar interaction, implying the presence of additional weak interactions that affect the zero field splitting in the concentrated lattice.

The minimal spin Hamiltonian for this system incorporating all these terms is:

$$\begin{aligned}\mathcal{H} &= \sum_{i,j,\mu,\nu} \frac{J_{i\mu j\nu}}{2} \mathbf{S}_{i\mu} \cdot \mathbf{S}_{j\nu} + D \sum_{i,\mu} \left(S^z_{i\mu} \cos\theta - S^x_{i\mu} \sin\theta \right)^2 \\ &\quad -\mu_B H \sum_{i\mu\alpha\beta} \left(\tilde{g}_{zz} S^z_{i\mu} + \tilde{g}_{xz} S^x_{i\mu} \right). \end{aligned} \tag{2.4}$$

The quantization z axis is set by the field direction while θ is the angle between the field direction and the crystalline c axis. Here $\tilde{g}_{zz} = g_{aa} \sin^2\theta + g_{cc} \cos^2\theta$ and $\tilde{g}_{xz} = (g_{cc} - g_{aa}) \sin\theta \cos\theta$. i, j designate the dimer coordinates, $\alpha, \beta = \{x, y, z\}$ and $\mu, \nu = \{1, 2\}$ denote each of the two $S = 1$ spins in each dimer. The various exchange constants shown in Fig. 2.3(a) are defined as follows: $J_0 = J_{i,1,i,2}$; $J_1 = J_{i,2,j,1}$ for i, j nearest neighbor dimers between planes; $J_2 = J_{i,\mu,j,\mu}$ and $J_3 = J_{i,\mu,j,\nu}$ for i, j in plane nearest neighbor dimers and $\mu \neq \nu$; and finally $J_4 = J_{i,2,j,1}$ for i, j next nearest neighbor dimers between planes. Using this Hamiltonian most of the important features of the phase diagram can be understood.

2.3 Effective Pseudospin Transformation

Mapping spin dimer systems onto a pseudospin $\frac{1}{2}$ model is a convenient method for qualitatively and quantitatively understanding these systems. This transformation can be performed in the singlet/$S^z = 1$ triplet regime for magnetic fields close to H_{c1} and sufficiently low temperatures where the higher energy $S^z = -1$ and $S^z = 0$ triplet and quintuplet states can be neglected to a reasonable level of approximation. In such a case the Hilbert space is spanned by the singlet and $S^z = 1$ triplet states, and the pseudospin $\tilde{s} = \frac{1}{2}$ represents the system such that the singlet state is the $\tilde{s}^z = \frac{-1}{2}$ state, and the $S^z = 1$ triplet state is the $\tilde{s}^z = \frac{1}{2}$ state (real spins are represented by capital letters and pseudospin operators by lowercase letters with tildes) [37]. A similar mapping is possible for the $S^z = 1$ triplet and the $S^z = 2$ quintuplet states in the regime for which these two states are degenerate (neglecting the four other quintuplet, two other triplet and singlet states), in which the $S^z = 1$ triplet state is the $\tilde{s}^z = \frac{-1}{2}$ state and the $S^z = 2$ quintuplet is the $\tilde{s}^z = \frac{1}{2}$ state. This transformation has been extensively studied for the two-leg ladder systems with $S = \frac{1}{2}$ spins under application of a magnetic field [38, 39]. In this section I will show a detailed demonstration of the transformation in $Ba_3Mn_2O_8$ for both the singlet/$S^z = 1$ triplet regime and the $S^z = 1$ triplet/$S^z = 2$ quintuplet regime by determining the form of the various terms present before finally presenting the final form of the effective Hamiltonians.

2.3.1 Relationship Between Real Spin and Pseudospin Operators

Before describing in detail the relationship between the real spin and pseudospin operators it is instructive to describe how the basic pseudospin operators act:

$$\begin{aligned} \tilde{s}^+|\uparrow\rangle &= 0 & \tilde{s}^+|\downarrow\rangle &= \tfrac{1}{\sqrt{2}}|\uparrow\rangle \\ \tilde{s}^-|\uparrow\rangle &= \tfrac{1}{\sqrt{2}}|\downarrow\rangle & \tilde{s}^-|\downarrow\rangle &= 0 \\ \tilde{s}^z|\uparrow\rangle &= \tfrac{1}{2}|\uparrow\rangle & \tilde{s}^z|\downarrow\rangle &= \tfrac{-1}{2}|\downarrow\rangle \end{aligned}$$

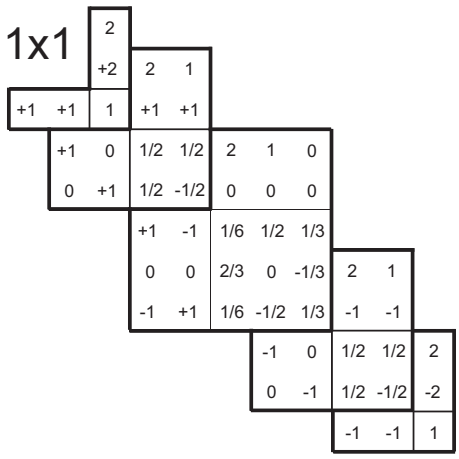

Figure 2.4: Clebsch-Gordan table for two $S = 1$ spins.

Here, $\tilde{s}^{\alpha}$'s are the pseudospin operators while $|\uparrow\rangle$ and $|\downarrow\rangle$ are pseudospin up and pseudospin down, respectively. Spin up and spin down correspond to different dimer states in the two different regimes: in the singlet/$S^z = 1$ triplet regime, spin up (spin down) corresponds to the $S^z = 1$ triplet (singlet); in the $S^z = 1$ triplet / $S^z = 2$ quintuplet regime, spin up (spin down) corresponds to the $S^z = 2$ quintuplet ($S^z = 1$ triplet). The transformations for these two regimes are nearly identical, with only a few changes in the prefactors of the terms in the effective Hamiltonians, which vary because the dimer states are composed of different individual ion states with varying Clebsch-Gordan coefficients (Fig. 2.4). The relationship between the pseudospin and real spin operators is determined by comparing how the different operators act on each of the dimer states. The equivalences between the two different representations are:

$\|00\rangle/\|11\rangle$ Regime	$\|11\rangle/\|22\rangle$ Regime
$S_1^+ = \frac{-2}{\sqrt{3}}\tilde{s}^+$	$S_1^+ = -\tilde{s}^+$
$S_2^+ = \frac{2}{\sqrt{3}}\tilde{s}^+$	$S_2^+ = \tilde{s}^+$
$S_1^- = \frac{-2}{\sqrt{3}}\tilde{s}^-$	$S_1^- = -\tilde{s}^-$
$S_2^- = \frac{2}{\sqrt{3}}\tilde{s}^-$	$S_2^- = \tilde{s}^-$
$S_1^z = \frac{1}{2}\left(\tilde{s}^z + \frac{1}{2}\right)$	$S_1^z = \frac{1}{2}\left(\tilde{s}^z + \frac{3}{2}\right)$
$S_2^z = \frac{1}{2}\left(\tilde{s}^z + \frac{1}{2}\right)$	$S_2^z = \frac{1}{2}\left(\tilde{s}^z + \frac{3}{2}\right)$

The pseudospin operators clearly are not uniquely defined in each regime because each dimer comprises two different spins. Most of the terms of the real spin Hamiltonian (Eq. 2.4) are easily converted into the pseudospin language using these relations. However, the zero field splitting term is not trivially expressed in the pseudospin language due to its angular variation. The real spin language expression of the zero field splitting is:

$$\begin{aligned} H_{SI} &= D\sum_{i,\mu}\left(S^z_{i\mu}\cos\theta - S^x_{i\mu}\sin\theta\right)^2 \\ &= D\sum_{i\mu}\left[\left(S^z_{i\mu}\cos\theta\right)^2 + \left(S^x_{i\mu}\sin\theta\right)^2 - \left(S^z_{i\mu}S^x_{i\mu} + S^x_{i\mu}S^z_{i\mu}\right)\sin\theta\cos\theta\right] \quad (2.5) \end{aligned}$$

The first of these three terms, $D\left(S^z_{i\mu}\cos\theta\right)^2$, is easily expressed in pseudospin language. However, the second and third terms are not so easily transformed and will ultimately enter the Hamiltonian as a result of second order processes. Over the next two subsections I will first analyze the second term, $H_{SI2} = D\left(S^x_{i\mu}\sin\theta\right)^2$ and then third term, $H_{SI3} = \left(S^z_{i\mu}S^x_{i\mu} + S^x_{i\mu}S^z_{i\mu}\right)\sin\theta\cos\theta$ of the zero field splitting.

2.3.2 Effective Zero Field Splitting for Fields Perpendicular to the c Axis

For fields perpendicular to the c axis ($\theta = \pi/2$) the ordered moments of the canted antiferromagnetic states lie in the plane perpendicular to the field direction. The easy axis anisotropy in the ordering plane favors spins along the c axis and disfavors spins perpendicular to both the c axis and field direction. However, $H_{SI3} = 0$ for $\theta = \pi/2$ while $H_{SI2} = D\left(S^x_{i\mu}\right)^2$ cannot directly connect singlets and triplets (or triplets and quintuplets) because H_{SI2} is a symmetric operator and those states have different symmetry, so a second order process is required to mix these various states.

The second order processes connecting the symmetric and antisymmetric states involves both the application of H_{SI2} and an exchange term (any of the exchanges will work). There are two processes in each of the different regimes, depending on

the order of application of the two interactions.

$|00\rangle/|11\rangle$ Regime

The second order process in which H_{SI2} is first applied yields the excited intermediate $|22\rangle_i$ state:

$$\langle 22|_i D\left[(S_1^x)^2+(S_2^x)^2\right]|00\rangle_i = \frac{D}{\sqrt{3}} \tag{2.6}$$

The second half of this second order process is application of a Heisenberg exchange between neighboring dimer sites i and j. Such an exchange induces a transition from the virtual state $|22\rangle_i|00\rangle_j$ to the final state $|11\rangle_i|11\rangle_j$ (this subsection will use solely the J_2 interdimer exchange, but the equivalent interaction exists for each of the interdimer exchange terms):

$$\langle 11|_j\langle 11|_i \frac{J_2}{2}\left(\mathbf{S}_{i,1}\cdot\mathbf{S}_{j,1}+\mathbf{S}_{i,2}\cdot\mathbf{S}_{j,2}\right)|22\rangle_i|00\rangle_j = \frac{2J_2}{\sqrt{3}} \tag{2.7}$$

The total energy shift of this second order process is calculated by using the value for the gap between the groundstates and the excited $|22\rangle_i$ quintuplet state in this regime of J_0:

$$\Delta E^{(2)} = \frac{M_1 M_2}{E_{GS}-E_{excited}} = \frac{D}{\sqrt{3}}\times\frac{2J_2}{\sqrt{3}}\div -J_0 = \frac{-2DJ_2}{3J_0} \tag{2.8}$$

The other second order process in $|00\rangle/|11\rangle$ regime has the Heisenberg exchange applied first, yielding an intermediate state of $|1\bar{1}\rangle_i$:

$$\langle 11|_j\langle 1\bar{1}|_i \frac{J_2}{2}\left(\mathbf{S}_{i,1}\cdot\mathbf{S}_{j,1}+\mathbf{S}_{i,2}\cdot\mathbf{S}_{j,2}\right)|00\rangle_i|00\rangle_j = \frac{-4J_2}{3} \tag{2.9}$$

The second half of this second order process is application of the H_{SI2} term which induces a transition between the $|1\bar{1}\rangle_i$ and $|11\rangle_i$ states:

$$\langle 11|_i D\left[(S_1^x)^2+(S_2^x)^2\right]|1\bar{1}\rangle_i = \frac{-D}{2} \tag{2.10}$$

The total energy shift of this second order process is calculated by using a value

for the gap between the groundstates and the excited $|1\bar{1}\rangle_i$ triplet state in this regime of $2J_0$:

$$\Delta E^{(2)} = \frac{M_1 M_2}{E_{GS} - E_{excited}} = \frac{-4J_2}{3} \times \frac{-D}{2} \div -2J_0 = \frac{-DJ_2}{3J_0} \tag{2.11}$$

The energy shifts of each of these processes are doubled because the excited state can be created on either the i or the j site. For the J_2 and J_3 exchanges these processes are doubled again because these are two of these interactions between each pair of dimers connected by these exchanges. Combining these two processes together, the effective interaction induced by H_{SI2} in the $|00\rangle|11\rangle$ regime between the i and j sites connected by J_2 is:

$$2J_2 a(\theta) \left(\tilde{s}_i^x \tilde{s}_j^x - \tilde{s}_i^y \tilde{s}_j^y\right) \tag{2.12}$$

where $a(\theta) = -2D\sin^2(\theta)/J_0$. The $\tilde{s}_i^x \tilde{s}_j^x - \tilde{s}_i^y \tilde{s}_j^y = \tilde{s}_i^+ \tilde{s}_j^+ - \tilde{s}_i^- \tilde{s}_j^-$ factor turns neighboring singlets into $S^z = 1$ triplets and vice versa.

$|11\rangle/|22\rangle$ Regime

The two processes of this regime have a similar form to the processes of the singlet-$S^z = 1$ triplet regime but have different intermediate virtual states. The second order process in which H_{SI2} is first applied yields the excited intermediate $|00\rangle_i$ state:

$$\langle 00|_i D\left[(S_1^x)^2 + (S_2^x)^2\right]|22\rangle_i = \frac{D}{\sqrt{3}} \tag{2.13}$$

The second half of this second order process is application of a Heisenberg exchange between neighboring sites i and j. Such an exchange induces a transition from the virtual state $|00\rangle_i|22\rangle_j$ to the final state $|11\rangle_i|11\rangle_j$:

$$\langle 11|_j\langle 11|_i \frac{J_2}{2}\left(\mathbf{S}_{i,1}\cdot\mathbf{S}_{j,1} + \mathbf{S}_{i,2}\cdot\mathbf{S}_{j,2}\right)|00\rangle_i|22\rangle_j = \frac{2J_2}{\sqrt{3}} \tag{2.14}$$

The total energy shift of this second order process is calculated by using a value for the gap between the groundstates and the excited singlet state in this regime of J_0:

$$\Delta E^{(2)} = \frac{M_1 M_2}{E_{GS} - E_{excited}} = \frac{D}{\sqrt{3}} \times \frac{2J_2}{\sqrt{3}} \div -J_0 = \frac{-2DJ_2}{3J_0} \tag{2.15}$$

The other second order process in $|11\rangle/|22\rangle$ regime has the Heisenberg exchange applied first, yielding an intermediate state of $|20\rangle_i$:

$$\langle 22|_j \langle 20|_i \frac{J_2}{2} \left(\mathbf{S}_{i,1} \cdot \mathbf{S}_{j,1} + \mathbf{S}_{i,2} \cdot \mathbf{S}_{j,2}\right) |11\rangle_i |11\rangle_j = \frac{-J_2}{\sqrt{6}} \tag{2.16}$$

The second half of this second order process is application of the H_{SI2} term which induces a transition between the $|20\rangle_i$ and $|22\rangle_i$ states:

$$\langle 22|_i D \left[\left(S_1^x\right)^2 + \left(S_2^x\right)^2\right] |20\rangle_i = \frac{D}{\sqrt{6}} \tag{2.17}$$

The total energy shift of this second order process is calculated by using a value for the gap between the degenerate groundstates and the excited $|20\rangle_i$ quintuplet state in this regime of $4J_0$:

$$\Delta E^{(2)} = \frac{M_1 M_2}{E_{excited} - E_{GS}} = \frac{-J_2}{\sqrt{6}} \times \frac{D}{\sqrt{6}} \div -4J_0 = \frac{DJ_2}{24J_0} \tag{2.18}$$

The energy shifts of each of these processes are doubled because the excited state can be created on either the i or j site. For the J_2 and J_3 exchanges these processes are doubled again because these are two of these interactions between each pair of dimers connected by these exchanges. Combining these two processes together, the effective interaction induced by H_{SI2} in the $|11\rangle|22\rangle$ regime between the i and j sites connected by J_2 is:

$$2J_2 b(\theta) \left(\tilde{s}_i^x \tilde{s}_j^x - \tilde{s}_i^y \tilde{s}_j^y\right) \tag{2.19}$$

where $b(\theta) = -5D \sin^2(\theta)/4J_0$. The $\tilde{s}_i^x \tilde{s}_j^x - \tilde{s}_i^y \tilde{s}_j^y = \tilde{s}_i^+ \tilde{s}_j^+ - \tilde{s}_i^- \tilde{s}_j^-$ factor turns neighboring $S^z = 1$ triplets into $S^z = 2$ quintuplets or vice versa.

2.3.3 Effective Zero Field Splitting at Intermediate Angles

At intermediate angles the H_{SI3} is no longer nonzero (in contrast to its value for fields along or perpendicular to the c axis, $\theta = 0, \pi/2$ respectively). The real spin form of this term is:

$$H_{SI3} = -D \sum_{i\mu} \left(S^z_{i\mu} S^x_{i\mu} + S^x_{i\mu} S^z_{i\mu} \right) \sin\theta \cos\theta \tag{2.20}$$

There is a single second order process in each regime connecting the symmetric and antisymmetric states through application of this term and a interdimer exchange term. In contrast to the second order processes associated with the other term from the zero field splitting, there is only one pathway in each regime and only one order of application of these terms yields a nonzero value for this term.

$|00\rangle/|11\rangle$ Regime

In the $|00\rangle/|11\rangle$ regime the only second order process that connects the two degenerate ground states has first application of the interdimer exchange before application of H_{SI3}.

The intermediate state which can be connected to the final state by this term of the zero field splitting is $|21\rangle_i$. However, the interdimer exchanges within a plane (J_2 or J_3 exchange) cannot induce a transition between the $|11\rangle_i$ and $|21\rangle_i$ states because the exchange between spins on the top half of neighboring dimers exactly counteracts the exchange between spins on the bottom half of the neighboring dimers:

$$\begin{aligned} \langle 11|_j \langle 21|_i \frac{J_2}{2} \mathbf{S}_{i,1} \cdot \mathbf{S}_{j,1} |11\rangle_i |11\rangle_j &= \frac{J_2}{8} \\ \langle 11|_j \langle 21|_i \frac{J_2}{2} \mathbf{S}_{i,2} \cdot \mathbf{S}_{j,2} |11\rangle_i |11\rangle_j &= \frac{-J_2}{8} \end{aligned} \tag{2.21}$$

This cancelation of the exchanges acting on the top and bottom spins of a dimer contrasts the earlier second order processes, where the interdimer exchange on both halves of the exchange yielded the same result, doubling the total value. The same

cancelation does not occur for interdimer exchange between planes because those terms only connect only the top of one dimer to the bottom of another dimer (this subsection will use solely the J_1 exchange, but the equivalent interaction exists also for the J_4 exchange):

$$\langle 11|_j\langle 21|_i \frac{J_1}{2}\mathbf{S}_{i,1}\cdot\mathbf{S}_{j,2}|11\rangle_i|11\rangle_j = \frac{J_1}{8} \tag{2.22}$$

Here the i dimer is in the layer below the j dimer. However, if the intermediate $|21\rangle$ state is put in the j dimer instead of the i dimer, the result changes sign:

$$\langle 21|_j\langle 11|_i \frac{J_1}{2}\mathbf{S}_{i,1}\cdot\mathbf{S}_{j,2}|11\rangle_i|11\rangle_j = \frac{-J_1}{8} \tag{2.23}$$

Thus this term will be positive for the dimer on the i site but negative for the dimer on the j site. H_{SI3} transforms the intermediate $|21\rangle$ state into the $|00\rangle$ state:

$$\langle 00|_i D\left[(S_1^z S_1^x + S_1^x S_1^z) + (S_2^z S_2^x + S_2^x S_2^z)\right]\cos\theta\sin\theta|21\rangle_i = \frac{-2D}{\sqrt{3}}\cos\theta\sin\theta \tag{2.24}$$

The total energy shift of this second order process is calculated by using a value for the gap between the degenerate groundstates and the excited $|21\rangle_i$ quintuplet state in this regime of $2J_0$:

$$\Delta E^{(2)} = \frac{M_1 M_2}{E_{GS} - E_{excited}} = \frac{J_1}{8}\times\frac{-2D\cos\theta\sin\theta}{\sqrt{3}}\div -2J_0 = \frac{DJ_1\cos\theta\sin\theta}{8\sqrt{3}J_0} \tag{2.25}$$

Expressing this process in pseudospin language, the final term is:

$$\frac{DJ_1}{4\sqrt{3}J_0}\cos\theta\sin\theta\left(\tilde{s}_i^z\tilde{s}_j^x - \tilde{s}_i^x\tilde{s}_j^z\right) = J_1\tilde{\mathbf{D}}(\theta)\cdot\tilde{\mathbf{s}}_i\times\tilde{\mathbf{s}}_j \tag{2.26}$$

where $\tilde{\mathbf{D}}(\theta) = \sin(\theta)\cos(\theta)\frac{D}{4\sqrt{3}J_0}\hat{\mathbf{y}}$. The $\tilde{s}_i^z\tilde{s}_j^x - \tilde{s}_i^x\tilde{s}_j^z = \hat{\mathbf{y}}\cdot\tilde{\mathbf{s}}_i\times\tilde{\mathbf{s}}_j$ factor acts differently depending on which initial state it is acting. If the initial state is neighboring singlets on sites i and j then the term induces a transformation to a superposition of two states with half the total amplitude: 1) a $S^z = 1$ triplet on site i and a singlet on

site j with positive amplitude and 2) a singlet site i and a $S^z = 1$ triplet on site j with negative amplitude. If the initial state is neighboring $S^z = 1$ triplets on sites i and j then the term induces a transformation to a superposition of two states with half the total amplitude: 1) a $S^z = 1$ triplet on site i and a singlet on site j with negative amplitude and 2) a singlet site i and a $S^z = 1$ triplet on site j with positive amplitude.

$|11\rangle/|22\rangle$ Regime

This second order process for this regime is qualitatively the same as the process in the $|00\rangle/|11\rangle$ regime: there is only one virtual process connecting these states using H_{SI3}, only the J_1 and J_4 exchanges yield nonzero values, the intermediate state is the $|21\rangle$ state, and this term changes sign depending on which side of the dimer it is acting. Applying first the interdimer exchange to the $|22\rangle$ state:

$$\begin{aligned} \langle 11|_j\langle 21|_i \frac{J_1}{2}\mathbf{S}_{i,1}\cdot\mathbf{S}_{j,2}|11\rangle_i|11\rangle_j &= \frac{J_1}{8} \\ \langle 21|_j\langle 11|_i \frac{J_1}{2}\mathbf{S}_{i,1}\cdot\mathbf{S}_{j,2}|11\rangle_i|11\rangle_j &= \frac{-J_1}{8} \end{aligned} \tag{2.27}$$

H_{SI3} transforms the intermediate $|21\rangle$ state into the $|22\rangle$ state:

$$\langle 22|_i D\left[(S_1^z S_1^x + S_1^x S_1^z) + (S_2^z S_2^x + S_2^x S_2^z)\right]\cos\theta\sin\theta|21\rangle_i = D\cos\theta\sin\theta \tag{2.28}$$

The total energy shift of this second order process is calculated by using a value for the gap between the degenerate groundstates and the excited $|21\rangle_i$ quintuplet state in this regime of $2J_0$:

$$\Delta E^{(2)} = \frac{M_1 M_2}{E_{GS} - E_{excited}} = \frac{J_1}{8}\times D\cos\theta\sin\theta \div -2J_0 = \frac{-DJ_1\cos\theta\sin\theta}{16J_0} \tag{2.29}$$

Expressing this process in pseudospin language, the final term is:

$$\frac{-DJ_1}{8J_0}\cos\theta\sin\theta\left(\tilde{s}_i^z\tilde{s}_j^x-\tilde{s}_i^x\tilde{s}_j^z\right)=J_1\tilde{\mathbf{D}}'(\theta)\cdot\tilde{\mathbf{s}}_i\times\tilde{\mathbf{s}}_j \tag{2.30}$$

where $\tilde{\mathbf{D}}'(\theta)=-\sin(\theta)\cos(\theta)\frac{D}{8J_0}\hat{\mathbf{y}}$. The $\tilde{s}_i^z\tilde{s}_j^x-\tilde{s}_i^x\tilde{s}_j^z=\hat{\mathbf{y}}\cdot\tilde{\mathbf{s}}_i\times\tilde{\mathbf{s}}_j$ factor acts in two ways depending on which initial state it is acting. If the initial state is neighboring $S^z=1$ triplets on sites i and j then the term induces a transformation to a superposition of two states with half the total amplitude: 1) a $S^z=2$ quintuplet on site i and a $S^z=1$ triplet on site j with positive amplitude and 2) a $S^z=1$ triplet on site i and a $S^z=2$ quintuplet on site j with negative amplitude. If the initial state is neighboring $S^z=2$ quintuplets on sites i and j then the term induces a transformation to a superposition of two states with half the total amplitude: 1) a $S^z=2$ quintuplet on site i and a $S^z=1$ triplet on site j with negative amplitude and 2) a $S^z=1$ triplet site i and a $S^z=2$ quintuplet on site j with positive amplitude.

2.3.4 Effective Hamiltonian

The complete form of the effective Hamiltonian in pseudospin language in the $|00\rangle/|11\rangle$ regime is:

$$
\begin{aligned}
\tilde{\mathcal{H}}_{st} &= J_1 \sum_{l\langle\langle i,j\rangle\rangle} \left[\frac{1}{4}\tilde{s}^z_{il}\tilde{s}^z_{jl+1} + \frac{4}{3}\left(\tilde{s}^x_{il}\tilde{s}^x_{jl} + \tilde{s}^y_{il}\tilde{s}^y_{jl}\right)\right] \\
&+ J_4 \sum_{l\langle\langle i,j\rangle\rangle'} \left[\frac{1}{4}\tilde{s}^z_{il}\tilde{s}^z_{jl+1} + \frac{4}{3}\left(\tilde{s}^x_{il}\tilde{s}^x_{jl} + \tilde{s}^y_{il}\tilde{s}^y_{jl}\right)\right] \\
&+ \sum_{l\langle i,j\rangle} \left[\frac{(J_2+J_3)}{2}\tilde{s}^z_{il}\tilde{s}^z_{jl} + \frac{8\,(J_2-J_3)}{3}\left(\tilde{s}^x_{il}\tilde{s}^x_{jl} + \tilde{s}^y_{il}\tilde{s}^y_{jl}\right)\right] \\
&- J_1 a(\theta) \sum_{l\langle\langle i,j\rangle\rangle} \left(\tilde{s}^x_{il}\tilde{s}^x_{jl+1} - \tilde{s}^y_{il}\tilde{s}^y_{jl+1}\right) - J_4 a(\theta) \sum_{l\langle\langle i,j\rangle\rangle'} \left(\tilde{s}^x_{il}\tilde{s}^x_{jl+1} - \tilde{s}^y_{il}\tilde{s}^y_{jl+1}\right) \\
&+ 2\,(J_2 - J_3)\, a(\theta) \sum_{l\langle i,j\rangle} \left(\tilde{s}^x_{il}\tilde{s}^x_{jl} - \tilde{s}^y_{il}\tilde{s}^y_{jl}\right) \\
&+ J_1 \sum_{l\langle\langle i\to j\rangle\rangle} \tilde{\mathbf{D}}(\theta)\cdot\tilde{\mathbf{s}}_i \times \tilde{\mathbf{s}}_j + J_4 \sum_{l\langle\langle i\to j\rangle\rangle'} \tilde{\mathbf{D}}(\theta)\cdot\tilde{\mathbf{s}}_i \times \tilde{\mathbf{s}}_j \\
&- B_{st}\,(\theta) \sum_{l,i} \tilde{s}^z_{il}. \qquad (2.31)
\end{aligned}
$$

Here, $\langle i,j\rangle$, $\langle\langle i,j\rangle\rangle$ and $\langle\langle i,j\rangle\rangle'$ denote i and j as nearest neighboring dimers in plane, nearest neighboring dimers out of plane, and next nearest neighboring dimers out of plane, respectively. The definition of the effective zero field splitting coefficients are: $a(\theta) = -\frac{2\sin^2(\theta)D}{J_0}$ and $\tilde{\mathbf{D}}(\theta) = \sin(\theta)\cos(\theta)\frac{D}{4\sqrt{3}J_0}\hat{\mathbf{y}}$. $\langle\langle i\to j\rangle\rangle$ and $\langle\langle i\to j\rangle\rangle'$ imply that the i dimer is always on the lower level relative to the j dimer. The effective field is $B_{st} = \tilde{g}_{zz}\mu_B H - J_0 - 3(J_2+J_3)/2 - 3(J_1+J_4)/4 + D\cos^2(\theta)/3$.

The effective Hamiltonian in the $|11\rangle/|22\rangle$ regime is:

$$
\begin{aligned}
\tilde{\mathcal{H}}_{tq} &= J_1 \sum_{l\langle\langle i,j\rangle\rangle} \left[\frac{1}{4}\tilde{s}^z_{il}\tilde{s}^z_{jl+1} + \left(\tilde{s}^x_{il}\tilde{s}^x_{jl} + \tilde{s}^y_{il}\tilde{s}^y_{jl}\right)\right] \\
&+ J_4 \sum_{l\langle\langle i,j\rangle\rangle'} \left[\frac{1}{4}\tilde{s}^z_{il}\tilde{s}^z_{jl+1} + \left(\tilde{s}^x_{il}\tilde{s}^x_{jl} + \tilde{s}^y_{il}\tilde{s}^y_{jl}\right)\right] \\
&+ \sum_{l\langle i,j\rangle} \left[\frac{(J_2+J_3)}{2}\tilde{s}^z_{il}\tilde{s}^z_{jl} + 2\left(J_2 - J_3\right)\left(\tilde{s}^x_{il}\tilde{s}^x_{jl} + \tilde{s}^y_{il}\tilde{s}^y_{jl}\right)\right] \\
&- J_1 b(\theta) \sum_{l\langle\langle i,j\rangle\rangle} \left(\tilde{s}^x_{il}\tilde{s}^x_{jl+1} - \tilde{s}^y_{il}\tilde{s}^y_{jl+1}\right) - J_4 b(\theta) \sum_{l\langle\langle i,j\rangle\rangle'} \left(\tilde{s}^x_{il}\tilde{s}^x_{jl+1} - \tilde{s}^y_{il}\tilde{s}^y_{jl+1}\right) \\
&+ 2\left(J_2 - J_3\right) b(\theta) \sum_{l\langle i,j\rangle} \left(\tilde{s}^x_{il}\tilde{s}^x_{jl} - \tilde{s}^y_{il}\tilde{s}^y_{jl}\right) \\
&+ J_1 \sum_{l\langle\langle i\to j\rangle\rangle} \tilde{\mathbf{D}}'(\theta)\cdot\tilde{\mathbf{s}}_i \times \tilde{\mathbf{s}}_j + J_4 \sum_{l\langle\langle i\to j\rangle\rangle'} \tilde{\mathbf{D}}'(\theta)\cdot\tilde{\mathbf{s}}_i \times \tilde{\mathbf{s}}_j \\
&- B_{tq}(\theta) \sum_{l,i} \tilde{s}^z_{il}. \qquad (2.32)
\end{aligned}
$$

The effective zero field couplings are slightly modified in this regime: $b(\theta) = -\frac{5\sin^2(\theta)D}{4J_0}$ and $\tilde{\mathbf{D}}'(\theta) = -\sin(\theta)\cos(\theta)\frac{D}{8J_0}\hat{\mathbf{y}}$. The effective field is $B_{tq} = \tilde{g}_{zz}\mu_B H - 2J_0 - 9(J_2+J_3)/2 - 9(J_1+J_4)/4 + D\cos^2(\theta)/3$.

These Hamiltonians have proven very powerful in describing much of the behavior of the ordered states of this system [29, 30, 33, 31].

Chapter 3

Crystal Growth and Characterization

Single crystals are critical for performing many different high precision measurements, including measurements of the crystal lattice anisotropy. In this section I will describe the crystal growth process and the characterization measurements performed on the resulting single crystals.

3.1 Single Crystal Growth

Single crystals of $Ba_3Mn_2O_8$, $Ba_3V_2O_8$ and substitutional alloy $Ba_3(Mn_{1-x}V_x)_2O_8$ were grown via a two step process. First, polycrystal precursor was synthesized through a solid state process. Second, the polycrystalline precursor was mixed with a flux to grow single crystals.

3.1.1 Ternary Phase Diagram

Compounds in the Ba-Mn-O system are represented in a ternary diagram, shown in Fig. 3.1. The Ba ions have a +2 oxidation state. In transition metal oxides Mn is often found with a formal valence of +3 or +4 . However, Mn can take a range of valences, including +2 (Ba_2MnO_3), +3 (Mn_2O_3), +4 ($BaMnO_3$) and +7 ($BaMn_2O_8$).

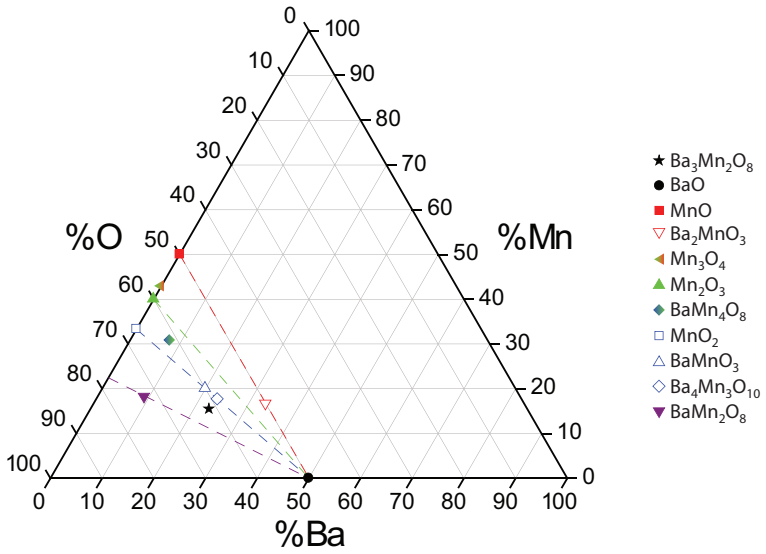

Figure 3.1: Ba-Mn-O ternary diagram showing $Ba_3Mn_2O_8$ (black star) and other phases. Compounds with the Mn valence of +2 (red), +3 (green), +4 (blue) and +7 (purple) are grouped by color and connected by dashed lines, while compounds with mixed Mn valence have a gradient between the colors representing the two different valences.

Inspection of the chemical formula shows that Mn ions in $Ba_3Mn_2O_8$, which all occupy the equivalent crystallographic position, have a formal valence of +5, corresponding to $3d^2$. This is a relatively rare and high oxidation state. However, for the equivalent compound $Ba_3V_2O_8$, the V ions also have a formal valence of +5, corresponding to $3d^0$. This is a relative common valence for vanadium.

The phases closest to $Ba_3Mn_2O_8$ in the ternary phase diagram are the most likely secondary phases to form during the synthesis and growth process. In particular, $Ba_3Mn_2O_8$ is close to the blue line connecting BaO and MnO_2, which marks the phases with +4 Mn valence. Steps must be taken during the growth process measures to insure that the high Mn^{5+} oxidation state is formed and not the Mn^{4+} state.

3.1.2 Polycrystalline Precursor Synthesis

$Ba_3Mn_2O_8$ polycrystalline precursor was synthesized following the previously published method [24]. The solid state process required several sinters at elevated temperatures with according to the following reaction:

$$3BaCO_3 + Mn_2O_3 + O_2(g) \rightarrow Ba_3Mn_2O_8 + 3CO_2(g) \tag{3.1}$$

Powders of $BaCO_3$ and Mn_2O_3 were weighed out according to the stoichiometric ratios for a total of 22g. The powders were combined and placed inside agate bowls with several agate balls, which were then ground in a planetary mill. The resulting mixture was pressed into pellets using a tungsten carbide die set. The pellets were placed in a horizontal Lindberg tube furnace under flowing O_2 and calcined at 900 °C for 30 hours. After the calcination the pellets were removed, reground, and pressed into pellets for two additional sinters at 1000 °C and 1050 °C for a total of roughly 100 hours. After the third sinter the pellets were a forest green color and significantly denser than the starting powders.

For the $Ba_3(Mn_{1-x}V_x)_2O_8$ polycrystalline synthesis, the stoichiometric amount of V_2O_5 powder (based on the V concentration) was substituted for Mn_2O_3 powder. The rest of the synthesis process remains the same, including the flowing O_2, which was found to improve the quality of pure $Ba_3V_2O_8$. The resulting powders were green for the syntheses with Mn concentrations of at least 0.5, light blue for $Ba_3(Mn_{0.02}V_{0.98})_2O_8$ and white for pure $Ba_3V_2O_8$.

3.1.3 Flux Growth

Single crystals were grown via a flux growth by spontaneous nucleation [40]. There are several advantages of the flux growth method. First, in a flux growth the melting point of the mixture can be significantly lowered from the melting point of each composite materials; for example, in this growth, the melting points of each of the composite starting powders as well as the desired compound $Ba_3Mn_2O_8$ are above 1500 °C, while the use of the flux, in this case NaOH, allows the growth to take place below 600 °C. Second, incongruently melting materials, which decompose into

a different solid phase and liquid than the stoichiometric compound at temperatures above the melting point of the stoichiometric compound, can be grown with the use of a flux below the peritectic temperature. Finally, the resulting crystals from flux growth are relatively free from thermal strain; there is less twinning and mosaic from such crystals. The two main drawbacks of flux growth are the relatively smaller size of the crystals (since the nucleation is not directly controlled), which can be somewhat improved through a slower cooling rate, and the likely presence of flux inclusions in the crystals, where a small amount of the solvent flux is often found in the resulting crystals.

Through significant trial and error, the only flux found to produce single crystals of the correct material was NaOH. This flux was chosen due to its oxidizing nature, a characteristic that arises because molten flux loses water to the atmosphere, leaving the very oxidizing Na_2O behind, according to the equilibria:

$$\begin{aligned} 2NaOH &\leftrightarrow Na_2O + H_2O(g) \\ Na_2O &\leftrightarrow 2Na^+ + O^{2-} \end{aligned} \tag{3.2}$$

The best growth process required mixing the polycrystalline precursor powder (for both the pure $Ba_3Mn_2O_8$ and the doped $Ba_3(Mn_{1-x}V_x)_2O_8$ material) and the NaOH flux in a 1:25 ratio. Roughly 13 total grams of material were put into a 20 mL Al_2O_3 crucible, with a cap on top to cover. Then the covered crucible was put into a firebrick enclosure which was then placed inside a Lindberg box furnace. The firebrick enclosure was necessary to prevent spilling materials inside the furnace due to boiling of the NaOH flux at elevated temperatures. The heating cycle for the growth began first with a rise from room temperature to 550 °C over 24 hours, followed by a dwell at 550 °C for 5 hours, and then a slow cool over 60 hours to 300 °C, after which the furnace was turned off. The slow heating part of the cycle ensured that the flux, which is highly volatile above room temperature, did not boil off too quickly. Even with the slow rise material usually ends up on the outside of the crucibles. The flux was removed from the resulting material by repeated washes in water, which dissolved

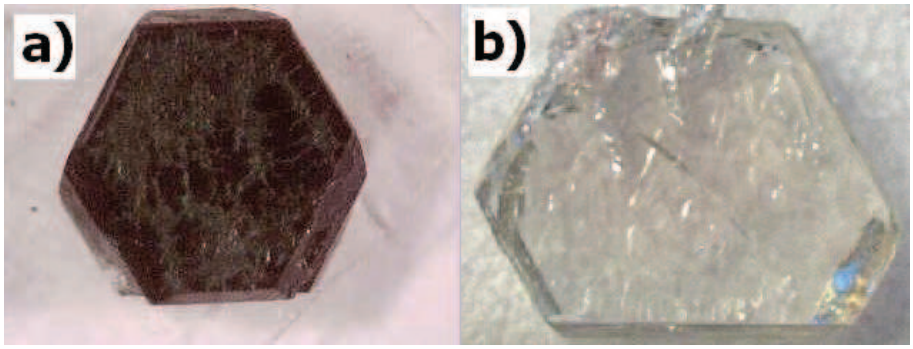

Figure 3.2: Pictures of (a) $Ba_3Mn_2O_8$ and (b) $Ba_3V_2O_8$ crystals, each roughly 1.5 mm in diameter.

the remaining NaOH flux. The resulting crystals were well formed and fully faceted (Fig. 3.2). The $Ba_3Mn_2O_8$ crystals have an intense green color, while small flakes shaved off the crystal appear lighter green. Crystals of $Ba_3V_2O_8$ are clear due to the absence of 3d electrons, and small flakes shaved off these crystals appear white.

3.2 Characterization

The primary crystal characterization measurements undertaken were X-Ray diffraction, which yielded structural information, low field susceptibility, which yielded impurity phase information, and electron microprobe analysis, which yielded elemental composition information.

3.2.1 X-Ray Diffraction

X-Ray diffraction studies were used to verify the structure of the single crystals as well as the quality of formation. Two types of measurements were undertaken: powder diffraction and single crystal diffraction studies, which yielded complimentary information about the material.

Powder diffraction studies revealed which structural phases were present in a given sample. For these measurements, the single crystals were first ground, using a agate

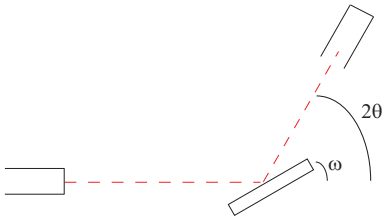

Figure 3.3: Schematic diagram of single axis diffractometer. X-rays (red dashed lines) are emitted at left, reflect on sample (rectangular box) at angle ω and are then collected in detector at angle 2θ. In the simplest diffraction experiments described here ω was fixed at one half 2θ.

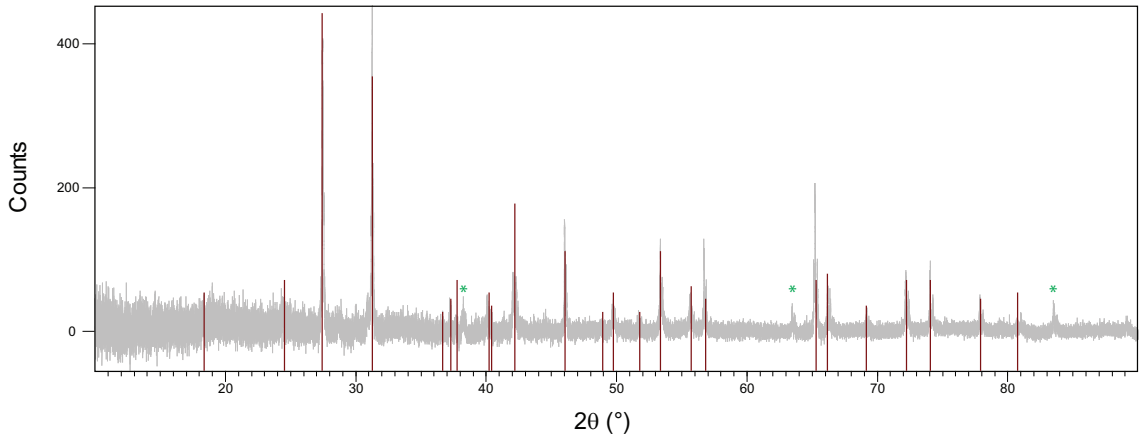

Figure 3.4: Powder diffraction of ground single crystals of $Ba_3Mn_2O_8$. The gray lines are the experimental data and the cardinal lines are the previously reported pattern [19]. Green asterisks label impurity phases, which correspond to NaOH flux inclusions.

mortar and pestle, into a powder. The powder was affixed to a glass slide using vacuum grease which was then put inside the X'Pert Pro x-ray diffraction system. The system sent Cu Kα x-rays through a divergence slit, which then diffracted off the sample and were finally collected in the detector (Fig. 3.3). For powder diffraction measurements, the sample angle ω was fixed at one half the detector angle 2θ, and both angles are scanned in concert. The background was subtracted from the resulting powder scan, which yielded the final pattern (grey line in Fig. 3.4). The pattern was then compared to the previously published data (cardinal lines) [19]. The data showed an excellent agreement with the previously published data, with less than a few percent of the total scan corresponding to impurity phases, which were primarily NaOH flux inclusions (the disagreement in the height of the peaks was due to imperfect grinding of the crystals which lead to preferential alignment of individual grains in the powder).

Single crystal diffraction studies were performed to determine the rocking curve, and thus the quality of formation, of these crystals. In this measurement, a single crystal, affixed to a glass slide, was mounted on the diffractometer. A known diffraction peak is found, with the sample at an angle ω and the detector at an angle 2θ equal to double ω. Then a sweep of ω was done while keeping 2θ constant. The resulting peak width in ω revealed the mosaicity of the crystal. The rocking curve for a single crystal of $Ba_3Mn_2O_8$ (on the strongest peak of (0,1,5)) is shown in Fig. 3.5. This curve showed a width in ω of 0.06°; this value is nearly resolution limited, indicating a very well formed crystal.

3.2.2 Low Field Susceptibility

Low field susceptibility measurements reveal both circumstantial information about the magnetic energy spectrum as well as the presence of magnetic impurities. Measurements were undertaken in a Quantum Design Magnetic Properties Measurement System (MPMS). The measurement was based on an extraction method, in which the sample was withdrawn through a set of three compensated coils to determine the

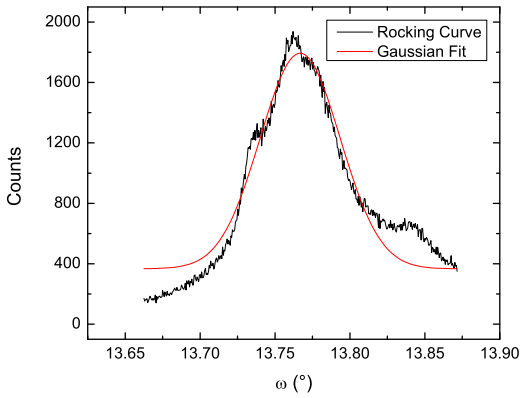

Figure 3.5: Rocking curve scan of the (0,1,5) peak of $Ba_3Mn_2O_8$. Black line shows experimental data; red line shows Gaussian fit to peak.

magnetization. The susceptibility was defined as the linear response of the magnetization, $\chi(T) = M(H,T)/H$.

In practice, samples were mounted between two straws which add a small diamagnetic background that was negligible relative to the large paramagnetic signal. The field was aligned along the length of the coil; the sample can be mounted in the straw in such a way that the field is along any axis. Measurements were performed typically at 1000 Oe or 5000 Oe for temperatures between 1.8 K and 100 K. $M(H,T)$ data confirmed that the magnetization varies linearly with field in this field range.

Experimental susceptibility data are shown in Fig. 3.6. These measurements were taken at 5000 Oe. The theoretical functional form of the susceptibility of a isolated $S = 1$ dimer system is described in Eq. 2.3. The key behavior of this model is the exponential rise of the susceptibility at low temperatures and a $1/T$ fall at high temperatures, which is observed in the experimental data. As previously described for polycrystalline samples [24], the temperature dependence of the susceptibility can be fit well to the isolated dimer model if one includes a mean field correction as well as terms relating to both magnetic and non-magnetic impurities:

$$\chi = \frac{\chi_d}{1 + \lambda\chi_d} + \frac{C}{T} + \chi_0 \tag{3.3}$$

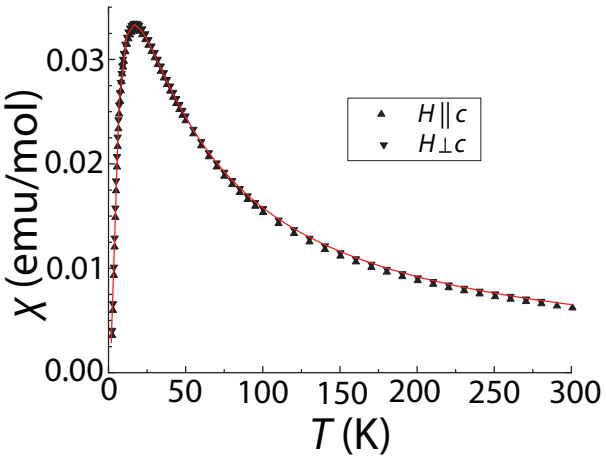

Figure 3.6: Low field susceptibility of $Ba_3Mn_2O_8$. Data shown for fields applied both along the c axis (up triangles) and perpendicular to the c axis (down triangles). Red line shows theoretical fit to the data as described in the main text.

Here $\chi'_d = \frac{\chi_d}{1+\lambda\chi_d}$ is the mean field correction which accounts for exchange with neighboring dimers with $\lambda = 3\left[J_1 + 2\left(J_2 + J_3\right)\right] / \left(Ng^2\mu_B^2\right)$. The impurities were accounted for in the Curie term (C/T) and the temperature-independent background χ_0. These fits resulted in rough estimates of $J_0 = 1.44 \pm 0.01$ meV and $g_c \sim g_a \sim 2.01 \pm 0.03$. The fit is rather insensitive to the precise value of λ (which is why this is a poor method to estimate interdimer exchange coefficients) but nevertheless returns a best value of $\lambda = 5.0 \pm 0.3$ mol/emu, which is remarkably close to the calculated value of 6.6 mol/emu based on estimates of the exchange constants $3J_1 + 6(J_2 + J_3) = 0.83$ meV obtained from previously described single crystal INS measurements [27, 28].

The impurity Curie term corresponded to just 0.4% unpaired spins, indicating the dimers were well formed throughout most of the crystal without many broken dimers. This sets a rough limit on the concentration of Mn^{4+} ions which, if randomly distributed would contribute to the Curie term. The T-independent term has a value of $\chi_0 = 2 \times 10^{-4}$ emu/mol.

3.2.3 Electron Microprobe Analysis

Electron microprobe analysis is a measurement which determines the elemental composition of a sample. Highly energized electrons are accelerated towards a solid sample where they ionize the inner shell of the atoms in the solid. As the atoms decay back to their ground state the emitted x-rays are measured. Through analysis of the wavelengths of the resulting x-rays the exact elemental shells ionized are determined, thus allowing identification of the amount each element present in the material.

To perform these measurements standard samples were used to determine the exact wavelengths expected for the pure compounds. For these measurements, the standards used were the end members of the doping series, $Ba_3Mn_2O_8$ and $Ba_3V_2O_8$, as well as elemental V for several of the samples. There was no significant difference in the results based on whether the elemental of molecular standard was used. The samples must have a microscopically flat surface for the electrons to bombard; the flat surfaces were created by polishing the samples using successively finer and finer sandpaper grits. Unfortunately, the samples could only be polished to a relatively flat surface, yielding a small error revealed in the deviation in the total number of atoms from 13. For these insulating samples a carbon coating was put on so that the charge would not build on the sample due to the incident electrons. The measurements were collected for such a time that there were at least 60000 counts of Mn and V ions total.

These measurements ultimately revealed a linear relationship between the nominal doping level and the measured doping level (fig. 3.7). Uncertainties reflect the standard deviation between multiple measurements performed at different locations for individual crystals. Systematic uncertainties for these low concentrations were likely slightly larger.

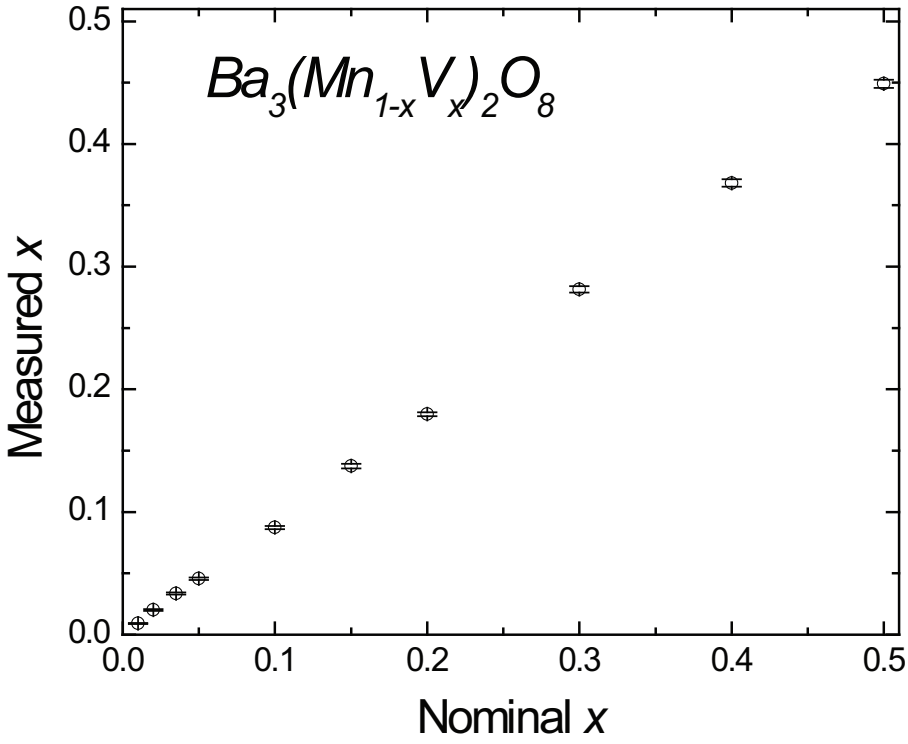

Figure 3.7: Microprobe measurement of real vs. nominal V doping level.

Chapter 4

Experimental Methods

For the specific systems I have looked at, low temperatures and high magnetic fields are required in order to reach the ordered states. While much of the important part of phase space can be accessed at Stanford using the 14 T magnet in the Fisher lab, other important measurements at higher fields required travel to the National High Magnetic Field Laboratory (NHMFL) to use higher magnetic fields. In this chapter, I will describe first the different magnets used for high fields and then the different thermodynamic measurements performed in these systems.

4.1 Magnets used in different systems

Large magnetic fields are primarily created by electromagnets, typically in a solenoid geometry wound of either superconducting or resistive wires. The standard magnets available for use in laboratories are superconducting magnets which can produce moderate fields; larger magnetic fields can be obtained from resistive magnets and pulsed magnets, which require extensive infrastructure. Typically superconducting magnets are limited to ∼20T based on the critical current density and strength tolerance of available materials. Efforts are underway to utilize new materials with higher critical current densities, such as the cuprate superconductor YBCO, to achieve higher magnetic fields. Resistive magnets can produce magnetic fields up to 36 T, and if used in combination with a superconducting "outsert" magnet can produce 45 T in

a "hybrid" magnet. Finally, pulsed magnets can create even higher magnetic fields for small bursts at a time. Each of these different types of magnets were used in this thesis.

4.1.1 Superconducting Magnets

The advantage of superconducting magnets stems from the defining characteristics of superconductivity: the non-dissipative flow of current in a system. This zero resistivity allows current, once flowing, to (ideally) flow in perpetuity. Power is needed only initially to reach the desired current and by extension the desired field, and no further electrical power is used to maintain that current.

Superconducting magnets only function as intended below the critical temperature of the superconductor material used. For the typical materials used, Nb_3Sn and NbTi which have critical temperatures of 18 K and 10 K respectively, this requires cooling the magnets with liquid Helium to 4.2K. The magnet is connected to an external current source which increases the current; once the desired current is achieved the external current source can be shut off and removed, leaving a closed loop in the superconducting solenoid. In order to maintain the full level of the non-dissipative current flow the magnet must be constantly submerged in liquid helium while in use to avoid warming up the magnet due to various sources of heating. The magnet is decoupled from the sample chamber via means of a heat switch. Although the electrical power used to run superconducting magnets is limited while sitting fixed at a field there is a large charge required to maintain the cold temperatures through use of cryogens. Measurements were performed in several superconducting magnets, including a 5 T magnet in the Quantum Design system Magnetic Properties Measurement System (MPMS), a 14 T magnet in the Quantum Design system Physical Properties Measurement System (PPMS), and an 18 T magnet at the NHMFL, Tallahasse.

4.1.2 Resistive Magnets

Resistive magnets work by a very simple process: pass as much current as possible through a conductor. These magnets are termed resistive because in contrast to the

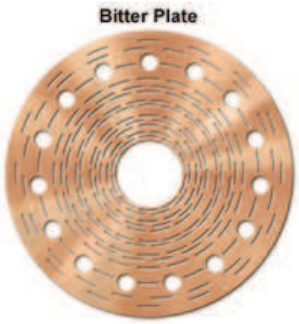

Figure 4.1: Schematic view of bitter disk, showing the cooling slits. Figure taken from NHMFL website [41].

superconducting magnets, which have non-dissipative current flow, these magnets are made of standard ohmic materials. Thus power, proportional to the square of the current, will be lost while field is being generated in the magnet; at full field a resistive magnet can use 20 MW. The cost of running a resistive magnet is 100 times greater than a superconducting magnet due to the expense of the power necessary. It is the energy cost, as well as the associated cooling water needs, that determines the maximum field achievable from a resistive magnet.

Resistive magnets are made up of a series of bitter plates interspersed with insulators. Bitter plates are metal discs (made of copper or a copper alloy at the NHMFL) which form the coils of the solenoid (Fig. 4.1). These discs have small slits in them. These slits allow deionized water to flow through the magnet at a rate of 15000 liters per minute, which keep the magnet from getting too hot due to resistive heating induced by the large current. The slit design of the disks serves to maximize the cooling power while minimizing the increase in resistance relative to other hole designs. The interspersed insulating layers cover less than a full turn so that current can flow between the successive layers. The top and bottom disks experience an uncompensated centripetal force due to the gradient field which can cause these disks to become misaligned. To account for this misalignment the end disks are slightly bigger and have larger slits. Several concentric solenoids are nested within each other, and the current runs in series through these coils to create the full field. Heat capacity, magnetocaloric effect measurements and dilatometry measurements were performed

in fields up to 36 T at the NHMFL, Tallahassee.

4.1.3 Hybrid Magnet

The hybrid magnet is, as its name suggests, a hybrid of a superconducting and resistive magnets. The idea behind this magnet is to increase the maximum field of the system by combining the fields produced by a superconducting magnet and a resistive magnet. The superconducting magnet is placed concentrically outside the resistive magnet (Fig. 4.2); the order cannot be switched because the resistive magnet creates a field larger than the critical field of the superconductor. The superconducting magnet has an extremely large radius to accommodate the insert resistive magnet, limiting the total field achievable by the superconducting magnet to 11 T while also requiring very large amounts of liquid Helium to keep the magnet below the critical temperature of the superconductor. The field in the superconducting magnet is ramped very slowly because of its large radius. The full hybrid system at the NHMFL, Tallahassee, by taking the superconducting magnet in combination with the 34 T resistive magnet, can produce 45T, the largest available DC field in the world. Heat capacity and magnetocaloric effect measurements were undertaken on this system.

4.1.4 Pulsed Magnet

The pulsed magnets at the NHMFL, Los Alamos, have the ability to reproducibly generate magnetic fields exceeding those available from DC systems for short durations, lasting 1-100 ms at full field and between 20-2000 ms for the full period (see 60T pulse profile in Fig. 4.3). These magnets are powered by a series of capacitor which combined can store 1.6 MJ. The magnets are composed of solenoid coils made of copper with fiber glass reinforcement between each copper layer to maintain a more uniform field profile. The materials of the magnet must be able withstand the exceedingly high pressures of up to 1.4 GPa which are felt by the coils while the magnetic field is created. While most of the energy from the capacitor bank is released as magnetic field a portion is also released as heat into the coils. To combat this, the

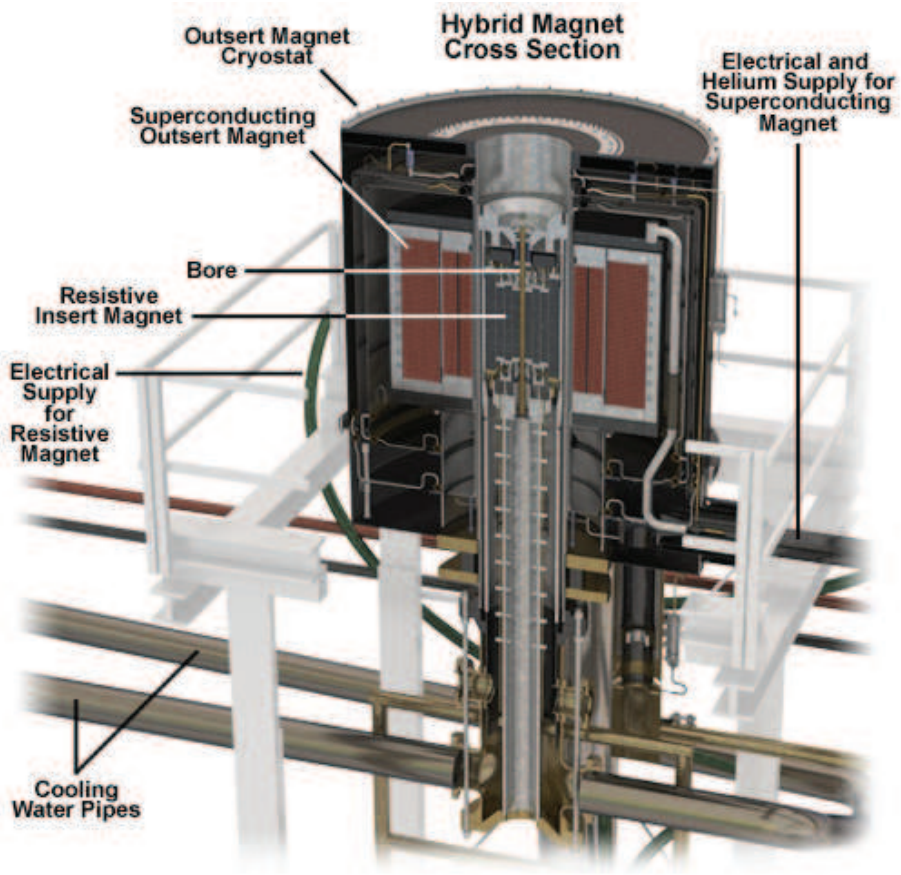

Figure 4.2: Schematic of hybrid magnet, showing both the inner resistive magnet and the outer superconducting magnet. Figure taken from NHMFL website [41].

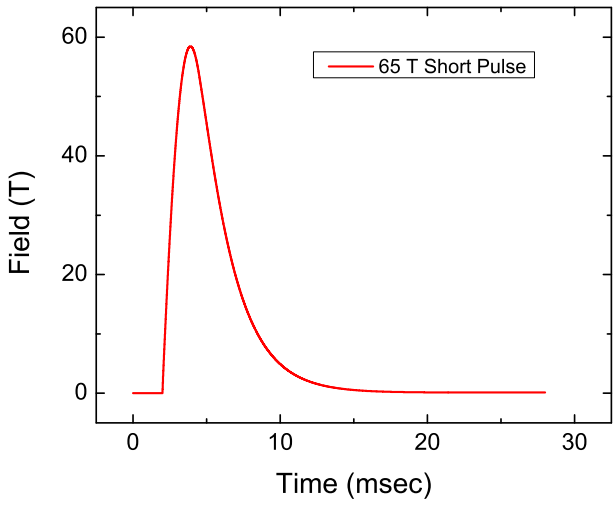

Figure 4.3: Field profile of 60T shot from pulsed magnet.

coils are submerged in liquid nitrogen to maintain a baseline temperature. The frequency at which the magnet can be fired is limited primarily by the need to cool the coil down to its baseline temperature, and for a full field pulse to $\geq$ 60T can require waiting for 1 - 2 hours. These magnets will fail (often spectacularly, including a large boom followed by melting of the coil) after on average 750 field pulses due to the repeated mechanical stresses acted on the coils by the large pressures. Magnetization measurements were undertaken in both 50 T and 65 T pulsed magnets.

4.2 Thermodynamic Measurements

Most of the experiments of this thesis were thermodynamics measurements. These measurements give information about basic macroscopic quantities, like the magnetization, which can often be related to the free energy and ultimately the critical ordering temperatures.

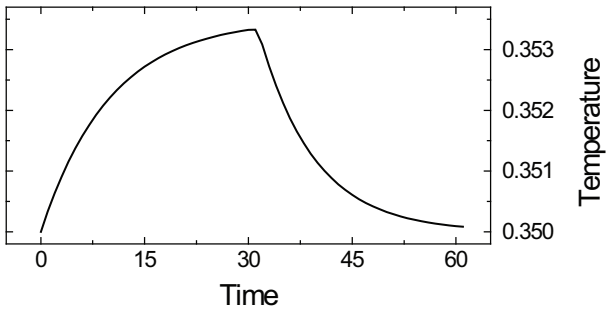

Figure 4.4: Schematic graph illustrating temperature versus time of specific heat measurement determining decay time constant

4.2.1 Specific Heat and Magnetocaloric Effect Measurements

Heat capacity and magnetocaloric effect (MCE) measurements were undertaken both in the Quantum Design Physical Properties Measurement System (PPMS) in Quantum Design calorimeters and at the NHMFL, Tallahassee in a home built calorimeter. The heat capacity and MCE measurements are complimentary and can be performed on the same calorimeter.

Thermal relaxation specific heat measurements are performed on calorimeters which have a sample connected by a weak link to the bath. The measurements are performed by applying a small amount of heat and allowing the temperature to asymptotically decay to a final temperature (see Fig. 4.4). The decay time constant τ is then determined from the time dependence of the temperature, while the specific heat is proportional to that decay constant [42]:

$$\begin{aligned} T &= T_0 + \Delta T \exp\left(-t/\tau\right) \\ C &= \kappa\tau = \frac{-\kappa\left(T - T_0\right)}{dT/dt} \end{aligned} \tag{4.1}$$

The constant of proportionality, κ, is the thermal conductivity of the weak link connecting the sample to the bath. Alternatively, by tracking the amount of heat pumped into the sample in addition to the temperature the heat capacity can be directly measured, allowing for a secondary measure of the the thermal conductivity.

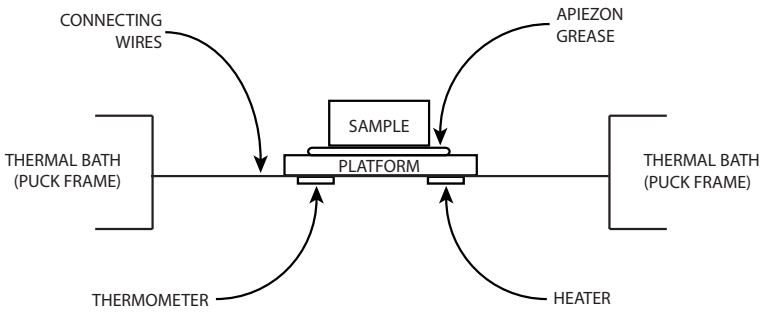

Figure 4.5: Schematic diagram of heat capacity/MCE calorimeter.

The heat capacity typically is measured by computing the averaging value of the heat capacity over the temperature range of the heat pulse to yield a single data point, and then taking a series of heat pulses at different starting temperatures to get a full heat capacity curve. Alternatively, in the large ΔT limit, a larger pulse of heat is applied, causing the temperature of the sample to track over a larger range. This yields then a full heat capacity curve from a single heat pulse by computing the instantaneous decay constant over the entire temperature range. The former method has better statistics by averaging over an entire range, while the latter method has an advantage in expediency such that each measurement can be performed more quickly.

A schematic diagram of the heat capacity calorimeter is shown in figure 4.5. The sample is affixed to the platform using either apiezon N grease, in the case of the PPMS, or GE varnish, in the case of the calorimeter used at the NHMFL. On the underside of the platform is both a heater and thermometer. The wires from the heater and thermometer to the puck frame, which constitutes the thermal bath, can form the link from the sample to the bath; additional links may be necessary to hold the platform in place and connect the sample to the bath.

While specific heat measurements give information about the entropy (and by extension ordering) of a system as a function of temperature, magnetocaloric effect measurements give similar entropic information but as a function of magnetic field. MCE measurements are performed under quasi-adiabatic conditions, where the temperature is tracked as the field is swept. The entropy change of a sample is dependent both on inherent heat capacity of the sample as well as the thermal link to the bath:

$$\delta S = -\frac{C\delta T + \kappa\left(T - T_{bath}\right)}{T} \tag{4.2}$$

Calorimeters may be in two different regimes: 1) the strong link regime, where the entropy change of the system is dominated by the connection to the bath ($\delta S \simeq -\kappa\frac{T-T_{bath}}{T}$) such that a temperature shift associated with a phase transition will be quickly damped to the bath temperature, or 2) the weak link regime, where the entropy change of the system is dominated by the inherent heat capacity of the system ($\delta S \simeq -C\frac{\delta T}{T}$) such that the sample can maintain an elevated temperature while scanning field. Each calorimeter used in this thesis was in the strong link regime.

A crucial parameter for MCE measurements is the rate of change of the magnetic field with time. This defines what constitutes quick dampening, and by extension determines the field width of each transition. Additionally, a faster sweep rate will make a peak or dip associated with a transition larger in temperature while still containing the same amount of entropy. Measurements conducted in the resistive and hybrid magnets at the NHMFL, with assistance from M. Jaime, had field sweep rates of 1-5 T/min, while measurements conducted in the superconducting magnet of the PPMS had slower field sweep rates of 0.05 - 0.3 T/min.

4.2.2 Magnetostriction Measurements

Magnetostriction measurements are sensitive measures of the change in the lattice parameters of a system as the field is swept. The method used to measure lattice expansion is capacitive dilatometry [43]. In this arrangement a sample is connected to the bottom plate of parallel plate capacitor which follows the well-known expression for a parallel plate capacitor:

$$C = \frac{\epsilon_0 A}{D} \tag{4.3}$$

.

Here C is the measured capacitance, D is the distance between the two plates and A is the area of the plates. The length of the sample directly sets the separation of

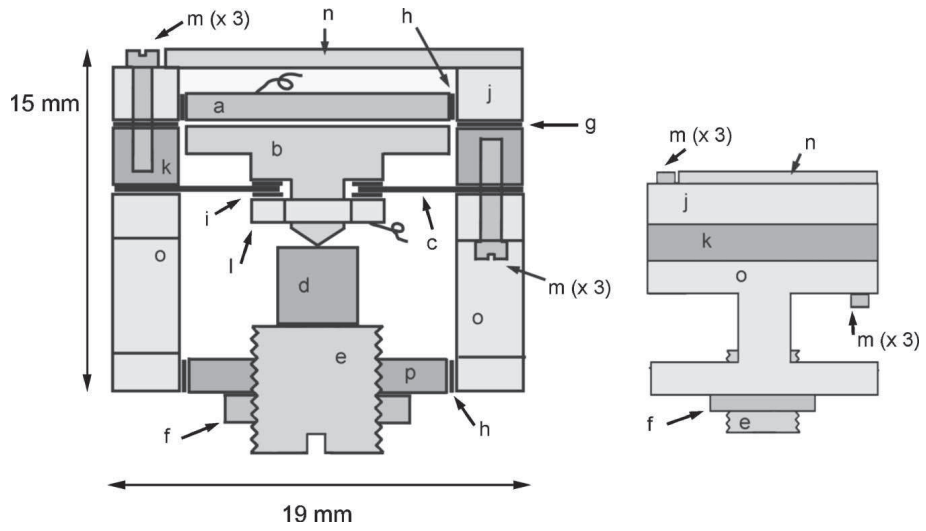

Figure 4.6: Diagram of capacitive dilatometer. The sample is labeled 'd', and the parallel plates are labeled 'a' and 'p'. Figure taken from [43].

the two plate D such that the linear magnetostriction, $\lambda = [L(H) - L(0)]/L(0)$, can be easily calculated by relating the length of the sample by measuring the capacitance C.

The design for the dilatometer is shown figure 4.6. The sample, labeled 'd', is affixed to a screw, labeled 'e', with GE varnish. This screw is tightened until the sample touches the point of 'b', the bottom plate of the capacitor which is machined so that it has a point on the side opposite the capacitor. Springs, labeled 'c', attach the lower parallel plate to outside platform by being held between two washers and a nut labeled 'l'. This allows the lower plate to move freely up and down as the sample expands/contracts while the upper plate of the capacitor, labeled 'a', is fixed. Thus as the sample expands (contracts), the lower capacitor plate will move closer to (further from) the upper plate, and the change in the distance between the two plates is the negative of the change in the length of the sample:

$$L(H) - L(0) = -\left(D(H) - D(0)\right) \tag{4.4}$$

Using this expression and the measured length of the sample at 0 field, the linear magnetostriction is easily computed as a function of the capacitance $C(H)$:

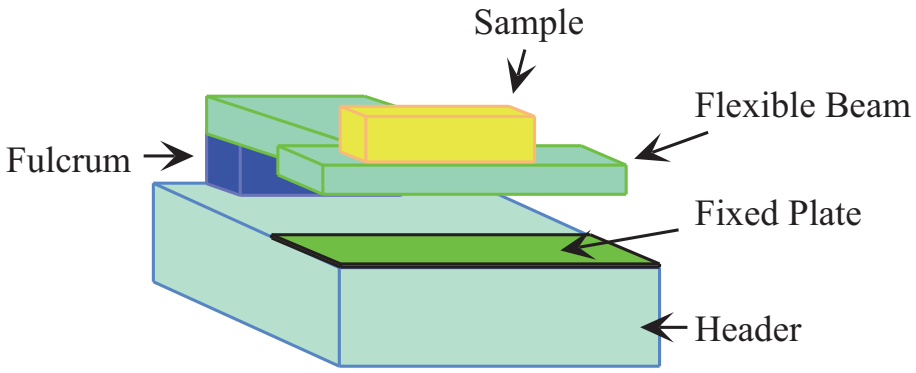

Figure 4.7: Schematic design of capacitive magnetomter used for torque magnetization measurements. Figure taken from [44].

$$\lambda = [L(H) - L(0)]/L(0) = \frac{\epsilon_0 A\,(C(H) - C(0))}{L(0)\,(C(H)C(0))} \tag{4.5}$$

Magnetostriction measurements were undertaken with the assistance of G. Schmiedeshoff in a ^{3}He refrigerator in a 35 T resistive magnet at the NHMFL.

4.2.3 Torque Magnetization

Torque magnetization measurements are very sensitive measures of phase transitions. For an anisotropic material, principal axes can be found for which the g-tensor is diagonal (for high symmetry samples, like the rhombohedral system studied here, this corresponds to the crystalline axes). For fields applied parallel to one of these axes the resulting magnetization will be parallel to the field, such that the torque, equal to the crossproduct of the magnetization and the field, will be zero. If, alternatively, fields are applied away from one of these principal axes, the resulting magnetization will not be exactly parallel with the applied field. If, for instance, the field is applied at an angle θ between the crystalline c and a axes, the resulting magnetization has the following form (the field axis is defined as the z axis, following earlier nomenclature) [45]:

$$\begin{aligned} M^z &= \mu_0 H \left[g_{cc} \cos^2(\theta) + g_{aa} \sin^2(\theta) \right] \\ M^x &= \mu_0 H \left[-g_{cc} + g_{aa} \right] \sin(\theta) \cos(\theta) \end{aligned} \tag{4.6}$$

This misalignment between the magnetization and field in turn creates a torque:

$$\tau = \mathbf{M} \times \mathbf{H} = \mu_0 H^2 \sin(\theta) \cos(\theta) \left[-g_{cc} + g_{aa} \right] \hat{y} \tag{4.7}$$

Torque magnetization measurements are performed by affixing a sample to the flexible beam (the cantilever), typically with GE varnish, forming one half of a parallel plate capacitor (see Figure 4.7) [44]. The second plate of the capacitor is fixed to the header, which is attached to the mounting stage where heaters and thermometers can be placed. The entire sample stage is encased in a can which is grounded. The torque range that can be measured is set by the stiffness of the cantilever, which is in turn determined by its thickness and its material. For this thesis CuBe cantilevers were used. Measurements were performed with the assistance of Y.-J. Jo and L. Balicas in a superconducting magnet at the NHMFL in a dilution refrigerator.

4.2.4 Magnetization in Pulsed Fields

Extraction magnetization measurements are conceptually easy measurements which require careful implementation to extract the data from the noise. A coil is wrapped around the sample, and during the magnetic field pulse the magnetization will rapidly change, inducing a voltage in the coil. By measuring both this time derivative of the magnetization as well as the time derivative of the field, the field derivative of the magnetization and by extension the magnetization itself are easily calculated [46]. In practice, one must be very careful to separate the signal of the sample from the signal of the coil alone. This is done by having two counter-wound coils of equal area such that each coil will pick up the same (opposite) voltage and yield no voltage due to the external applied field. In addition, an secondary compensation coil is put around the magnetometer which is used as a background. The outside coil signal is

subtracted from the inner counter-wound coils, with the difference multiplied through a 50000x amplifier to yield the final result. In practice, each measurement requires an additional background shot of the empty magnetometer which is subtracted from the sample measurement. This requires that the sample can be moved in and out of the magnetic field *in situ* such that the rest of the experimental setup can remain the same. An additional coil must be put outside the main magnetometer to directly measure time derivative of the field.

The sample is put either directly inside the coils or instead inside a nonmagnetic plastic case to hold the sample. Each arrangement has benefits: the plastic case setup leads to lower noise while the setup with the sample directly inside the coil allows for better thermal contact and ultimately lower temperatures. In both setups it is crucial to maximize the amount of material inside the coil to get a better signal to noise ratio. The specific geometry of the resulting samples are cylindrical (or at least oblong) and roughly 1-1.5 mm long with a 200 μm diameter.

Measurements were performed with the assistance of R. McDonald in pulsed magnets at the NHMFL, Los Alamos in a ^{3}He refrigerator.

Chapter 5

Singlet-Triplet Regime

The ordered states of the singlet-triplet regime of $Ba_3Mn_2O_8$ have several characteristics that previously studied spin dimers did not have. I have studied these ordered states through several different thermodynamic measurements which have painted a picture about their microscopic nature. In this chapter I will first describe the numerous measurements undertaken in this regime; then through analysis of the Hamiltonian I will compare the calculated critical fields to the measured critical fields and finally I will propose different possible forms for the microscopic nature of these ordered states. This work is published in refs. [29, 31, 33].

5.1 Experimental Results

A wide variety of measurements were used to probe the singlet-triplet regime, all requiring fields above 9 T and temperatures below 1 K to access the ordered states. These measurements mapped out the phase boundary of these ordered states and also provided further circumstantial information about the nature of the phase transitions.

5.1.1 Heat Capacity and Magnetocaloric Effect

Heat capacity measurements of single crystals of $Ba_3Mn_2O_8$ in the singlet-triplet regime were performed both on a home built calorimeter down to 0.35 K for fields up

to 30 T at the NHMFL and also in commercial PPMS calorimeter at fields up to 14 T and down to 0.35 K. These measurements revealed significant anisotropy depending on the direction that field was applied.

The heat capacity, scaled by temperature, is plotted as a function of temperature and fields for field applied along both the c and a axes in Fig. 5.1 (a) and (b) respectively. For fields greater than H_{c1} applied parallel to the c-axis there is only one phase transition in this regime. This ordered state is labeled phase I to distinguish from a second distinct phase observed for fields parallel to the a-axis. The data show a lambda-like transition, suggestive of 3D XY ordering. The value of the peak height (in C_p/T) increases as the field is increased from H_{c1} up to the maximum field for which data was taken for this orientation, indicative of an increasing entropy, although quantitative estimates are difficult given the small temperature range and large background associated with gapped magnetic states. These data points are included as solid square symbols in the phase diagram shown in Fig. 5.6(a).

For fields oriented parallel to the a-axis, heat capacity data were taken up to $H_{c2} \sim$ 26 T (Fig. 5.1(b)). These data show a remarkable sequence of phase transitions at low temperature with an unusual division of entropy. For fields between 9 and 11 T just one transition is observed above 0.35 K; between 11 and 13 T two distinct transitions are clearly resolved; for intermediate fields, only a single transition; between 24 and 25 T two transitions are again observed; and finally close to the triplet saturation field of $\sim$26 T only one transition is observed. Anomalies in the heat capacity marking these phase transitions are joined by lines in Fig. 5.1(b), and T_c values included in the phase diagram shown in Fig. 5.6(b) as solid symbols. The heat capacity anomaly for phase transitions joined by the solid blue line in fig. 5.1(b) are lambda-like, similar to those observed for fields parallel to the c-axis, and accordingly the ordered state marked by this transition is labeled phase I. The value of the peak height of this transition (in C_p/T) first rises with field, and then after H is increased beyond the midpoint of this regime, reduces in magnitude again. In contrast, the anomaly associated with the phase transitions connected by the dashed red lines in Fig. 5.1(b) are less divergent, and although the data do not permit a critical scaling analysis, nevertheless are more suggestive of an Ising transition; this state is labeled

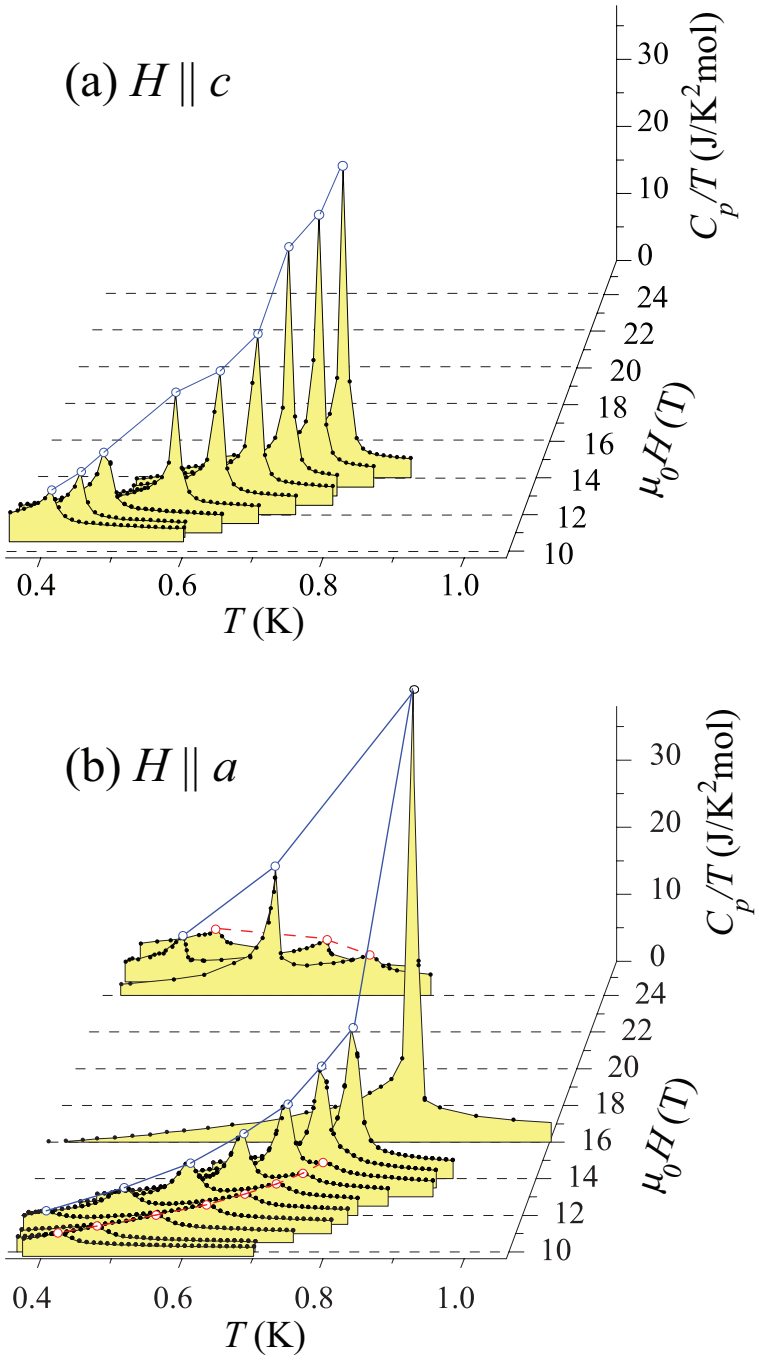

Figure 5.1: Heat capacity (shown as C_p/T) as a function of temperature and fields for fields applied (a) parallel and (b) perpendicular to the c axis. The solid blue (dashed red) indicate the transition into phase I (phase II) from higher temperatures as determined by peaks in C_p/T as a function of field.

as phase II. The rise in C_p/T associated with this phase transition does not appear to vary with field within the uncertainty, indicating that the change in entropy is only weakly dependent on the applied field. Estimates of the integrated entropy are difficult due to the close proximity of the second phase transition, and also due to the large background magnetic contribution to the heat capacity associated with the other gapped states. However, a crude estimate of this entropy was obtained for several fields for which the only resolvable transition is between the disordered phase and phase II (plotted in Fig. 5.2(c) for $H = 10.5$ T). Upper and lower bounds for the entropy were determined by assuming a minimum and maximum possible background, shown as blue and red lines respectively in Fig. 5.2(c), yielding an average of 0.45 $\pm$ 0.20 J/molK. Within the uncertainty, this value appears to be symmetric for fields above and below the midpoint of H_{c1} and H_{c2} as shown in Fig. 5.2(d), and for this reason the ordered state on the right hand side of Phase I in Fig. 5.6(b) is labeled as phase II.

MCE measurements, performed up to 30 T and down to 0.35 K for fields both parallel and perpendicular to the c axis, also probed the singlet-triplet ordered states. Phase transitions are evident from a sharp increase (decrease) in the temperature of the sample on entering (leaving) the ordered state (see Fig. 5.4). In practice, points on the left (right) hand side of the phase diagram were determined from a sharp peak (trough) in the first derivative of the temperature with respect to field taken on up (down) field sweeps, each corresponding to the case of entering the ordered state (see Fig. 5.3). These data are in close agreement with heat capacity measurements, with small differences being ascribed to differences in sample alignment and, where two different calorimeters were used, thermometry (Fig. 5.6). A slight asymmetry in the magnitude of the change in temperature between up and down sweeps provides evidence that transitions between the disordered state and phase I, between the disordered state and phase II, and between ordered phases I and II are all weakly first order in this temperature range.

Additional temperature independent features were found centered at H_{c1} and H_{c2}. These features do not mark phase transitions but rather are a consequence of the

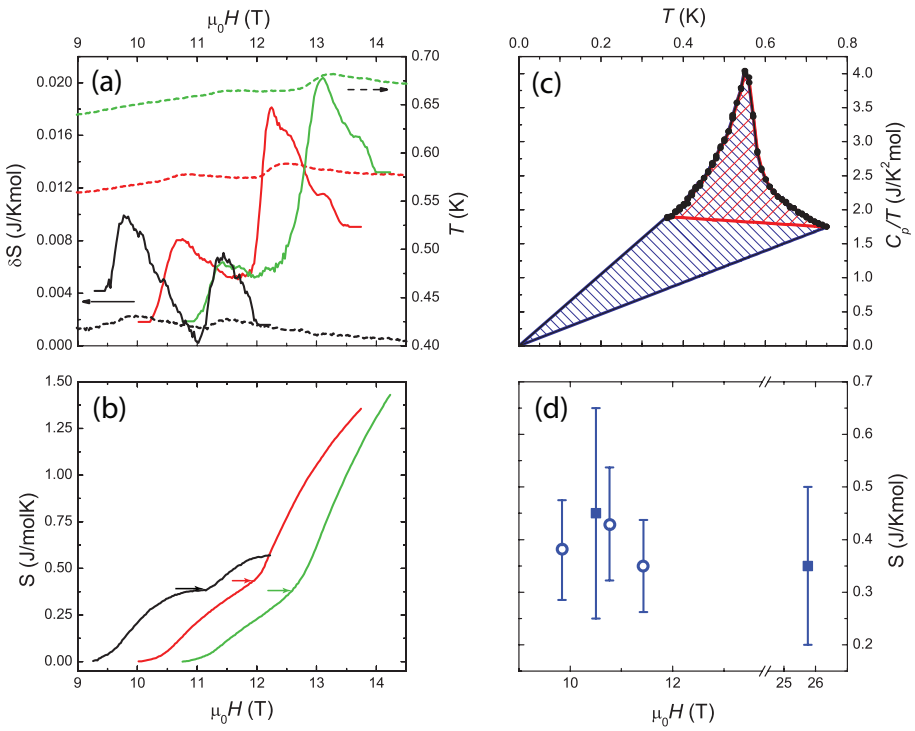

Figure 5.2: Entropy estimates for phase II for fields oriented parallel to the a-axis. (a) Three representative MCE measurements (dashed lines, right axis) and the corresponding change in entropy, δS_i, (solid lines with the same color, left axis). (b) Total entropy associated with phase transitions seen in MCE measurements, calculated as described in the main text. Horizontal arrows indicate the entropy associated with the lower transition. (c) Upper and lower bounds of the integrated entropy associated with the phase transition observed in heat capacity at 10.5T. (d) Entropy on entering phase II from MCE (open circles) and C_p (solid squares).

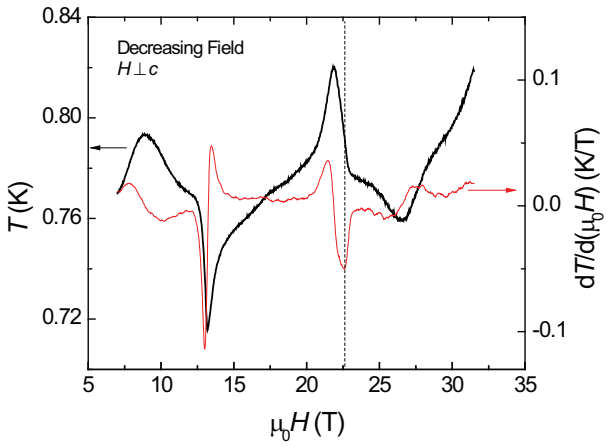

Figure 5.3: MCE curve (shown in black) and its field derivative (shown in red) for decreasing field. The phase boundary point is determined from a peak in the field derivative associated with the rapid change in temperature on entering into the ordered state and is marked by a vertical dashed line at $\sim$ 22.6 T.

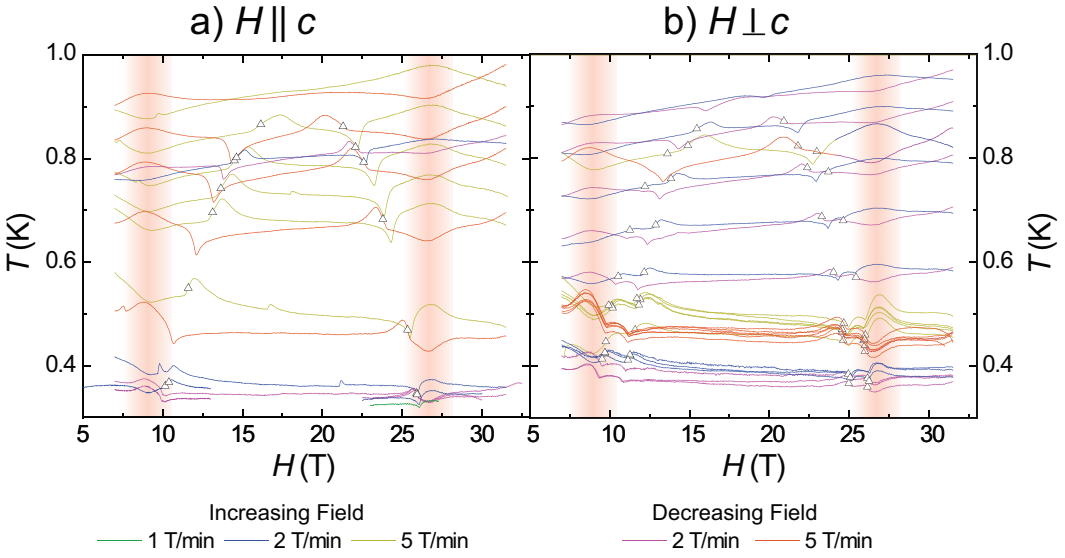

Figure 5.4: MCE curves for increasing and decreasing fields at different rates for fields applied parallel (a) and perpendicular (b) to the c axis. Shaded vertical bands are guides to the eye to draw attention to the broad features observed in MCE measurements centered at 8.8T and 26.5T. MCE traces are shown in green, blue and yellow for increasing fields for sweep rates of 1, 2 and 5 T/min, respectively and purple and red for decreasing fields for sweep rates of 2 and 5 T/min, respectively. Representative data for increasing fields are designated by arrows and shown in blue for sweep rates of 5 T/min in panel (a) and 2 T/min in panel (b).

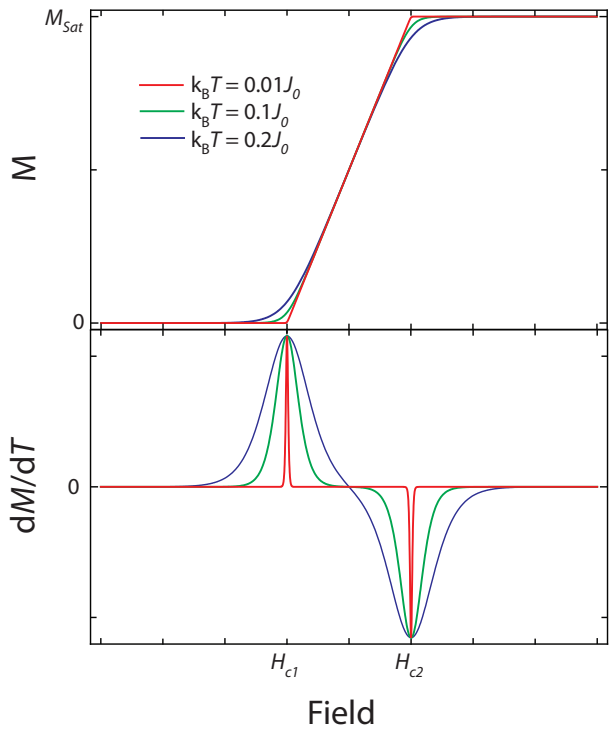

Figure 5.5: Magnetization (a) and the temperature derivative of the magnetization (b) of a $S = \frac{1}{2}$ dimer system with interdimer exchange J at several temperatures.

rapidly changing magnetization as a function of temperature. Using Maxwell's equations, the change in magnetization with temperature can be related to the change in entropy with field:

$$\frac{\partial M}{\partial T}|_{H,P} = \frac{\partial S}{\partial H}|_{T,P} \tag{5.1}$$

This effect is demonstrated in Fig. 5.5 for a model dimer system composed of two spin $\frac{1}{2}$ moments. The excited triplet band is modeled as having a uniform density of states, which leads to a linearly increasing magnetization between the minimum of the triplet band H_{c1} and the maximum of the triplet band H_{c2}. The sharp increase (decrease) in the slope of the magnetization at H_{c1} (H_{c2}) at 0 K is rapidly smeared out at higher temperatures. This change in the slope leads to a peak in the temperature derivative of the magnetization, which goes from delta like at 0 K to shorter and broader humps at higher temperatures.

The total change in entropy associated with a phase transition can be calculated

from MCE measurements by summing the increase in entropy of the system plus the entropy lost as heat to the bath from the sample stage:

$$\delta S_i = -\frac{C\left(T_{i+1} - T_i\right) + \kappa\left(T_i - T_{base}\right)}{T_i}, \tag{5.2}$$

where i labels successive temperature points taken as the field is swept (typically 40 evenly spaced points per Tesla) and κ is the thermal conductivity of the thermal link in the calorimeter. A linear interpolation for κ was calculated as a function of temperature and field for the calorimeter, and values of the heat capacity were taken from measurements performed in the PPMS calorimeter. Figure 5.2(a) shows three representative MCE data sets for fields oriented perpendicular to the c-axis (dashed line, right axis), and the associated change in entropy δS_i between successive data points (solid curves, left axis). All three data sets were taken for increasing fields and for the same sweep rate of 2 T/min. As can be seen, δS_i shows two successive peaks as a function of field, which correspond to the two phase transitions. A practical measure of the change in entropy associated with each phase transition is therefore provided by the integrated entropy up to the minimum in δS_i, which is shown in Fig. 5.2(b). For the lowest temperature data set (black curves) the two transitions are well separated and the total entropy associated with the first transition exhibits a clear plateau. For the higher temperature sweeps (lighter color curves) the two transitions are slightly closer in field, and the total entropy exhibits more of a kink than a plateau. Nevertheless, these data allow an estimate of the integrated entropy associated with each transition into phase II from the disordered phase, which are plotted in Fig. 5.2(d) for these and some additional intermediate temperature sweeps. Within the uncertainty of this analysis, the change in entropy associated with entering phase II from the disordered state is essentially independent of temperature, with an absolute value that agrees remarkably well with the value extracted from heat capacity measurements (square symbol in Fig. 5.2(d)). In contrast, the change in entropy associated with entering phase I depends strongly on temperature, consistent with inspection of the heat capacity data shown in Fig. 5.1(b).

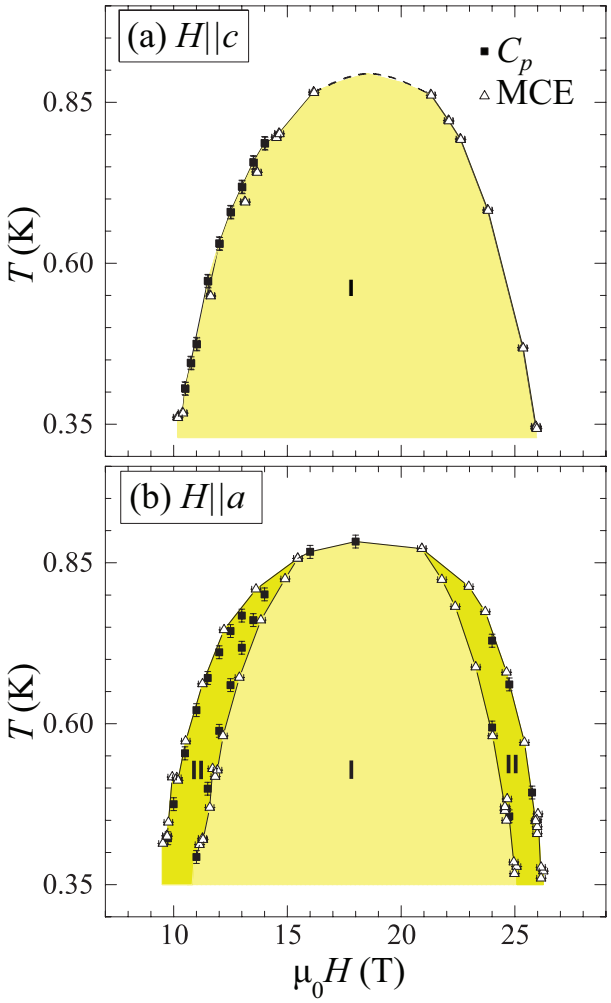

Figure 5.6: Phase diagram obtained from heat capacity (solid squares) and MCE (open triangles) measurements for fields applied (a) parallel and (b) perpendicular to the c axis. Labels indicate Phases (I) and (II), as described in the main text. Dashed line in panel (a) indicates the anticipated phase boundary for fields between 16 and 21 T based on similar data in panel (b)

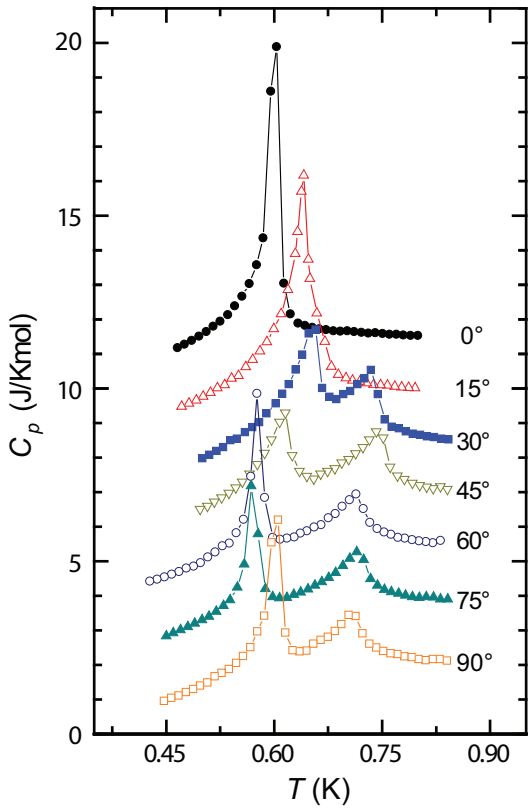

Figure 5.7: Representative heat capacity data taken at 12T for fields in the a-c plane. Labels indicate the angle between the field and the c axis. Successive data sets are offset vertically by 1.6 J/molK for clarity.

Heat capacity measurements were also undertaken to determine the angular dependence of these two phases. The measurements were performed in the PPMS for four different fields and seven different angles. The sample was mounted on angled brackets, machined within 1° accuracy, made from oxygen-free high conductivity copper and the field was oriented in the [100]-[001] plane.

Representative heat capacity measurements, taken at 12 T for several angles, are shown in Figure 5.7. These data show a single peak for fields aligned along the c axis, a peak and a shoulder for fields 15° from the c axis and two peaks for larger angles. Significantly, comparison of the data at 75° and 90° degrees shows that the 75° data has both a slightly higher critical temperature between the paramagnetic phase and phase II ($T_{c_{II}}$) and also a substantially lower critical temperature between phase II

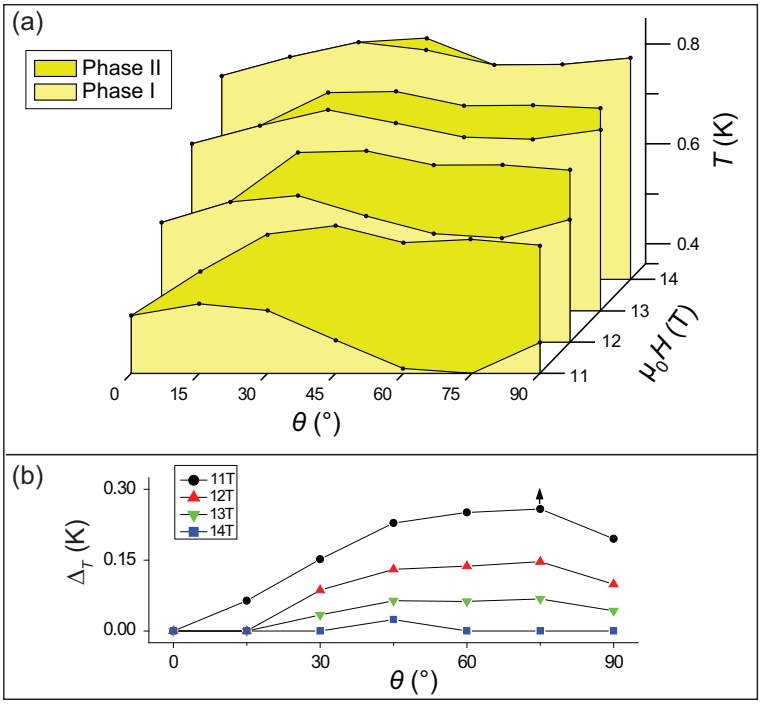

Figure 5.8: (a) Phase diagram showing the transitions between the paramagnetic state and phase II (T_{II}), and between phase II and phase I (T_I), as a function of temperature and angle in the [100]-[001] plane for various fields, where θ indicates the angle between the field and the c axis. (b) Width of phase II, $\Delta_T = T_{c_{II}} - T_{c_I}$, as a function of angle for 11T, 12T, 13T and 14T (black circles, red up triangles, green down triangles, and blue squares, respectively.)

and phase I (T_{c_I}) than the 90° data.

The phase diagram derived from the complete set of angular C_p measurements, shown in Fig. 5.8(a), reveals the evolution as a function of angle of the two distinct singlet-triplet ordered states for fields in the [100]-[001] plane. The data show a single transition for all fields for $H \| c$ and two transitions for $H \| a$. The extent in temperature of phase II, $\Delta_T = T_{c_{II}} - T_{c_I}$, is shown in Figure 5.8(b). Δ_T increases as a function of angle as the field is rotated away from the c axis, reaches a maximum at 75°, and decreases at the a axis (90°). For example, for a field of 11T, Δ_T is $\sim$ 0.07 K larger at 75° than at 90°.

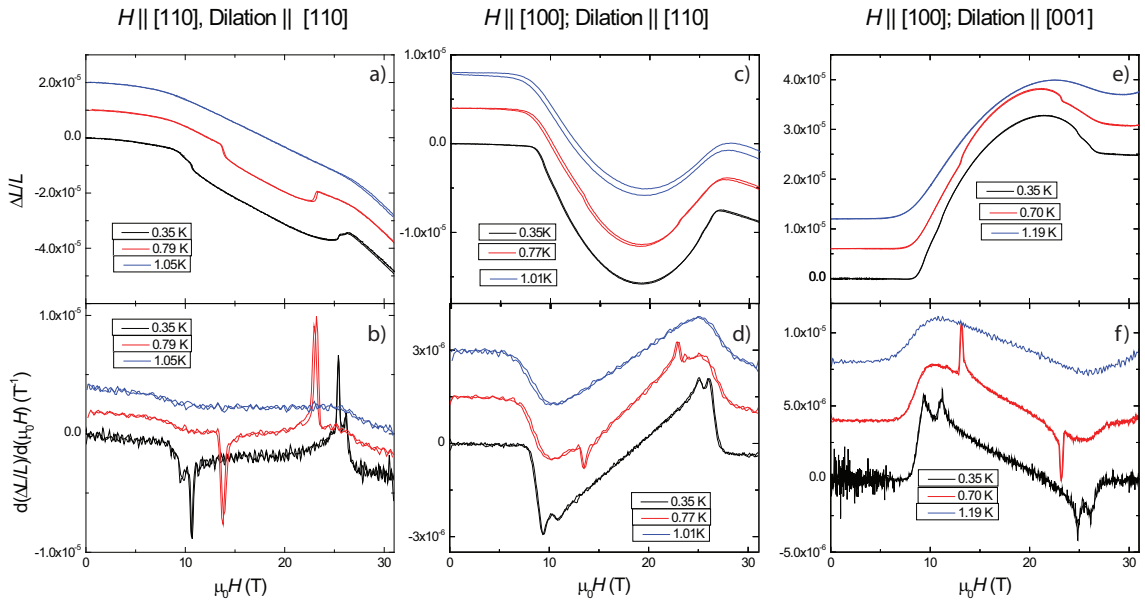

Figure 5.9: Linear coefficient of magnetostriction and its first derivative with respect to field for the three orientations measured. Successive curves offset by $1*10^{-5}$, $2*10^{-5}$ T^{-1}, $4*10^{-5}$, $1.5*10^{-6}$ T^{-1}, $6*10^{-5}$ and $4*10^{-6}$ T^{-1} for panels a) - f), respectively.

5.1.2 Magnetostriction

Magnetostriction measurements were performed on single crystals of $Ba_3Mn_2O_8$ for fields through the singlet-triplet ordered states. Due to limited access to the resistive magnet at the NHMFL no estimate of the background magnetostriction associated with the dilatometer was obtained. These measurements were performed for three different field axis / dilation axis orientations: 1) Field along [110], dilation along [110]; 2) Field along [100], dilation along [110]; and 3) Field along [100], dilation along [001]. Taken together, these sets of measurements cover all possible dilation directions for fields applied in the plane (recall that in hexagonal nomenclature the [100] and [110] directions are perpendicular). Measurements were performed for several temperatures between 1.1 K and 0.3 K. These measurements revealed two transitions near both H_{c1} and H_{c2} at low temperatures.

Considering first the magnetostriction for fields applied along [110] and dilation along [110], the lattice contracts as fields sweep through the singlet/triplet regime (Fig. 5.9 a)). At 1.05 K, above the ordered states, the magnetostriction continuously

decreases. At lower temperatures, the lattice shows an equivalent overall contraction as fields increase, but there is an additional sharp contraction in the magnetostriction at the transition into the ordered state and a sharp increase at the transition out of the ordered state, superimposed on top. Overall the lattice contracts by roughly 0.045% by 30 T. The field derivative of the magnetostriction for this orientation reveals peaks associated with transitions into both ordered states (Fig. 5.9 (b)). At 0.79 K only one peak is observed on entering the ordered states, likely due to broadening of the transition, while at 0.35 K two separate peaks are observed.

The magnetostriction for fields along [100] and dilation along [110] (dilation perpendicular to field, both in plane) are shown in Fig. 5.9 (c). The magnetostriction decreases at fields above H_{c1}, continues to decrease until roughly the midpoint of the singlet-triplet regime, and then increases less rapidly until H_{c2}, contracting the lattice 0.005% at H_{c2} relative to H_{c1}. At lower temperatures the onset of the contraction and the termination of the expansion become sharper. The field derivative of the magnetostriction for this orientation shows peaks associated with onset (termination) of the lattice contraction (expansion) (Fig. 5.9 (d)). Similar to the first field/dilation arrangement considered, two (one) peaks are observed at base (intermediate) temperature.

The magnetostriction of the final experimental setup, with fields applied along [100] and dilation along [001], is plotted in Figure 5.9(e). The lattice begins to expand from fields above H_{c1} until roughly the midpoint of the singlet-triplet regime, and then begins to contract less rapidly until H_{c2}, leaving the lattice 0.025% expanded relative to the beginning of the singlet/triplet regime. At lower temperatures the onset of the increase and the end of the decrease becomes sharper. Finally, identically to the other two directions, there are peaks in the field derivative of the magnetostriction at the phase transitions (Fig. 5.9(f)).

Magnetostrictions for the three different dilation directions, and their first derivatives with respect to field, are plotted together at base temperature in Fig. 5.10(a) and (b), respectively. The three curves do not add to zero at extended fields. This could be due to the nonconservation of volume as the field is swept, however it is more likely due to the lack of a background subtraction associated with the empty

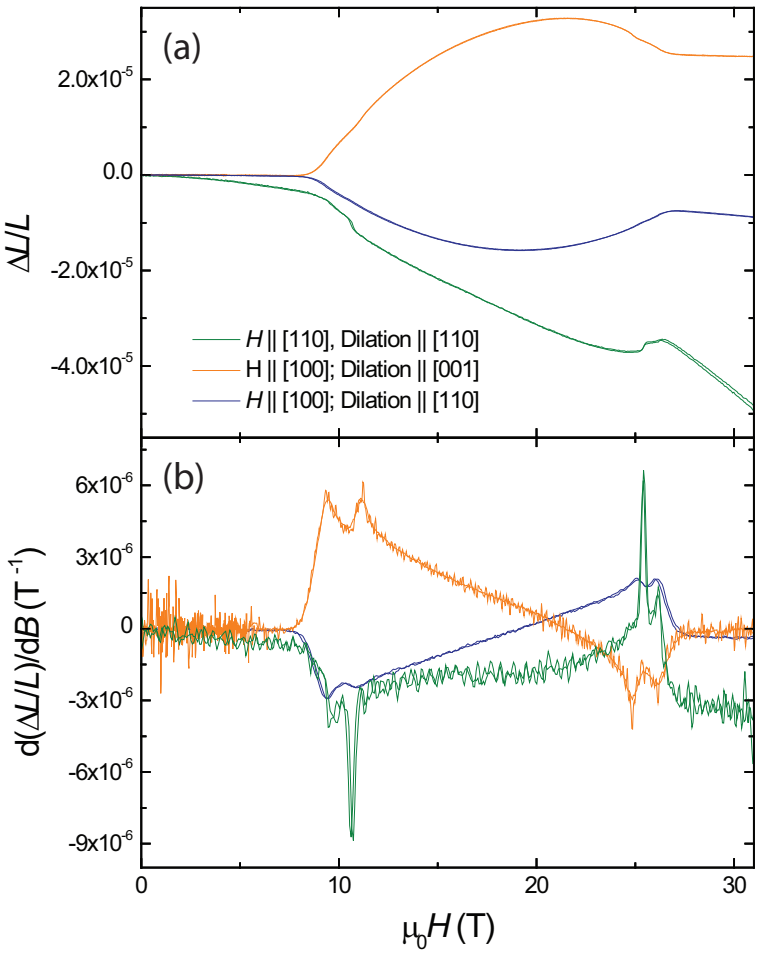

Figure 5.10: Comparison of the linear coefficient of magnetostriction (a) and its first derivative with respect to field (b) at 0.35 K for the three orientations measured.

dilatometer. The primary effect is the lattice expansion along the [001] direction connected by the J_0 bond the strongest antiferromagnetic coupling. By expanding along this strongest exchange, the exchange penalty from the condensed triplets can be reduced. The lattice contraction near the middle of the singlet-triplet regime presumably reflects particle-hole symmetry, such that the singlet sites prefer to contract. The other two lattice directions compensate for the expansion along [001] by contracting, although because of the lack of background subtraction it is unclear how perfectly the two directions compensate for the [001] direction.

5.1.3 Torque

Extensive torque magnetization experiments were performed at the NHMFL on a single crystal of $Ba_3Mn_2O_8$ for fields up to 15 T and temperatures between 25 mK and 800 mK. Several different measurements were run: the temperature dependence of the phase boundary for fields near perpendicular to the c axis; the temperature dependence of the phase boundary for fields near the c axis; and also the angular dependence of the phase boundary at 25 mK as fields were rotated from close to the c axis to nearly perpendicular to the c axis.

Determination of the phase transition from the torque data requires detailed studying of the data and its field derivatives. Although the torque τ is the quantity actually measured data is usually analyzed as τ/H because that quantity is roughly equivalent to the magnetization and under certain circumstances exact (Eq. 4.7). The magnetization is proportional to the first derivative of the free energy with respect to field, implying that a second order phase transition would exhibit a delta-like peak in the second field derivative of the magnetization, as has been observed in $BaCuSi_2O_6$ [47]. However there are peaks (and sharp troughs) in the first derivative of τ/H at all temperatures for the transition between phase I and phase II and at temperatures above $\sim$ 150 mK for the transition between the paramagnetic phase and phase II. Transitions marked by these peaks and troughs in the first derivative are likely first order, although it could also be evidence of a change in the anisotropy of the system. There is a further complication to determining the phase boundary: the peaks in the

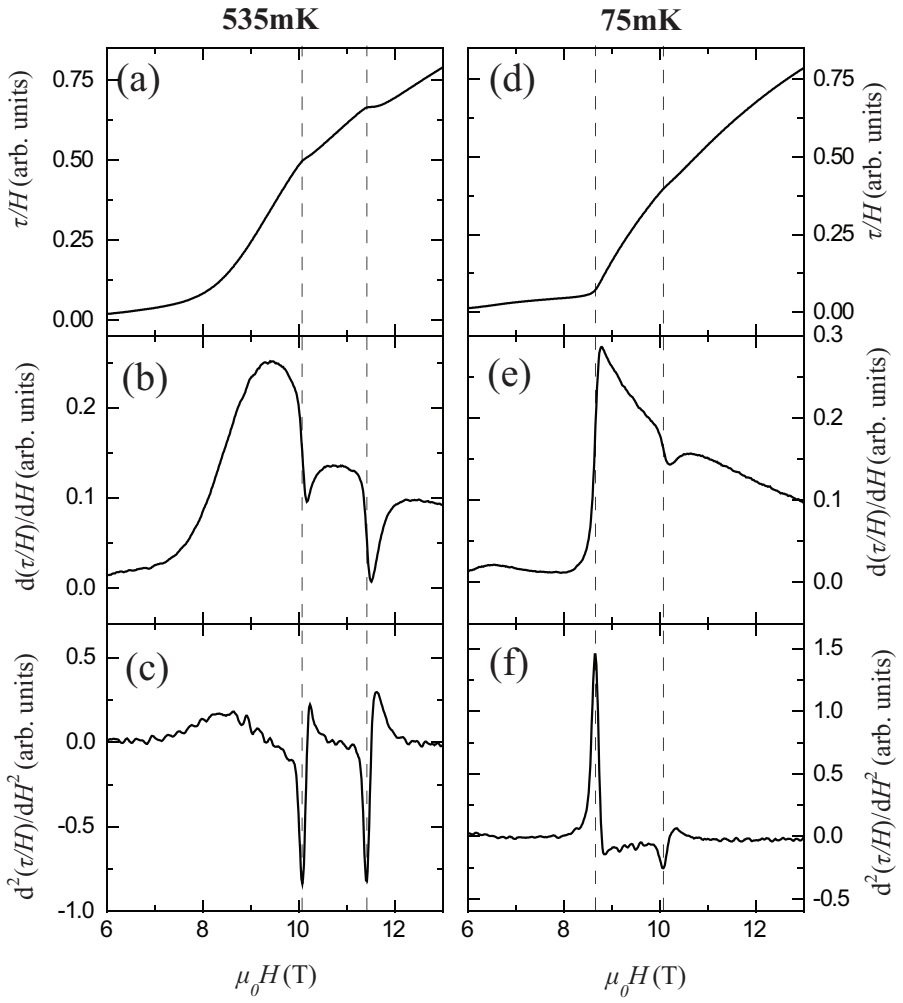

Figure 5.11: Torque scaled by field and its first two derivative versus field for fields applied close to perpendicular to the c axis.

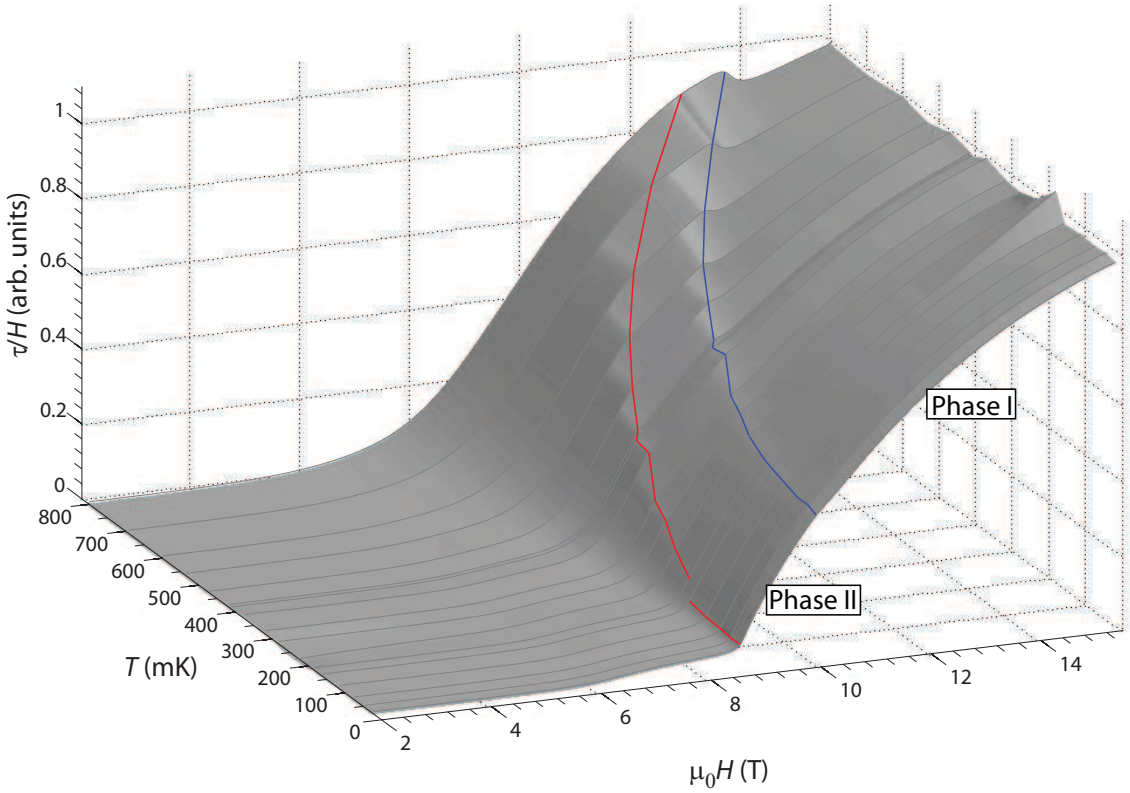

Figure 5.12: Torque scaled by field data versus temperature and field for fields applied close to perpendicular to the c axis. Red and blue lines mark the difference between the disordered phase and phase II and between phase II and phase I, respectively.

first derivative (and by extension second derivative) change signs from sharp peak to sharp trough and vice versa for successive field sweeps as either the temperature or angle is tuned. To systematically account for this variance a uniform method of phenomenologically determining the phase transition was devised: a peak or trough in the *second* field derivative of τ/H that most closely lined up with the change in τ/H was chosen as the phase transition. A few representative τ/H curves, and their first and second field derivatives, taken at several different temperatures are shown in Fig. 5.11 and illustrate how the phase transitions are ascribed to different features in the second derivative.

Raw data taken to the highest temperatures measured for fields nearly perpendicular to the c-axis, scaled by the magnetic field strength, are shown as a 3D surface in

Fig. 5.12. The sharp increase in torque at 8.5 T for the lowest temperatures corresponds to the spin gap closing as the minimum of the the S_z=1 triplet band crosses the singlet leading to a finite magnetization. As temperature is increased, thermal effects smear out this rapid increase in torque, and field derivatives of τ/H at H_{c1} rapidly broaden with temperature (Fig. 5.13(a) and (b)). Superimposed on top of the broad rise in torque with field, the two phase transitions seen in heat capacity and MCE experiments are clearly visible as breaks in the slope of τ/H (Fig. 5.12).

Fig. 5.13 (a) and (b) shows 3D surface plots of the first and second field derivatives of τ/H respectively for fields applied nearly perpendicular to the c axis for all temperatures measured. These curves demonstrate the smooth evolution of the various features described above. Points on the resulting phase diagram, extracted as described above are shown in Fig. 5.13(c) and are in agreement with points taken from MCE and C_p measurements up to the inherent angular misalignment in this torque measurement. No boundary points are plotted in the temperature region where there is a crossover from second order behavior to first order behavior leading to ambiguity in the choice of feature marking the phase transition.

Extensive measurements were attempted to determine the critical scaling behavior of the transitions for fields both nearly aligned with the c axis and nearly perpendicular to the c axis. However, because the scaling behavior can only be fit in the range where the transition is second order there were not enough data points in the available temperature range to get reliable estimates of the scaling parameters.

Measurements were also undertaken on the angular dependence of the torque magnetometry at 25 mK. The measurement was intended to probe the angular dependence in the a-c plane, however the sample was slightly inclined such that the field did not exactly rotate within the [100]-[001] plane, generating a finite torque for all angles studied. Angles are quoted in terms of the angular position with respect to the closest approach to the c axis, but it is important to note that the field was never less than $\sim 10^\circ$ from the c axis. Consequently two phase transitions are observed for all angles studied. The sign of the peak in the second derivative marking the transitions between the paramagnetic phase and phase II (H_{c1}) and between phase II and phase I (H_{II-I}) both changed with the evolution of angle, reflecting a change in anisotropy

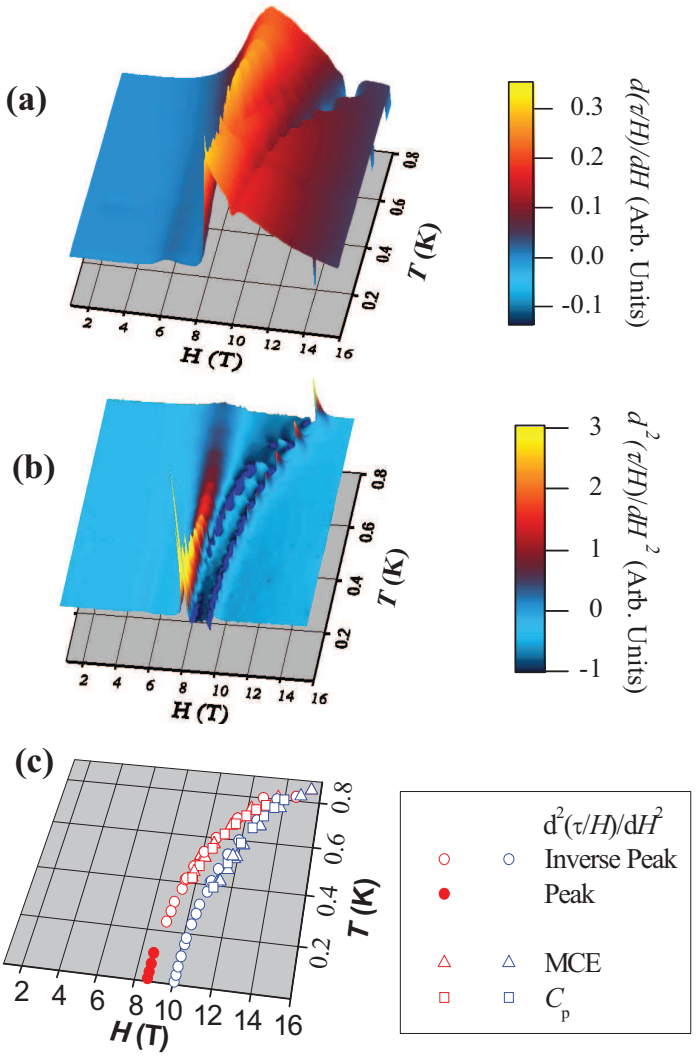

Figure 5.13: (a) First and (b) second derivatives with respect to field of torque divided by field for fields close to perpendicular to the c axis. (c) Phase boundary derived from torque as described in main text.

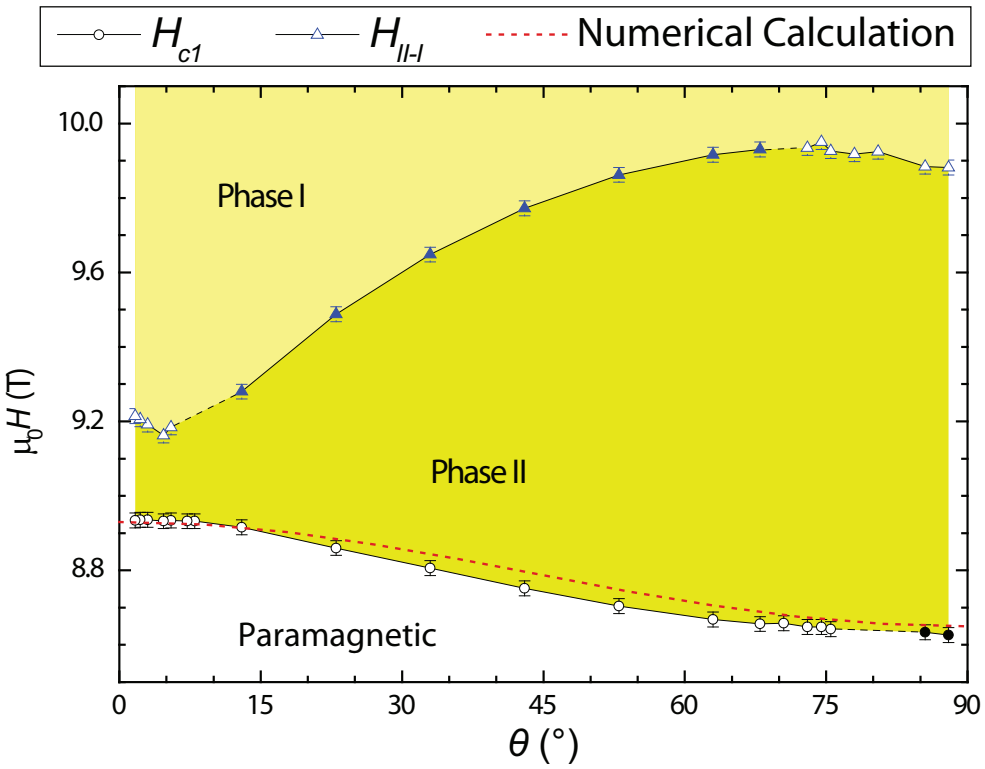

Figure 5.14: Phase diagram at 25 mK determined from torque magnetometry measurements. Circles (triangles) mark transitions between the disordered phase and phase II (phase II and phase I). Open (closed) symbols signify that the transition was determined from a peak (trough) in the second derivative. Angles are measured relative to the closest approach to the c axis as described in the main text.

for the two different phases. This lead to minor discontinuities in the determination of the phase boundary (dashed lines in Fig. 5.14).

Similar to the phase diagram obtained from heat capacity measurements (Fig. 5.8), the phase diagram obtained from torque measurements at lowest temperatures reveals a non-monotonic angle dependence (Fig. 5.14). The maximum value of H_{II-I} occurs between 65-75° from the closest approach to the c axis. This is in agreement with the heat capacity data, for which the smallest T_{c_I} occurs at 75° from the c axis. Additionally, the field extent of phase II, $\Delta_H = H_{II-I} - H_{c1}$, is largest at 75°, and decreases by ∼0.05 T from its maximum value at the highest angles measured.

5.2 Critical Field

Through consideration of the minimal spin Hamiltonian (Eq. 2.4) it is possible to calculate the critical field $H_{c1}(\theta)$ corresponding to the value for which the energy of lowest energy triplet mode becomes equal to zero. The calculation, performed by K. A. Al-Hassanieh and C. D. Batista, is based on a generalized spin-wave approach in which only the singlet and the three triplet states of each dimer are kept [48]. The softening of this triplet mode signals the onset of the magnetic instability towards an ordered state (phase I for $H \| c$ and phase II otherwise). For field directions along the principal axes, it is possible to obtain simple analytical expressions for the critical field [49]. The expression for $H \| c$ is:

$$(g_{cc}\mu_B H_{c1})^2 = \left(J_0 - \frac{D}{3}\right)^2 + \frac{8}{3}\left(J_0 - \frac{D}{3}\right)\mathcal{J}_{min}, \tag{5.3}$$

while for $H \perp c$ the expression is:

$$\begin{aligned}(g_{aa}\mu_B H_{c1})^2 &= \left(J_0 + \frac{D}{6}\right)^2 + \frac{8}{3}\left(J_0 + \frac{D}{6}\right)\mathcal{J}_{min} \\ &\quad -\frac{D^2}{4} - \frac{4}{3}|D||\mathcal{J}_{min}|\end{aligned} \tag{5.4}$$

where $\mathcal{J}_{min}$ is the minimum of the interdimer exchange portion of the dispersion (Eq. A.7) which is fully described in Appendix A. The difference in the first two terms between these expressions stems from a change in the zero field splitting of an isolated dimer depending on quantization direction expressed in the reduced basis of dimer states as described in section B.1 of Appendix B. The two additional terms of H_{c1} for fields perpendicular to the c axis arise from the second order process mixing singlets and triplets as described in section 2.3 of the Theory chapter. This state mixing causes the gap between the $S^z = 1$ triplet and singlet states to close as $\sqrt{H - H_{c1}}$, as expected for an Ising-like QCP. Evaluating these expressions using the values of the exchanges and single ion anisotropy yield values for the critical fields which are in good accord with the measured data. Numerical calculation of H_{c1} for arbitrary field orientations in the [001]-[100] plane yields the red dotted curve shown

in Fig. 5.14. The calculation was performed using the values of D and the interdimer couplings given in the introduction while J_0 was allowed to vary leading to a fit value of 1.567 meV. The calculated values agree well with the measured data up to the inherent uncertainty associated with the misalignment of the sample in the torque measurements described above.

5.3 Ordered States

A few direct measurements have been undertaken to determine the microscopic nature of the singlet-triplet ordered states of $Ba_3Mn_2O_8$. Nuclear magnetic resonance (NMR) studies at high fields revealed a continuously varying local magnetization for the Ba site, indicative of incommensurate order [33]. In addition, elastic neutron studies performed for fields perpendicular to the c axis in the ordered states also revealed incommensurate order, with ordering wavevectors aligned slightly away from $(\frac{1}{3}, \frac{1}{3})$ [50]. However, due to the incommensurate nature of the ordered states neither measurement could provide a full microscopic description of the ordered states. In the absence of such a determination of the ordered states analysis of the spin Hamiltonian can provide candidates for the microscopic ordering present. In this section I will motivate and describe the classical ordered states that were found from the effective psuedospin Hamiltonian in the singlet-triplet regime, Eq. 2.31.

To understand the origin of the specific structures proposed, it is simplest to first consider the limiting cases - fields applied parallel and perpendicular to the c-axis. In each case I first consider the 2D lattice, effectively setting J_1 and $J_4 = 0$ (i.e. no interplane coupling), before considering the full 3D case. After these simple cases I finally consider the general case of intermediate fields.

5.3.1 Field Parallel to c

Considering first the 2D lattice (effectively setting J_1 and $J_4 = 0$), and noting that the D anisotropy does not act on the s^{xy} components of the pseudospins (i.e. both $a(\theta = 0) = 0$ and $\tilde{\mathbf{D}}_l(\theta = 0) = 0$), the system consists of independent triangular

layers of vertical dimers, and the effective Hamiltonian reduces to

$$\begin{aligned}\tilde{\mathcal{H}} &= \sum_{l\langle i,j\rangle}\left[\frac{J_2+J_3}{2}\tilde{s}^z_{il}\tilde{s}^z_{jl}+\frac{8\left(J_2-J_3\right)}{3}\left(\tilde{s}^x_{il}\tilde{s}^x_{jl}+\tilde{s}^y_{il}\tilde{s}^y_{jl}\right)\right] \\ &- \left(g_{cc}\mu_B H-J_0-3\left(J_2+J_3\right)/2+D/3\right)\sum_{l,i}\tilde{s}^z_{il} \qquad (5.5)\end{aligned}$$

The effective exchange anisotropy is easy-plane, i.e., the XY component of the effective exchange dominates. At $T=0$, the triplets condense (canted XY antiferromagnetic ordering) for $H > H_{c1} = \left(J_0 - 4\left(J_2-J_3\right)\right)/\left(g_{cc}\mu_B\right)$ into a state that can be approximated by a direct product of single dimer states of the form:

$$|\psi_{il}\rangle = \cos\theta_{il}|00\rangle + \sin\theta_{il}e^{-i\phi_{il}}|11\rangle. \qquad (5.6)$$

The canting angle $\theta_{il} = \theta$ is uniform and is set by the magnetic field, while $\phi_{il} = \phi_l + \mathbf{Q}\cdot\mathbf{r}_i$ with $\mathbf{Q} = (\pm\frac{1}{3},\pm\frac{1}{3})a^*$. The relative phase between different layers is determined by ϕ_l, which can take any value for the moment because we are assuming that $J_1 = 0$. The expectation values of the pseudospins take a simple form

$$\begin{aligned}\langle\psi_{il}|\tilde{s}_x|\psi_{il}\rangle &= \frac{1}{2}\sin 2\theta\cos\left(\mathbf{Q}\cdot\mathbf{r_i}+\phi_l\right) \\ \langle\psi_{il}|\tilde{s}_y|\psi_{il}\rangle &= \frac{1}{2}\sin 2\theta\sin\left(\mathbf{Q}\cdot\mathbf{r_i}+\phi_l\right) \\ \langle\psi_{il}|\tilde{s}_z|\psi_{il}\rangle &= -\frac{1}{2}\cos 2\theta. \qquad (5.7)\end{aligned}$$

This corresponds to a canted antiferromagnetic state, in which the $\tilde{s}^{xy}$ component of the pseudospins orient 120° with respect to each other to minimize the interdimer exchange energy (i.e. the $\tilde{s}^{xy}$ components of the pseudospins on each triangular plaquet sum to zero) analogous to the classical solution for a Heisenberg or XY antiferromagnet on a triangular lattice [18]. This is illustrated in Fig. 5.15(a). The phase, corresponding to the angle of the $\tilde{s}^{xy}$ component of the pseudospins relative to the crystal lattice, spontaneously breaks the U(1) symmetry of the effective Hamiltonian, and the ordered state can be described as a Bose-Einstein condensate. In terms of the original spins on each Mn site, the ordered state still consists of a canted AF with

the S^{xy} component of the spins on adjacent dimers oriented 120° with respect to each other, but with these components reversed for spins on the top and bottom of each dimer unit. The S^z component of each spin is equivalent for each Mn ion.

Now consider the full 3D lattice with nonzero J_1 and J_4. The Hamiltonian still maintains U(1) symmetry, and the ordered state will still correspond to a triplet condensate (consistent with the lambda anomaly observed in heat capacity measurements for this field orientation) because the XY interaction in the Hamiltonian dominates the Ising interaction. However, the system now has the possibility to gain additional energy from the interlayer exchange. The $\tilde{s}^{xy}$ component of the total spin on any triangular plaquette for the classical case in Fig. 5.15(a) is zero, but if the pseudospins twist around the z-axis to form a spiral structure in which successive spins along the [100] and [010] directions rotate by an angle $\alpha = 120° \pm \epsilon$ in the XY plane, the system is then able to benefit from the interlayer coupling. There are two degenerate solutions that minimize the total energy. The first solution is characterized by a uniform phase along the c-axis: $\phi_l = 0$. In contrast, the phase is staggered $\phi_l = l\pi$, in the second solution. In addition, the shift of the single-layer ordering wave-vector from $\mathbf{Q} = (\pm\frac{1}{3}, \pm\frac{1}{3})a^*$ to $\mathbf{Q} = \pm(\alpha, \alpha)\frac{2}{\sqrt{3}a}$ (note that $a^* = \frac{4\pi}{\sqrt{3}a}$ in this non-orthogonal basis) has opposite signs for the two cases:

$$\begin{aligned} \cos\alpha &= -\frac{1}{2} - \frac{J_1}{4\left(J_2 - J_3 - J_4\right)} \quad \text{for} \quad \phi_l = 0 \\ \cos\alpha &= -\frac{1}{2} + \frac{J_1}{4\left(J_2 - J_3 - J_4\right)} \quad \text{for} \quad \phi_l = l\pi, \end{aligned} \tag{5.8}$$

corresponding to angles $\alpha = 124°$ and $\alpha = 116°$ respectively for the values of J_1, J_4 and $(J_2 - J_3)$ obtained from single crystal INS [26, 27, 28]. The gain in energy of this in-plane twisting due to the interlayer interactions scales linearly with ϵ (i.e. for a given phase relation between adjacent layers there is a "right way" and a "wrong way" to twist the spiral structure). In contrast, the loss in intralayer energy from breaking the perfect 120° structure scales quadratically with ϵ because $\alpha = 120°$ is the minimum energy structure for J_1 and $J_4 = 0$. Hence, an arbitrarily small interlayer exchange is able to stabilize a spiral phase as indicated by Eq. 5.8. The resulting

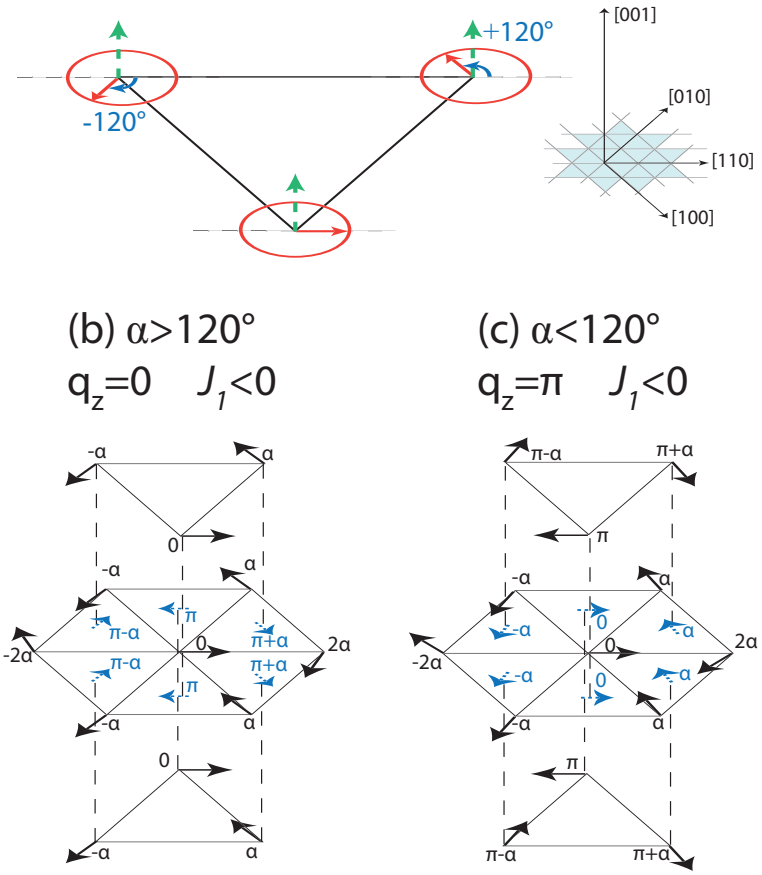

Figure 5.15: Schematic diagrams of the predicted spin structure for field applied along c-axis. (a) 120° structure on a triangular plaquette corresponding to the classical solution for Heisenberg spins on a 2D lattice. Dashed green and solid red arrows indicate $\tilde{s}^z$ and $\tilde{s}^{xy}$ components of the pseudospin representing each dimer unit, respectively. Inset shows crystal axes. Full 3D structure of $\tilde{s}^{xy}$ components of pseudospins on successive layers for values of α more than and less than 120° leading to ordering wavevectors along the z-direction of 0 and $\frac{1}{2}c^*$ are plotted in (b) and (c) respectively. Dashed blue arrows indicate the total pseudospin moment on each triangular plaquette, illustrating antiferromagnetic interplane coupling.

phase is incommensurate, in agreement with the previously described NMR [33] and elastic neutron scattering measurements at high fields [50].

A similar structure, but with antiferromagnetic interplane coupling, has already been proposed by Uchida *et al.* following their initial estimation of the exchange constants in $Ba_3Mn_2O_8$ [24]. However, two subtleties to the ordered phase were not anticipated in that earlier paper. The first of these is that ϵ can take both positive and negative values because there are two degenerate solutions: $\phi_l = 0$ or $\phi_l = l\pi$. If $\alpha > 120°$, as illustrated in Fig. 5.15(b), then for $J_1 > 0$ the component of the ordering wavevector along the c direction, q_z, is equal to 0 ($\phi_l = 0$). However, if $\alpha < 120°$, as illustrated in Fig. 5.15(c), then the component of the ordering wavevector along the c direction, q_z, is equal to $\frac{1}{2}c^*$ ($\phi_l = l\pi$), leading to a doubling of the unit cell along the c-axis. A second subtlety of the ordered phase is that the resulting structure contains triangular plaquettes on which pair of spins are more closely antiferromagnetically aligned along specific directions, while other pairs of spins are less perfectly antiferromagnetically aligned along equivalent crystallographic directions. Specifically, adjacent spins along the [110] direction have a relative angle of $2\alpha = 2(120° + \epsilon) \equiv 120° - 2\epsilon$, in contrast to adjacent spins along the [100] and [010] directions which have a relative angle of $\alpha = 120° + \epsilon$. While such "bond order" would lead to a subtle lattice deformation, this effect was not found in the magnetostriction. However, such a subtle effect would likely be obscured by the much stronger effect of the intradimer coupling which dominated the overall behavior of the magnetostriction.

5.3.2 Field Perpendicular to c

For fields oriented away form the c axis, the anisotropy term D breaks the U(1) symmetry of the Hamiltonian; in particular for fields applied perpendicular to the c axis the dominant anisotropy term $a(\theta = \pi/2) = \frac{-2D}{J_0}$ is nonzero (the smaller intermediate angle term $\tilde{\mathbf{D}}(\theta = 0) = 0$ is still zero). The anisotropy term induces an easy axis in the ordering plane which can stabilize an Ising-like modulated structure. To understand the nature of this phase, it is instructive to first consider the case in which D vanishes on a 2D lattice (J_1 and $J_4 = 0$) and a magnetic field is applied perpendicular

to the crystalline c axis, for instance along the direction midway between [100] and [110] (i.e. along the "point" of a triangular plaquette). All of the same arguments given above for the case $H\|c$ and $J_1, J_4 = 0$ still apply, but the quantization axis now lies in the ab plane so the XY order lies in the plane defined by the two vectors [001] and [010] (Fig. 5.16(a)). Since $D = 0$, there is no anisotropy in this plane, and the pseudospins spontaneously break U(1) symmetry – the ordered state is a Bose Einstein condensate. However, a finite value of D in equation 2.31 qualitatively changes the nature of the ground state. For the specific example of the field oriented along the tip of the triangular plaquette, a negative value for D, appropriate for $Ba_3Mn_2O_8$, implies an easy axis for the $\tilde{s}^{xy}$ component of the the pseudospins along the [001] direction. For the 2D lattice (i.e. $J_1, J_4 = 0$), the in-plane interaction between spins still favors a magnetic structure for which the total spin in the XY plane vanishes. To minimize both the anisotropy energy and also the in-plane exchange energy, the system may adopt an inhomogeneous magnetic structure in which the component of the pseudospins along the hard axis are depressed relative to along the easy axis while the canting angle along the z-axis is adjusted so as to preserve zero net $\tilde{s}^{xy}$ spin on each triangular plaquette (fig. 5.16(b)).

Considering now the 3D lattice (finite J_1 and J_4), the general form of the pseudospins describing this modulated behavior in a spin dimer system with uniaxial anisotropy is

$$\begin{aligned}
\langle\psi_{il}|\tilde{s}_x|\psi_{il}\rangle &= \frac{1}{2}\sin 2\theta \cos\left(\mathbf{Q}\cdot\mathbf{r_i}+\phi_l\right) \\
\langle\psi_{il}|\tilde{s}_y|\psi_{il}\rangle &= \frac{1}{2}\cos\gamma \sin 2\theta \sin\left(\mathbf{Q}\cdot\mathbf{r_i}+\phi_l\right) \\
\langle\psi_{il}|\tilde{s}_z|\psi_{il}\rangle &= \frac{\pm 1}{2}\sqrt{\cos^2 2\theta + \sin^2 2\theta \sin^2\gamma \sin^2\left(\mathbf{Q}\cdot\mathbf{r_i}+\phi_l\right)},
\end{aligned} \tag{5.9}$$

where $0 \leq \gamma \leq \pi/2$ sets the ratio between the maximum amplitude of the $\tilde{s}^y$ and $\tilde{s}^x$ components and consequently the amplitude of the modulation of the $\tilde{s}^z$ component ($\gamma = 0$ is unmodulated and $\gamma = \pi/2$ is maximally modulated). The positive (negative) sign in the last line of Eq. 5.9 holds for $\theta > \pi/4$ ($\theta < \pi/4$). Minimization of the

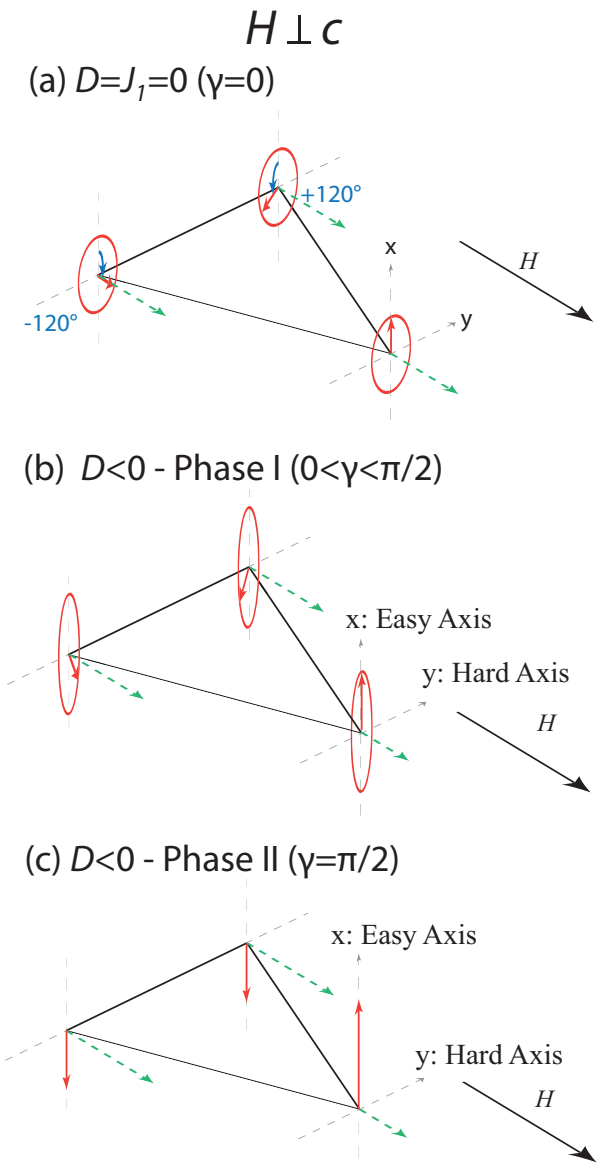

Figure 5.16: Schematic diagram showing spin structure for fields pointing along the 'point' of a triangular plaquette obtained by minimizing parameters in Eq. 5.9. Dashed green and solid red arrows indicate $\tilde{s}^z$ and $\tilde{s}^{xy}$ components of the pseudospin representing each dimer unit, respectively. (a) Spin structure for D=0 and J_1=0 for $H\|[110]$. The $\tilde{s}^{xy}$ components of the pseudospins are oriented 120° from each other, equivalent to the case shown in figure 5.15(a) for $H\|c$, but rotated into the [010]-[001] plane. (b) Partially modulated phase (phase I) for $D < 0$ and J_1 finite. The $\tilde{s}^{xy}$ components of the spin precess along an elliptical path with an incommensurate wavevector close to $(\frac{1}{3}, \frac{1}{3})a^*$. (c) Maximally modulated phase (phase II) stabilized close to H_{c1} and H_{c2}.

Hamiltonian (Eq. 2.31) with respect to the different parameters θ, γ, $\mathbf{Q}$ and ϕ_l yields the ground state. The optimal values of $\mathbf{Q}$ and ϕ_l are still very well approximated by Eq. 5.8. The optimal values of θ and γ as a function of the field H are shown in Fig. 5.17. The ordered ground state has no $\tilde{s}^y$ component of the pseudospin ($\gamma = \pi/2$) for H near H_{c1} (Fig. 5.16(c)). However the effective exchange anisotropy $\frac{J_2+J_3}{2}\tilde{s}^z_{il}\tilde{s}^z_{jl}$ in $\tilde{\mathcal{H}}_{st}$ (Eq. 2.31) penalizes the modulation of the $\tilde{s}^z$ component and favors a less modulated structure ($\gamma < \pi/2$) when the z-component of the real magnetization becomes large enough, i.e., when $H - H_{c1}$ is large enough. This is presumably the origin of the two distinct phases observed in thermodynamic measurements for fields oriented perpendicular to the c-axis. The reemergence of phase II close to the top of the singlet-triplet regime is a consequence of the particle-hole symmetric nature of this Hamilton where at fields near H_{c2} the small singlet density minimizes the effective exchange anisotropy penalty. A full analysis performed by K. A. Al-Hassanieh and C. D. Batista including all three triplet states quantitatively accounts for H_{c1} [48], however even without including these terms the agreement with the measured phase diagram is remarkable. According to the results shown in Fig. 5.17, the transition between both phases is of second order at $T = 0$. For H slightly larger than H_{II-I} (the critical field for the transition between phase II and phase I) the field dependence $\pi/2 - \gamma \propto \sqrt{H_{II-I}}$ is characteristic of a mean field transition. Correspondingly, the total magnetization and θ exhibit a kink at $H_{1,2}$. The resulting structure stable at higher fields is still modulated along the z direction but with a finite component along the y direction (Fig. 5.16(b)). The $\tilde{s}^y$ component of the pseudospin varies to the $\tilde{s}^x$ component as a function of field, yielding an unmodulated structure exactly at the middle of the dome since $\tilde{s}^z$=0 at this field, equivalent to the $H\|c$ structure. At this field, rotation of field into the $H\|c$ direction therefore occurs without crossing a phase boundary, consistent with our labeling of phase I in Fig. 5.6(a) and (b). The energy associated with the anisotropy $a(x)\,(J_2 - J_3) \sim D\,(J_2 - J_3)\,/J_0$ ~25 mK is small, consistent with the observation of a λ-like anomaly in heat capacity seen in Fig. 5.1(b) (i.e the critical scaling associated with the Ising phase transition will only apparent very close to T_c).

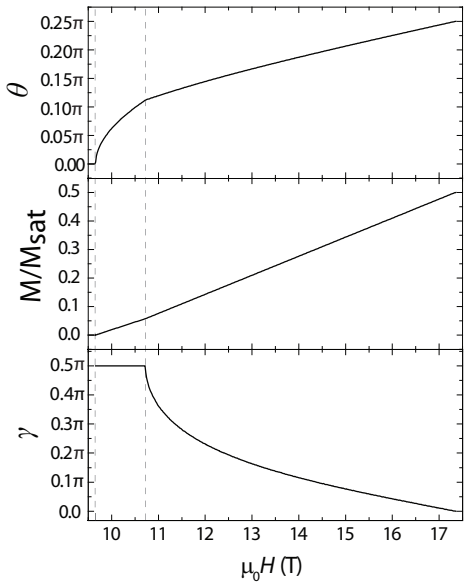

Figure 5.17: Variational parameters γ and θ and normalized magnetization M/M_{sat} that result from minimizing the energy ($\tilde{\mathcal{H}}$) for the spin configuration described by Eq. (5.9). The vertical dashed lines mark H_{c1} and the transition between phase II and phase I. Fit values of $J_0 = 19.1$ K, $J_1 = -1.37$ K and $J_2 - J_3 = 1.32$ K determined from preliminary fits of triplet dispersion measured at $H = 0$ in a single crystal of $Ba_3Mn_2O_8$ [27, 28]. The value of $J_3 = 1.27$ K was chosen to fit the measured optimal field: $(H_{c1} + H_{c2})/2 \sim 17.3$ T. The disagreement between the calculated $H_{c1} \sim 9.6$ T and the measured value of ~ 8.7 T is due to our two-level (singlet-triplet) approximation. Good quantitative agreement is obtained if the other two triplets are included.

The resulting modulated structures are characterized by three separate order parameters: there is a finite modulation of the magnetization along the field direction (Ising order), there is also Ising ordering along the easy direction perpendicular to the field, and finally there is bond order. Referring back to the heat capacity data (Fig. 5.1), the anomaly associated with this phase transition into phase II is clearly different to the λ anomaly seen for fields oriented parallel to the c-axis, although the data do not permit a critical scaling analysis. Estimates of the change in entropy through the transition into phase II vary only weakly with field or temperature, possibly implying a significant lattice contribution.

5.3.3 Field at Intermediate Angles

At intermediate angles is is expected the width of phase II should primarily vary in proportion to the strength of $a(\theta) = \sin^2(\theta)a(\pi/2)$, implying monotonic evolution with field. However, both the torque data (Fig. 5.14) and heat capacity data (Fig. 5.8) had the maximal width of phase II for fields $\sim 75^\circ$ from the c axis. This discrepancy may be caused by the additional effective Dzyaloshinskii-Moriya term arising from the zero field splitting term present at intermediate fields, $\tilde{\mathbf{D}}(\theta) = -\sin(\theta)\cos(\theta)\frac{D}{4\sqrt{3}J_0}\hat{\mathbf{y}}$, which is only nonzero for intermediate fields.

This effective DM interaction between dimers on adjacent layers is frustrated in both ordered states at a mean field level (the mean value of $J_1 \sum_{l\langle\langle i\rightarrow j\rangle\rangle} \tilde{\mathbf{D}}(\theta) \cdot \tilde{\mathbf{s}}_i \times \tilde{\mathbf{s}}_j + J_4 \sum_{l\langle\langle i\rightarrow j\rangle\rangle'} \tilde{\mathbf{D}}(\theta) \cdot \tilde{\mathbf{s}}_i \times \tilde{\mathbf{s}}_j$ is zero for both phase I and phase II). Therefore, the small contribution of the effective DM interaction to the ground state energy must be produced by quantum fluctuations. Because the DM vectors point along the $\hat{y}$ direction (perpendicular to the applied field and to the easy c axis) this contribution term will favor phase II, for which the pseudo-spins only have x and z components (Fig. 5.18(b)(ii)), as opposed to phase I for which the pseudo-spins have an additional third component along the y direction (Fig. 5.18(b)(i)). Thus this contribution strengthens phase II relative to phase I near $\theta = \pi/2$ and leads to a small non-monotonic behavior of the H_{II-I} curve (see Fig. 5.14).

Although this simple analysis captures the qualitative non-monotonic behavior of

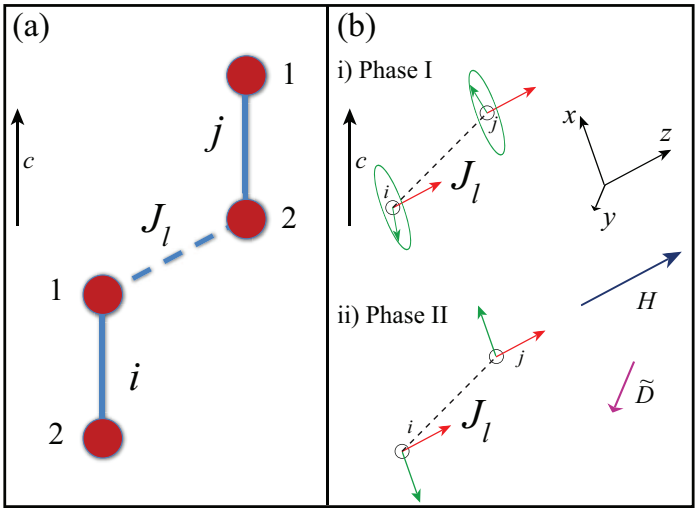

Figure 5.18: (i), (ii) Schematic diagram for two pseudo-spins on adjacent dimers connected by the J_l interaction for arbitrary field direction in the a-c plane. Red arrows show uniform moment, while green arrows show ordered moment. Field direction along z axis, $\tilde{\mathbf{D}}$ along $\hat{y}$ axis, and c axis vertical.

the H_{II-I} curve, it cannot account for the magnitude of the observed effect. The amplitude of the effective DM interaction is of order 100 mK for $\theta \simeq 75°$. Because the interaction mixes the singlet and $S^z = 1$ triplet dimer states, the mean value of the DM term is less than $\sqrt{m}\mathcal{D}(\theta)$ for any state with magnetization m (the mean density of $S^z = 1$ triplets). Noting that $m \simeq 0.06$ at H_{II-I}, the upper bound on the DM term of $\simeq 25$ mK is the order of magnitude of the observed non-monotonic effect of 5-10 mK in the H_{II-I} curve. Given that $\mathcal{D}(\theta)$ is much weaker than the dominant terms of $\mathcal{H}_{st}$, it is clear that the effective DM term can only explain the magnitude of the non-monotonic effect if it gives a first order contribution to the energy of phase II. However, as established above for the both phase I and phase II, the effective DM interaction contributes via a second order correction and must therefore be considerably smaller. This leaves us with two possibilities: a) The magnetic structure of phase II is different from the simple Ising phase in such a way that the mean value of the effective DM term is non-zero, or b) The non-monotonic effect is caused by a term that has not been included in $\mathcal{H}_{st}$. Currently it is impossible to distinguish between these possibilities, but ongoing efforts to experimentally determine the magnetic structure

have the potential to directly address option (a), while EPR experiments should, at least in principle, be able to determine the energy scale of additional interactions not considered in the minimal spin Hamiltonian (Eq. (2.4)).

Chapter 6

Triplet-Quintuplet Regime

The vast majority of previously studied spin dimer compounds are based on pairs of $S = \frac{1}{2}$ spins. A pair of spin $S = \frac{1}{2}$ ions can have total spin 0 or 1; interactions between pairs of spins in a spin dimer system leads to the previously discussed singlet-triplet ordered states. However, if the dimers are based on a pair of larger spin $S = 1$ ions, then the dimer can have total spin 0, 1 or 2, such that interactions between dimers can lead to similar triplet-quintuplet ordered states at higher fields than the singlet-triplet ordered states. Only one previous $S = 1$ spin dimer has been studied, the organic biradical magnet F2PNNNO [21, 22]. In this chapter, I will present the first direct measurements of a triplet-quintuplet ordered state in a spin dimer system, then compare and contrast the triplet-quintuplet ordered states to the singlet-triplet ordered states before finally discussing the fluctuation induced asymmetry at highest fields. This work has been published in ref. [30]

6.1 Experimental Results

Fields above 35 T are required to access the triplet-quintuplet ordered state, constraining the magnets and techniques available to study this regime. Of these limited choices, magnetization measurements in pulsed fields and heat capacity and magnetocaloric effect measurements in the hybrid magnet were performed in this regime.

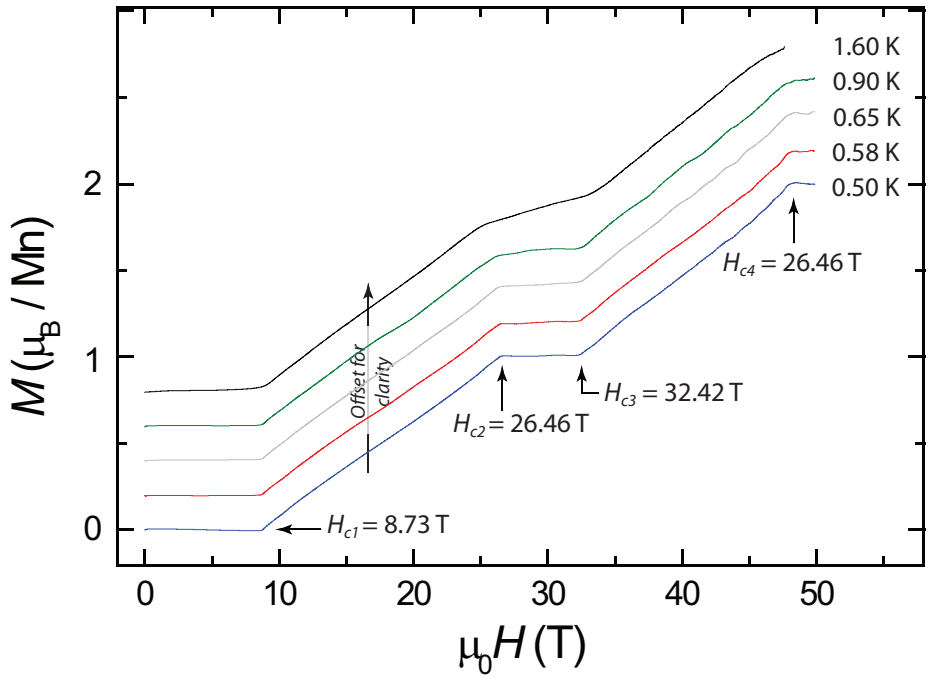

Figure 6.1: Magnetization curves for $Ba_3Mn_2O_8$ taken for fields applied perpendicular to the c axis. Successive temperature sweeps are offset by 0.2 μ_B for clarity.

6.1.1 Magnetization

Extraction magnetization measurements were performed in pulsed magnetic fields up to 60 T in a ^{3}He refrigerator for fields applied perpendicular to the c axis. Data were obtained by integrating the field derivative of the magnetization and are plotted for increasing fields in Figure 6.1(c). The data were cross calibrated with low field SQUID measurements to attain absolute values of the magnetization. Critical fields, evident as discontinuities in the slope of the magnetization, were determined from peaks in the second derivative of magnetization with respect to field. At base temperature, the data show no magnetization up to H_{c1}=8.73 T, followed by roughly linearly increasing magnetization as the dimers are populated with triplet states, and a plateau at 1 μ_B between H_{c2}=26.46 T and H_{c3}=32.42 T corresponding to one $S_z = 1$ triplet per dimer. There is then a second region of roughly linearly increasing magnetization as the quintuplet band is filled, before finally reaching the full saturation magnetization of 2 μ_B at H_{c4}=47.9 T.

The derivative of magnetization with respect to field is plotted in Figure 6.2 for various temperatures. The data were obtained by measuring the time derivative of both the magnetization and field, and taking the quotient. The signal to noise ratio diminishes at high fields, for which the field derivative tends to 0. These curves, shown for increasing fields, reveal clear peaks associated with each of the critical fields. For falling fields the field derivative is smaller, resulting in a worse signal to noise ratio. However, a representative curve for decreasing field at base temperature is plotted revealing the same qualitative behavior. The data also show a second peak to the right (left) of H_{c1} (H_{c2}) at low temperatures. These peaks do not mark phase transitions since there is no temperature dependence and the features are observed well above $T_{c,max}$=0.9 K, the highest ordering temperature. Rather, these features signify a zero temperature crossover between phase II and phase I of the singlet-triplet ordered states (leading to the rise in magnetization associated with the crossing of the singlet and triplet states).

Inspection of Fig. 6.2 reveals that at lowest temperature the peak at H_{c4} is significantly higher than the peaks at the other three critical fields. This critical field difference is observed on both increasing and decreasing fields, and thus is not a consequence of the nearly zero dB/dt at maximal applied fields. The origin of the peak enhancement will be discussed later in the section on asymmetry in the quintuplet condensate.

6.1.2 Heat Capacity and Magnetocaloric Effect

The high field phase diagram was determined by both magnetocaloric effect (MCE) and heat capacity experiments performed in a 45T hybrid superconducting/resistive magnet at ^{3}He temperatures for fields perpendicular to the c axis. For MCE measurements, transitions were determined from peaks in the derivative in the same manner as in the singlet-triplet regime (see Fig. 5.3(a)). These measurements revealed a single phase for fields between 34 T and 41 T (Fig. 6.3). The vertical shaded region corresponds to a temperature independent effect associated with a rapidly changing temperature derivative of magnetization at H_{c3}, identical to the features observed in

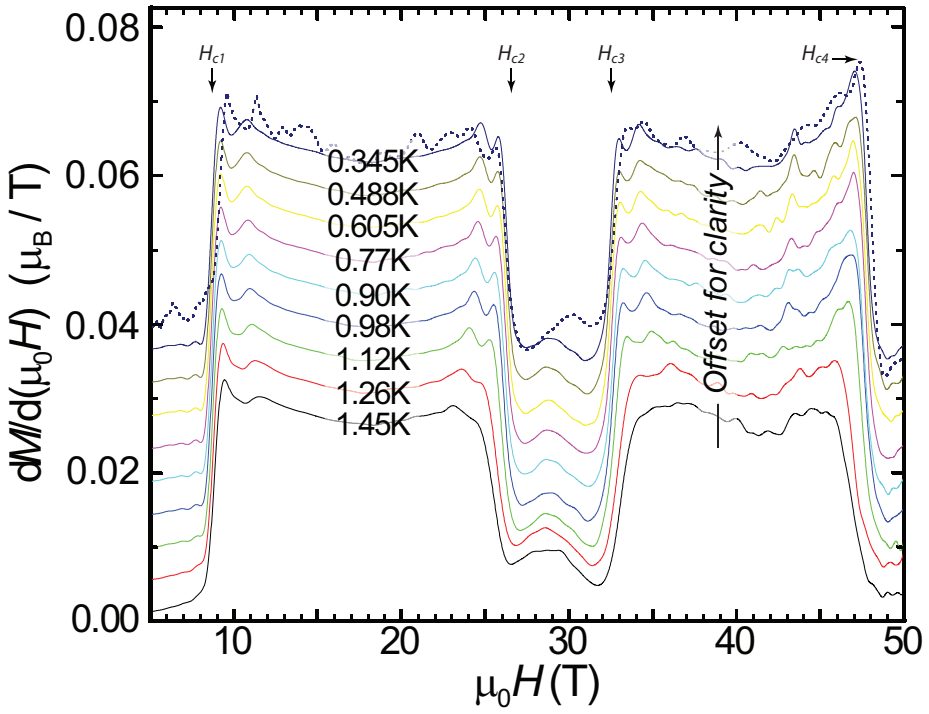

Figure 6.2: Field derivative of magnetization of $Ba_3Mn_2O_8$ for increasing fields applied perpendicular to the c axis. Successive temperature sweeps offset by 0.0045 μ_B/T for clarity. Dotted line shows representative magnetization derivative for decreasing fields at 0.345K, revealing no significant hysteresis.

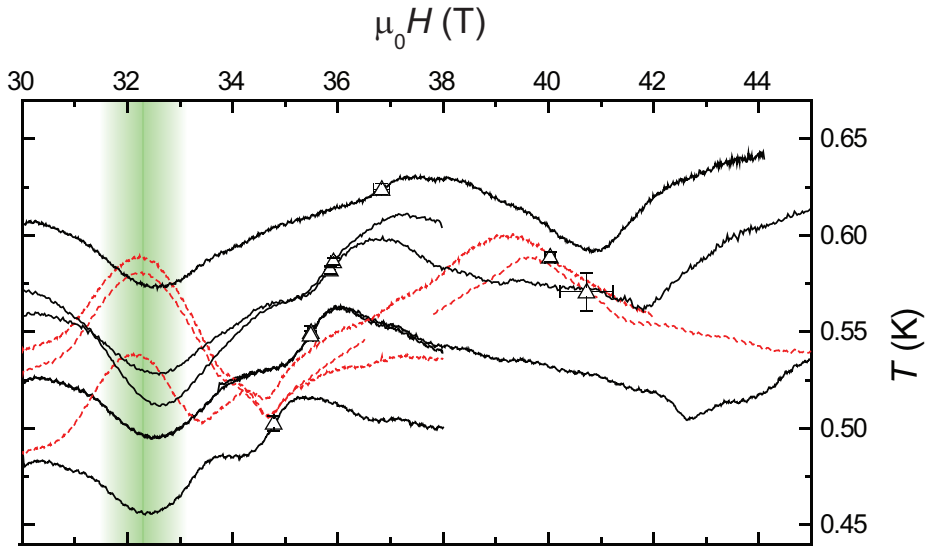

Figure 6.3: MCE curves plotted versus field for increasing field (solid black lines) and decreasing fields (dashed red lines) for fields applied perpendicular to the c axis. Phase transitions can be determined from peaks in derivative with respect to field, and are shown as open triangles. Vertical shading indicates broad maximum associated with rapidly changing temperature derivative of magnetization at the critical field.

the singlet-triplet regime (see Fig. 5.5).

Heat capacity measurements were performed using standard thermal relaxation time calorimetry, in the large ΔT limit. Accordingly, C_p is calculated from the instantaneous time derivative of the calorimeter temperature and the conductance of the thermal link and not averaged over the entire temperature range. For these experiments, the primary benefit of this technique is its expediency, which unfortunately comes at the cost of reduced accuracy. The reduced accuracy caused a small extraneous hysteresis on heating versus cooling. To improve the accuracy, multiple temperature curves were measured at each field and then averaged. The data taken on cooling are plotted in Fig. 6.4. They reveal an increasing critical temperature for fields leading up to 37 T which has the maximum $T_{c,max}$ of 0.643 $\pm$ 0.014 K. Above 37 T the critical temperature begins to decrease again. T_c values extracted from heat capacity data for both cooling and heating are shown as a lower and upper bound on the phase boundary in Fig. 6.5. The integrated entropy under the curve appears to track the critical temperature, such that a higher T_c implies more entropy.

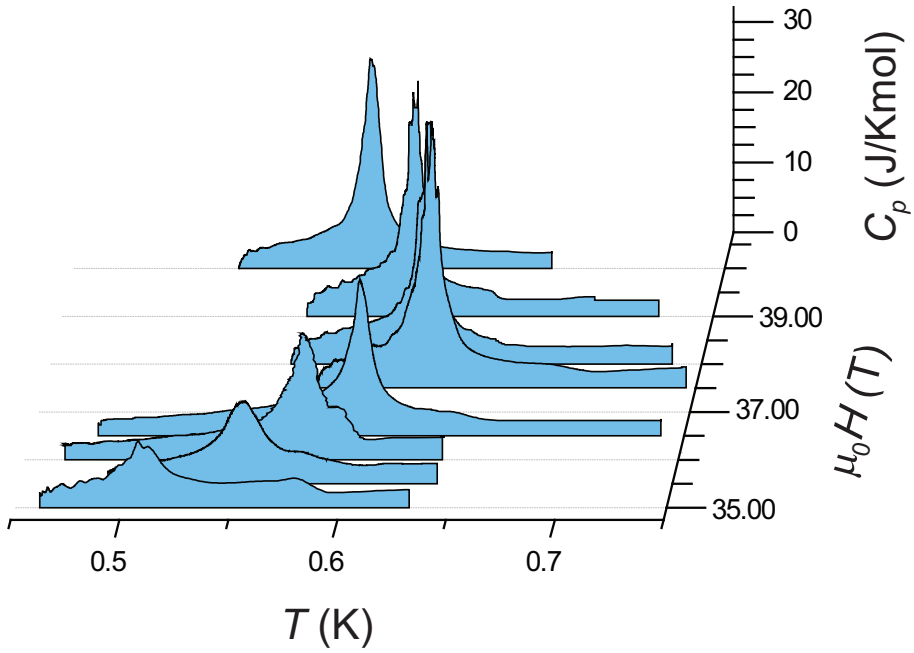

Figure 6.4: Heat capacity, taken on cooling, as a function of temperature for fields applied perpendicular to the c axis.

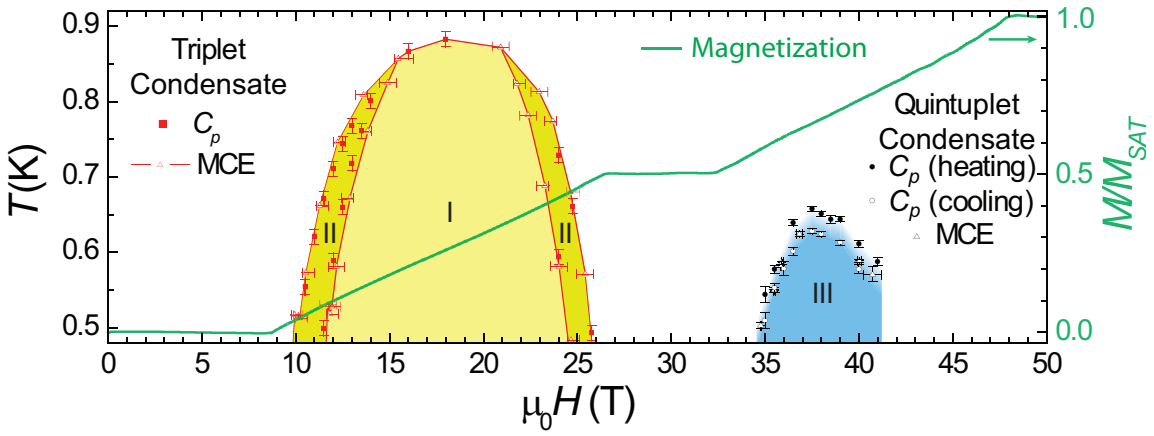

Figure 6.5: Phase diagram for fields applied perpendicular to the c axis. Representative magnetization curve for $T = 0.50$ K is shown for reference (right axis). Blue region corresponds to the quintuplet condensate (labeled phase III). Solid and open circles correspond to heat capacity data taken on heating and cooling respectively, illustrating the apparent hysteresis caused by the experimental technique. Dark and light yellow regions correspond to phase II and phase I of the triplet condensate.

The entire phase diagram for fields applied perpendicular to the c axis, together with a magnetization curve taken at 0.50K, are shown in Figure 6.5, revealing the four critical fields as discontinuities in the slope and the corresponding ordered states. All told the phase diagram reveals at least three distinct ordered states across a large field range. Inspection of this figure reveals a striking asymmetry in the quintuplet condensate, for which $T_{c,max}$ of the quinton phase is found at H=37 T, less than 5 T from H_{c3} but more than 10 T from H_{c4}. This effect will also be explored later in the section on asymmetry in the quintuplet condensate.

6.2 Comparison between Triplet-Quintuplet and Singlet-Triplet Regimes

The ability to microscopically determine the form of the triplet-quintuplet ordered state is even more difficult than direct determination of the singlet-triplet states due to the high fields required. However, predictions for the nature of the quintuplet

condensate ordered state can be made through analysis of the effective Hamiltonian (Eq. 2.32). Such predictions yield ordered states in this regime which are very similar to those found in the singlet-triplet regime (section 5.3) due to the near equivalence between the effective Hamiltonians of these regimes (Eqs. 2.31 and 2.32). In this section I will compare and contrast a few of the main features of the ordered states of both the singlet-triplet and triplet-quintuplet regimes through analyses of the effective Hamiltonians.

In a layered system such as $Ba_3Mn_2O_8$, the T_c of the ordered state is primarily determined by the 3D interactions in the system. This is a consequence of the the Mermin-Wagner-Berezinskii theorem which describes the disordering effects of thermal fluctuations in 2D systems at finite temperatures (i.e. a 2D system with a continuous symmetry can only order at T=0 due to the proliferation of spin waves at finite temperatures) [51]. A smooth evolution of the ordered states with the 3D interactions would dictate that the maximum T_c scales primarily with those interactions. In this system, the largest 3D interactions are the J_1 and J_4 exchanges between Mn ions on successive layers. The effective J_1 and J_4 interactions in the singlet-triplet regime are (from Eq. 2.31):

$$\begin{aligned}\tilde{\mathcal{H}}_{st,3D} &= J_1 \sum_{l\langle\langle i,j\rangle\rangle} \left[\frac{1}{4}\tilde{s}^z_{il}\tilde{s}^z_{jl+1} - \frac{4}{3}\left(\tilde{s}^x_{il}\tilde{s}^x_{jl} + \tilde{s}^y_{il}\tilde{s}^y_{jl}\right)\right] \\ &\quad + J_4 \sum_{l\langle\langle i,j\rangle\rangle'} \left[\frac{1}{4}\tilde{s}^z_{il}\tilde{s}^z_{jl+1} - \frac{4}{3}\left(\tilde{s}^x_{il}\tilde{s}^x_{jl} + \tilde{s}^y_{il}\tilde{s}^y_{jl}\right)\right] \end{aligned} \tag{6.1}$$

The equivalent effective interactions in the triplet-quintuplet regime are (from Eq. 2.32):

$$\begin{aligned}\tilde{\mathcal{H}}_{tq,3D} &= J_1 \sum_{l\langle\langle i,j\rangle\rangle} \left[\frac{1}{4}\tilde{s}^z_{il}\tilde{s}^z_{jl+1} - \left(\tilde{s}^x_{il}\tilde{s}^x_{jl} + \tilde{s}^y_{il}\tilde{s}^y_{jl}\right)\right] \\ &\quad + J_4 \sum_{l\langle\langle i,j\rangle\rangle'} \left[\frac{1}{4}\tilde{s}^z_{il}\tilde{s}^z_{jl+1} - \left(\tilde{s}^x_{il}\tilde{s}^x_{jl} + \tilde{s}^y_{il}\tilde{s}^y_{jl}\right)\right] \end{aligned} \tag{6.2}$$

These relations can be simplified at the middle of each the singlet-triplet and quintuplet ordered states, roughly where the maximum T_c will occur. Considering the singlet-triplet regime, at the midpoint of those ordered states the magnetization is halfway between its value at H_{c1} (where $S^z_{il1} + S^z_{il2} = 0$ for a given dimer when all dimers are singlets) and H_{c2} (where $S^z_{il1} + S^z_{il2} = 1$ for a given dimer when all dimers are singlets), the average magnetization per dimer will be $S^z_{il1} + S^z_{il2} = \frac{1}{2}$. Using the relation between the real spin operators and the pseudospin operators, $S^z_{il1} + S^z_{il2} = \tilde{s}^z_{il} + \frac{1}{2}$ (from section 2.3.1) it is clear that $\tilde{s}^z_{il} = 0$. Thus the ratio of the 3D interactions near the maximum T_c reduces to a simple value:

$$\frac{\tilde{\mathcal{H}}_{st,3D}}{\tilde{\mathcal{H}}_{tq,3D}}|_{T_{c,max}} \cong \frac{4}{3} \tag{6.3}$$

The maximum $T^{st}_{c,max}$ observed in the singlet-triplet regime is 0.883±0.010 K and the maximum $T^{tq}_{c,max}$ in the triplet-quintuplet regime is 0.643±0.014 K (Fig. 6.5). Thus the ratio of these maximum T_c's, $T^{st}_{c,max}/T^{tq}_{c,max} = 1.37 \pm 0.025$, is in good agreement with the theoretical ratio of these two T_c's, up to the inherent error in the measure of the maximum T_c.

The width of the two regimes also follows from the effective Hamiltonians. This quantity cannot be solely ascribed to a specific term, but must include all terms contributing to the bandwidth. Short of doing a full spin wave analysis to get an exact determination of the width of the phases, a first order approximation of the widths can be obtained with just the strongest interactions acting on the pseudospins, the J_2 and J_3 exchanges. The effective J_2 and J_3 interactions in the singlet-triplet regime are (from Eq. 2.31):

$$\tilde{\mathcal{H}}_{st,J_2J_3} = \sum_{l\langle i,j\rangle} \left[\frac{(J_2 + J_3)}{2} \tilde{s}^z_{il}\tilde{s}^z_{jl} + \frac{8\,(J_2 - J_3)}{3} \left(\tilde{s}^x_{il}\tilde{s}^x_{jl} + \tilde{s}^y_{il}\tilde{s}^y_{jl} \right) \right] \tag{6.4}$$

The equivalent J_2 and J_3 terms in the triplet-quintuplet regime are (from Eq. 2.32):

$$\tilde{\mathcal{H}}_{tq,J_2J_3} = \sum_{l\langle i,j\rangle} \left[\frac{(J_2 + J_3)}{2} \tilde{s}^z_{il}\tilde{s}^z_{jl} + 2\,(J_2 - J_3) \left(\tilde{s}^x_{il}\tilde{s}^x_{jl} + \tilde{s}^y_{il}\tilde{s}^y_{jl} \right) \right] \tag{6.5}$$

As opposed to the discussion of the maximum T_c, neither the $\tilde{s}_z$ nor the $\tilde{s}_x$ and $\tilde{s}_y$ pseudospin operators equal zero across the entire field range where the width is calculated. However, taking the two limits where either the $\tilde{s}_z$ pseudospin operator goes to 0 or the $\tilde{s}_x$ and $\tilde{s}_y$ operators go to 0 gives two extremes between which the measured ratio of the widths will be. Taking first the limit for which both $\tilde{s}_x$ and $\tilde{s}_y$ go to 0, the ratio of the J_2 and J_3 terms in the two regimes is:

$$\frac{\tilde{\mathcal{H}}_{st,J_2J_3}}{\tilde{\mathcal{H}}_{tq,J_2J_3}}|_{\tilde{s}_x=\tilde{s}_y=0} = 1 \tag{6.6}$$

The ratio of the J_2 and J_3 terms in the two regimes in the second limit where $\tilde{s}_z$ goes to 0 is:

$$\frac{\tilde{\mathcal{H}}_{st,J_2J_3}}{\tilde{\mathcal{H}}_{tq,J_2J_3}}|_{\tilde{s}_z=0} = \frac{4}{3} \tag{6.7}$$

These two values yield a fairly small range for the measured ratio. Using the critical fields determined from the magnetization, Fig. 6.1, the widths of the singlet-triplet regime and triplet-quintuplet regime are 17.73 T and 15.48 T, respectively. The measured ratio of the widths, $\Delta H_{st}/\Delta H_{tq} = 1.15$, right in the middle of predicted range.

The most obvious contrast between the two regimes is the lack of a second ordered state in the triplet-quintuplet regime. The effective Hamiltonian in the triplet-quintuplet regime has the single ion anisotropy term, $b(\theta) = -\frac{5\sin^2(\theta)D}{4J_0}$, which is $\frac{5}{8}$ as large as the equivalent single ion anisotropy term in the the singlet-triplet regime, $a(\theta) = -\frac{2\sin^2(\theta)D}{J_0}$. Further, the size of the competing Ising modulation of the pseudospins, $\frac{(J_2+J_3)}{2}\tilde{s}^z_{il}\tilde{s}^z_{jl}$, is unchanged between the two regimes, suggesting that a second ordered state in the triplet-quintuplet regime should exist and be roughly 40% smaller in field range than the phase II of the singlet-triplet regime. Additionally, the field derivative of the magnetization, which shows two peaks on entering and leaving the singlet-triplet regime that correspond to the zero temperature transition between phase I and phase II, shows similar pairs of peaks on entering and leaving the triplet-quintuplet regime. However, neither magnetocaloric effect nor heat capacity

measurements revealed a second ordered state. The most likely reason for this discrepancy is simply that the noise level associated with the measurements performed in the challenging high field environment obscured a second ordered state. In particular, at the high fields where these measurements were performed the field gradient acting on the liquid helium of the ^{3}He refrigerator was strong enough to cause the liquid helium to levitate within the ^{3}He pot, minimizing the length of time that the system could be maintained at base temperature. To accommodate this constraint measurements had to be performed quickly, sacrificing signal for expediency. The baseline noise level in the MCE measurements would obscure a jump of $\sim$0.005 K, the size of the temperature jump in the singlet-triplet regime on entering into phase II at 0.75 K, roughly the same percentage of the maximum T_c of the singlet-triplet dome as 0.5 K is for the triplet-quintuplet dome. The noise in the heat capacity measurement derive from the experimental method used, the instantaneous derivative technique. This technique is primarily used to measure first order phase transitions and could have missed a smaller feature indicative of second ordered state that would have been captured by the more standard discrete temperature points technique. Thus the most likely explanation is that a second ordered state was simply below the high noise level of these measurements, not absent.

6.3 Asymmetry near H_{c4}

Significant asymmetry was observed in both the field derivative of the magnetization, where the peak at H_{c4} is larger than the peaks at H_{c1}, H_{c2} and H_{c3}, and the phase diagram, where $T^{tq}_{c,max}$ of the triplet-quintuplet ordered states occurs at a field much closer to H_{c3} than H_{c4}. In this section I will describe how these asymmetries are a direct result of the asymmetry in the zero-point fluctuations of the paramagnetic phases at each critical field and induce the observed effects.

The zero-point fluctuations of this system must conserve total S^z because of the U(1) symmetry in this compound (although the U(1) symmetry is broken by the zero field splitting for fields away from the c axis, the symmetry will be present for temperatures above $\sim$0.37 K, the energy scale of the zero field splitting). Above H_{c4}

each dimer has its maximal $S^z = 2$ value, precluding any zero-point fluctuations at that critical field. In contrast, such fluctuations consisting of creation (annihilation) of $S^z = 2$ quintuplet-singlet pairs ($S^z = 1$ triplet-$S^z = 1$ triplet pairs) are present for $H_{c2} \leq H \leq H_{c3}$ as well as zero-point fluctuations consisting of creation (annihilation) of singlet-singlet pairs ($S^z = 1$ triplet-$S^z = -1$ triplet pairs) are present for $H \leq H_{c1}$. These fluctuations, when present, reduce the effective mass of the gapless bosons which describe the system at each of the critical fields. This can be easily appreciated by a thought experiment in which the field is fixed at some arbitrary value between H_{c2} and H_{c3} and the interdimer exchange couplings are increased by applying pressure. The applied pressure P will close the gap at a critical point ($P = P_c$) where H_{c2} becomes equal to H_{c3}, causing the single-particle excitation spectrum to become linear ($z = 1$). Such an XY quantum phase transition in $D = d + 1 = 4$ dimensions is driven by the zero-point (phase) fluctuations under consideration. A simple continuity argument implies that the boson mass has to be reduced by such fluctuations in order to get a massless spectrum when they diverge at $P = P_c$. In general, all spin dimer compounds should exhibit some degree of asymmetry because zero-point fluctuations are absent only in the highest field paramagnetic phase. The effect is especially striking in $Ba_3Mn_2O_8$ because $H_{c3} - H_{c2} \sim 6$T is considerably smaller than $H_{c4} - H_{c3} \sim 15.5$T, implying the gap in energy to create a zero-point fluctuation near H_{c3} is relatively small.

A more quantitative determination of the mass asymmetry was obtained through analysis of the boson dispersion by K. A. Al-Hassanieh and C. D. Batista [48]. At each critical field, the gapless bosons have a dispersion relation $\omega^\nu(\mathbf{q})$ that is quadratic at low energies. Since each boson is a quasiparticle that carries a unit of magnetization ($S^z = 1$) along the field direction, the boson density is the magnetization per site $\langle S^z_j \rangle$. The effective masses are determined from the diagonal components of the mass tensor, $m^{-1}_{\nu i} = \partial^2 \omega^\nu(\mathbf{q}) / \partial^2 q_i|_{\mathbf{q}=\mathbf{Q}}$, where $i = \{x, y, z\}$ and $\mathbf{Q}$ is the wavevector where $\omega^\nu(\mathbf{q})$ is minimized. In the dilute limit relevant for the regions around each of the quantum critical points, the inter-particle distance $\rho^{-1/3}$ (where ρ is the boson density) is much larger than the scattering length a (lattice parameter) of the hard-core repulsion between bosons. The effective boson-boson repulsion, $v_0 = \Gamma_{\mathbf{0}}(\mathbf{Q}, \mathbf{Q})$,

is obtained from a ladder summation [52]:

$$\Gamma_{\mathbf{q}}\left(\mathbf{k},\mathbf{k}'\right)=V_{\mathbf{q}}-\int_{-\pi}^{\pi}\frac{d^3p}{8\pi^3}V_{\mathbf{q}-\mathbf{p}}\frac{\Gamma_{\mathbf{p}}\left(\mathbf{k},\mathbf{k}'\right)}{\omega^{\nu}(\mathbf{k}+\mathbf{p})+\omega^{\nu}(\mathbf{k}'-\mathbf{p})}. \tag{6.8}$$

Here $V_{\mathbf{q}}=U+\left(J_2+J_3\right)\gamma_{\mathbf{q}}^2+\frac{J_1}{2}\gamma_{\mathbf{q}}^1+\frac{J_4}{2}\gamma_{\mathbf{q}}^4$, where $U\rightarrow\infty$ comes from the hard-core repulsion, the rest of the terms come from nearest neighbor repulsion terms and $\gamma_{\mathbf{q}}^n$'s are defined as follows:

$$\begin{aligned}
\gamma_{\mathbf{q}}^1 &= \cos\left(q_3\right)+\cos\left(q_3-q_1\right)+\cos\left(q_3-q_2\right)\\
\gamma_{\mathbf{q}}^2 &= \cos\left(q_1\right)+\cos\left(q_2\right)+\cos\left(q_1-q_2\right)\\
\gamma_{\mathbf{q}}^4 &= \cos\left(q_3+q_1-q_2\right)+\cos\left(q_3-q_1+q_2\right)\\
&\quad +\cos\left(q_3-q_1-q_2\right),
\end{aligned} \tag{6.9}$$

where q_n's refer to the principal reciprocal axes. The dispersions $\omega^{\nu}(\mathbf{q})$ were computed by using a generalized spin-wave approach. For the paramagnetic (PM) region near each QCP, a mean field treatment of the effective interaction v_0 leads to a renormalized chemical potential $\tilde{\mu}_{\nu}=\mu_{\nu}-2v_0\rho$ with $\mu_{\nu}=g\mu_B\left(-1\right)^{\nu}\left(H_{c\nu}-H\right)$ [5]. Low temperature thermodynamic properties were computed from the renormalized chemical potential in the PM region around each QCP. The striking asymmetry between H_{c4} and the rest of the critical fields follows from the fact that the corresponding masses $m_{4\parallel}=1.9357K^{-1}$ and $m_{4\perp}=0.4531K^{-1}$ are roughly two times larger than the masses at the other three critical fields: $m_{3\parallel}=0.7834K^{-1}$, $m_{3\perp}=0.1833K^{-1}$, $m_{2\parallel}=0.6977K^{-1}$, $m_{2\perp}=0.1633K^{-1}$, and $m_{1\parallel}=0.9133K^{-1}$, $m_{1\perp}=0.2138K^{-1}$.

The asymmetry observed in the thermodynamic measurements can be readily understood in the context of these mass asymmetries, $m_{4i}/m_{3i}\simeq 2.4711$. Considering first the field derivative of the magnetization, the magnitude of the peaks at the critical fields is determined by the number of low-energy excited states available at each critical point. The larger effective mass at H_{c4} thus implies a larger density of states, reflected in the enhanced peak at that field. The condensation temperature ($\tilde{\mu}(T=T_c)=0$) near the critical fields for a 3D BEC scaling class is also related to the effective mass of the bosons at each critical field: $T_c\propto\rho^{2/3}m_{\nu}^{-1}\propto\left|H-H_{c\nu}\right|^{2/3}m_{\nu}^{-1/3}$. The

increased effective mass at H_{c4} reduces the ordering temperature, causing the phase boundary to be steeper near H_{c3} than near H_{c4}. The effect of the entropy tracking T_c, and not the maximal particle condensation, is also produced by the asymmetry in the zero-point fluctuations that shift the maximum of the order parameter towards the critical field with larger fluctuations (H_{c3} for the triplet-quintuplet phase).

These mass asymmetries also played a role in the not perfectly symmetric ordered states of singlet-triplet regime as well. In particular, phase II is slightly narrower closer to H_{c1} than H_{c2}, which is expected from the different effective masses, $m_{2i}/m_{1i} \simeq 0.7639$.

Chapter 7

Effect of partial substitution of non-magnetic ions: Low Field Behavior of $Ba_3((Mn_{1-}x)V_x)_2O_8$

Adding disorder to a system can dramatically effect the groundstates that arise. In the context of spin dimer systems in particular this has not been extensively explored, with the diluted system $TlCu_{1-x}Mg_xCl_3$ being the only widely studied example [53]. In this regard, $Ba_3Mn_2O_8$ provides a wonderful opportunity to explore the effects of non-magnetic substitution. In particular, $Ba_3(Mn_{1-x}V_x)_2O_8$ is a model diluted spin dimer compound, for which the partial substitution of non-magnetic $3d^0$, $S = 0$ V^{5+} leads to unpaired $3d^2$, $S = 1$ Mn^{5+} moments. In this chapter I study this compound in the low field state, observing the effects of disorder on the zero field singlet ground state. I will first introduce some background on the theoretical groundstates for a magnetically diluted system, then show extensive susceptibility and heat capacity studies for several different dilutions at low fields, and finally interpret these results in terms of the possible ground states. The low field portion of this work has been published in ref. [32].

In Appendix C preliminary studies of the high field ordered states of this disordered system are presented.

7.1 Site Diluted Groundstates

Randomness can lead to intriguing magnetic states not typically available to perfectly ordered systems. The archetypal example is the spin glass state, found for a wide variety of disordered materials with either site or bond randomness [54]. In contrast, for gapped systems with a singlet ground state, substitution of non-magnetic elements can introduce local moments, ultimately leading to long range magnetic order due to the effective interaction mediated by the background singlet state - one manifestation of "order by disorder" (OBD). For example, both the Spin-Peierls compound $CuGeO_3$ and the spin ladder compound $SrCu_2O_3$ have gapped ground states without long range order; however diluting either system with a small amount of nonmagnetic Zn or Mg ions onto the $S = \frac{1}{2}$ Cu site induces antiferromagnetic order [55, 56, 57]. It is not clear whether this effect should be uniformly anticipated for all gapped systems, motivating both theoretical and experimental interest aimed at exploring the properties of disordered spin-gap materials.

The broad category of spin dimer compounds provides a simple means to study the effect of non-magnetic substitution on a singlet ground state. Recently, quantum Monte Carlo (QMC) simulations have been performed for the specific case of spin dimers arranged on a square lattice with antiferromagnetic nearest neighbor and next nearest neighbor exchange [58, 59]. These calculations revealed that for an appropriate range of concentrations, substitution of non-magnetic impurities leads to long range order in zero magnetic field. The predicted wave-vector is the same as that found for the stoichiometric parent compound subjected to fields above the critical field. It would be highly desirable to experimentally test whether such an OBD state is found for a real material conforming to the simple effective spin Hamiltonian used in this calculation. Unfortunately, there are not currently any suitable candidate materials that match these requirements for which substitution of non-magnetic species is possible over an appreciable range of concentrations. Conversely, it would be equally interesting to see how geometric frustration affects the stability of the OBD phase. Here, unfortunately, quantum Monte Carlo simulations are prohibitively difficult due to the frustration induced sign problem, and we must resort to experiment to provide

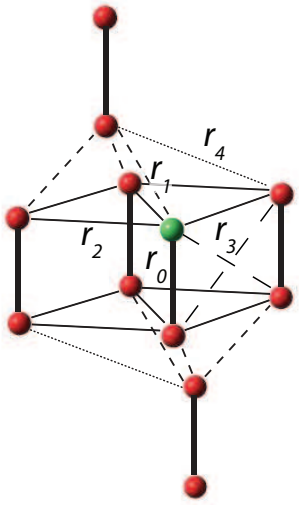

Figure 7.1: Schematic diagram showing the transition metal sublattice of the dimer compound $Ba_3(Mn_{1-x}V_x)_2O_8$. Mn ions are shown in red and a single substituted V ion shown in green. The Mn ion vertically below the V ion is now no longer paired and hence contributes a local magnetic moment. Distances between the V ion and its nearest neighbors r_0 - r_4 are labeled.

insight. In this case, though, there are luckily several candidate materials to which we can turn. One such material is $Ba_3(Mn_{1-x}V_x)_2O_8$. In this chapter I probe this compound, revealing that at low temperatures the system does not exhibit long range order or spin glass behavior but may manifest instead a random singlet phase.

$Ba_3V_2O_8$ is isostructural to $Ba_3Mn_2O_8$. However in contrast to the strongly magnetic Mn^{5+} ion, V^{5+} corresponds to a $3d^0$ electron configuration and hence is nonmagnetic. Partial substitution of V in $Ba_3Mn_2O_8$ therefore leads to unpaired Mn moments (Fig. 7.1) [60].

The probability of finding at least one unpaired moment within a distance r_i of a given unpaired moment, $P_{x,tot}(r_i)$, is plotted in Fig. 7.2(a) for the relevant V concentrations studied here (assuming no clustering as data suggest). This probability is determined by taking 1 less the probability that no unpaired moment is within a distance r_i of a given a unpaired moment. The probability that no unpaired moments are within a distance r_i of a given unpaired moment is determined by multiplying the probabilities that there are no unpaired moments at each successive distance r_j up

to r_i ($j \leq i$), taking account of the number of equivalent sites Z_j in the jth shell: $1 - P_{tot,x}(r_i) = \prod_{j=0}^{i}(1-x)^{Z_j}$. For the highest dilution studied here, $x = 0.456$, $P_{x,tot}(r_4) = 0.59$.

The probability of the nearest unpaired moment being a distance r_i away from a given unpaired moment, $P_x(r_i)$, is given by the probability that no unpaired moments are within a distance r_{i-1} times the probability that there is an unpaired moment at a distance r_i, again taking account of the number of equivalent sites Z_j in the jth shell: $P_x(r_i) = \left(\prod_{j=0}^{i-1}(1-x)^{Z_j}\right) \times \left(1-(1-x)^{Z_i}\right)$. For each of the concentrations studied here the most likely distance between nearest neighboring V ions is the r_2 pairing (Fig. 7.2(b)).

7.2 Experimental Results

Low-field susceptibility measurements of $Ba_3(Mn_{1-x}V_x)_2O_8$ for $0 \leq x \leq 0.046$ were performed using a commercial Quantum Design MPMS XL SQUID magnetometer for fields of 1000 Oe applied perpendicular to the c-axis and are shown in Fig. 7.3(a). Results were fit to the same dimer model used to fit the undiluted compound, which included a mean field correction, a term corresponding to Curie-Weiss paramagnetic behavior and a temperature independent term (Eqs. 2.3 and 3.3). The full model is:

$$\begin{aligned} \chi_{iso} &= \frac{2N_A\beta g^2\mu_B^2\left(1+5e^{-2\beta J}\right)}{3+e^{\beta J}+5e^{-2\beta J}} \\ \chi_{total} &= \alpha\frac{\chi_{iso}}{1+\lambda\chi_{iso}} + \frac{C}{T-\theta} + \chi_0 \end{aligned} \tag{7.1}$$

Here $\lambda = 3\left[J_1 + J_4 + 2\left(J_2 + J_3\right)\right]/N_A g^2\mu_B^2$ is the mean field correction to account for interdimer exchange. N_A is Avogadro's number, $\beta = 1/k_BT$ and α is the number of dimers per mole (where 1 mol refers to the formula unit of $Ba_3(Mn_{1-x}V_x)_2O_8$, such that $\alpha = 1$ for $x = 0$). Recent INS studies found a negligible concentration dependence of both the spin gap Δ and the triplet bandwidth for $x < 0.05$ [34]. Therefore values of $J_0 = 16.42$ K, $J_1 + J_4 + 2\left(J_2 + J_3\right) = 5.31$ K and $g = 2.07$

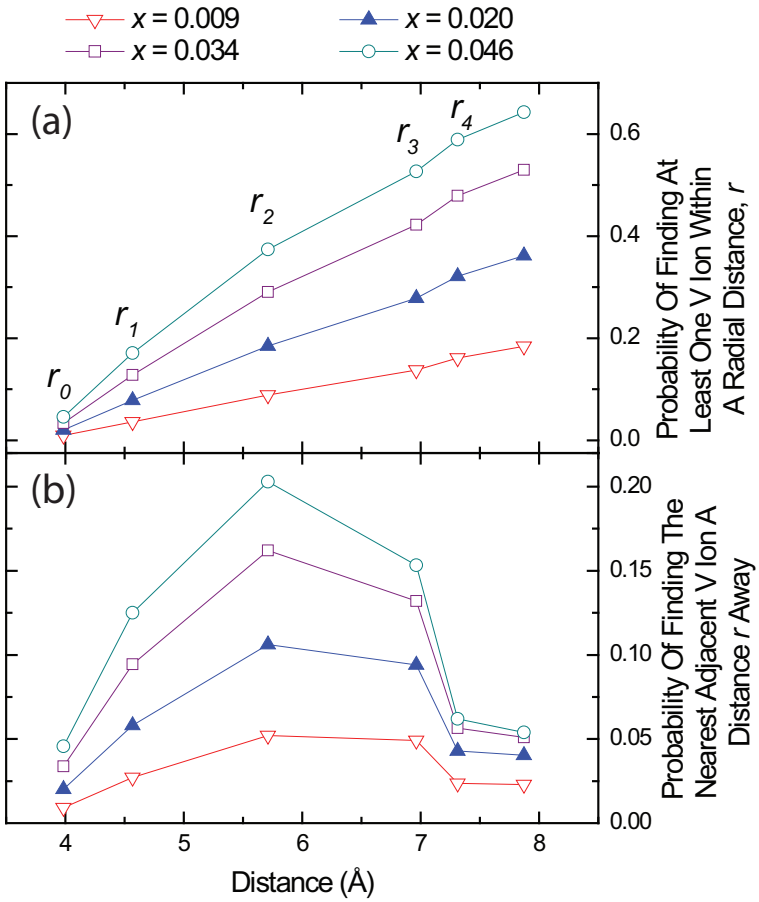

Figure 7.2: (a) Probability, assuming no clustering, of finding the nearest neighboring V ion a distance r from the substituted ion, shown for the specific vanadium concentrations (x) studied, and for the specific distances $r_0 - r_5$. (b) Probability of finding at least one V ion within a distance r from the substituted ion.

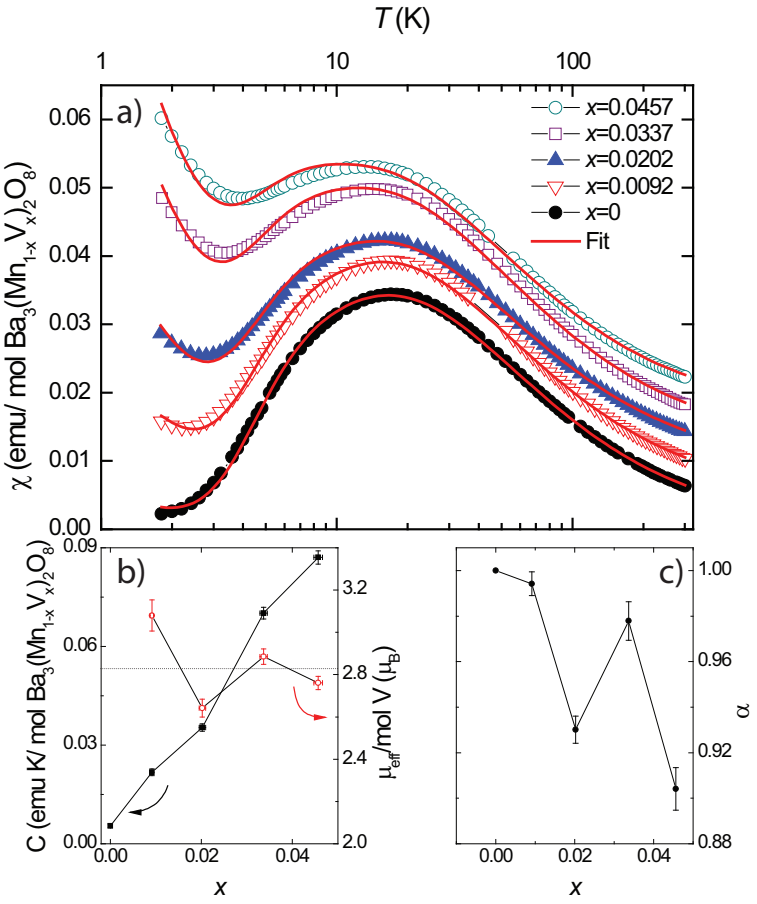

Figure 7.3: (a) Susceptibility as a function of temperature for single crystals of $Ba_3(Mn_{1-x}V_x)_2O_8$ (compositions listed in legend). Successive curves are offset by 0.004 emu/mol for clarity. Data are fit (red lines) by a dimer model, described in the main text, including a mean-field correction to account for interdimer interactions, a temperature-independent term, and a Curie-Weiss term to account for the unpaired magnetic impurities introduced by V-substitution. Values for the exchange constants were held fixed at the values obtained for the stoichiometric compound. (b) Curie constant, C (left axis), and the associated effective moment per V, μ_{eff}/x (right axis). Note that V^{5+} is non-magnetic, and that the moment arises from the unpaired Mn^{5+} S=1 spin on the broken dimers. Horizontal line shows the anticipated effective moment $\mu_{eff} = g\sqrt{S(S+1)}\mu_B = 2.83\ \mu_B$ for Mn^{5+}. (c) The number of dimers per mole, α.

determined from the fit of the undiluted $Ba_3Mn_2O_8$ measurement (solid black circles) were held fixed in the fits of the other samples. These fixed values are in rough agreement with the values measured from INS and EPR, of $J_0 = 18.78$ K, $J_1 + J_4 + 2(J_2 + J_3) = 11.03$ K and $g = 1.96$, up to the inherent limitations of this fit. The Curie constant C, extracted from these fits, is plotted against the left axis in Fig. 7.3(b), and varies essentially linearly with V concentration. The effective moment per mole of V is readily determined from the Curie constant C:

$$\mu_{eff} = 2.827\sqrt{CT} = g\sqrt{S(S+1)}\mu_B \tag{7.2}$$

The effective moment, which is plotted against the right axis of Fig. 7.3(b), is independent of V concentration within the uncertainty of the measurement. Observed values are close to those anticipated for Mn^{5+}, implying that each V impurity results in a single unpaired Mn^{5+} spin. That is, substitution V does not appear to result in clustering, but rather, as anticipated in Fig. 7.2, the number of doubly-broken dimers is very small, and the majority of V impurities occupy half of a dimer site paired with a magnetic Mn^{5+} ion. The fit parameter α, shown in panel (c), nominally scales with (1-x), but provides a much less sensitive measure of the number of unbroken dimers than does the Curie susceptibility for these low concentrations.

Heat capacity (C_p) studies were performed with a Quantum Design physical properties measurement system (PPMS) using standard thermal relaxation-time calorimetry. These measurements were performed in temperatures between down to 50 mK and fields up to 0.5 T parallel to the c axis. Data are shown in Fig. 7.4(a) for the temperature interval 50 to 500 mK. The stoichiometric parent compound, $Ba_3Mn_2O_8$ ($x = 0$, black filled circles) exhibits only a very small heat capacity in this temperature interval due to the much larger energy scale of the spin gap. A small temperature dependence due to the phonon contribution is barely discernable, but can be seen more clearly when similar data for $Ba_3V_2O_8$ are plotted over a wider temperature interval in Figure 7.6(b). In contrast, samples with $x > 0$ reveal dramatically different behavior. The heat capacity is approximately two orders of magnitude larger, and exhibits a broad maximum centered at approximately 100 mK. For x=0.009 and 0.020

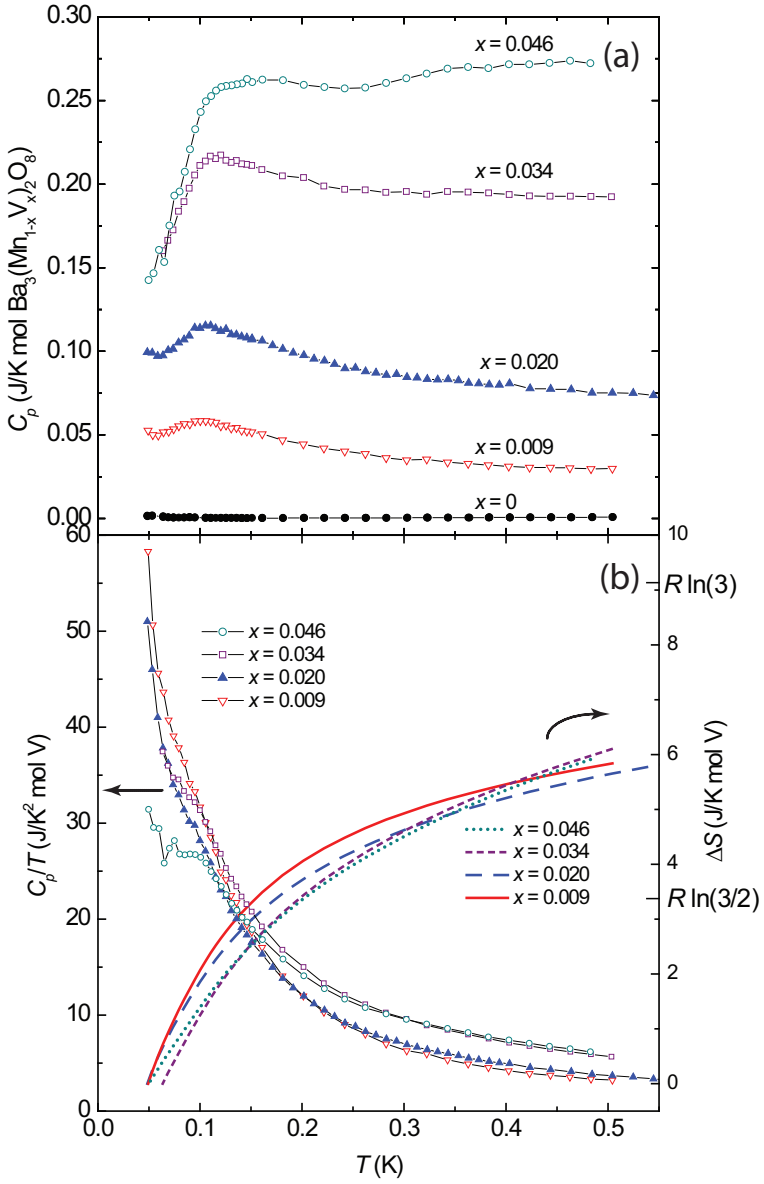

Figure 7.4: (a) Low temperature heat capacity of $Ba_3(Mn_{1-x}V_x)_2O_8$ in zero field. Substitution vanadium leads to a substantial increase in the total heat capacity. (b) Left axis: The same data, plotted as C_p/T and scaled by V concentration, revealing the evolution in the functional form of heat capacity. Right Axis: Change in entropy ΔS between 50 mK and 500 mK associated with the total heat capacity. Despite subtle changes in the functional form of the heat capacity as the vanadium concentration is increased, the integrated entropy per mole of V over this temperature window remains remarkably similar.

there is a slight indication of an additional upturn in the heat capacity at the lowest temperatures. This is not observed for the higher two V concentrations, x=0.034 and 0.046, which also exhibit a progressive broadening of the feature at 100 mK, and, for x=0.046, a gradual increase in the heat capacity from 200 mK to 500 mK. Significantly, none of the concentrations studied exhibit a sharp anomaly characteristic of a phase transition.

The same data shown in panel (a) of Fig. 7.4 are replotted as C_p/T normalized by the vanadium concentration $2x$, in panel (b). Scaled in this way, it is clear that C_p approximately scales with x. The change in entropy, ΔS over this temperature window can be estimated from the area under these curves, and is plotted against the right axis of panel (b), also normalized per mole of V. The small phonon contribution has negligible effect on this estimate over this temperature range, as can be readily appreciated by inspection of the data in panel (a). Inspection of panels (a) and (b) of Fig. 7.4 reveals a progressive change in the T-dependence of the heat capacity and entropy as the vanadium concentration increases. For the higher vanadium concentrations, relatively more entropy is removed per increment of temperature at high temperature than for lower concentrations, and vice versa at the lowest temperatures. This concentration dependence is, however, rather subtle, and the most remarkable aspect of the data is that the total entropy removed over this interval is almost identical for all four compositions, despite a factor of 5 difference in the vanadium concentration. This value [$\sim$ 6 J/K mole (V)] is approximately 60% of the total magnetic entropy $S_{total} = R\ln(3)$ (where R is the molar gas constant) associated with the unpaired S=1 magnetic Mn ions induced by the vanadium substitution.

The heat capacity data for the V-substituted samples shown in Fig. 7.4(a) reveal a broad maximum centered at approximately 100 mK for all four compositions. In the absence of any other interactions, uniaxial single ion anisotropy, represented by a term $D\,(S^z)^2$ in the spin Hamiltonian, will split the $S^z = 0$ and $S^z = \pm 1$ triplet states of unpaired Mn moments. A calculation of the expected contribution to the specific heat in zero field is shown in Fig. 7.5 for the specific case of $x = 0.020$ (red line), using the value of D = -0.024 meV previously determined from EPR measurements of diluted $Ba_3(Mn_{1-x}V_x)_2O_8$. The maximum value occurs at a temperature very close to that

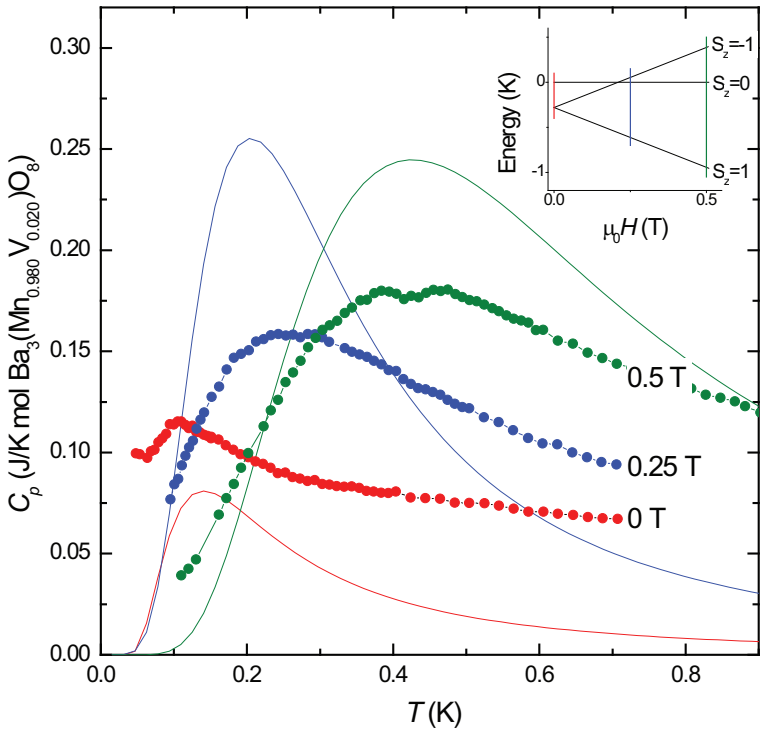

Figure 7.5: Heat capacity of $Ba_3(Mn_{0.980}V_{0.020})_2O_8$ in magnetic fields of 0 T, 0.25 T and 0.5 T, shown as red, blue and green points, respectively. Lines show the theoretical heat capacity for the Schottky anomaly associated with an isolated $S = 1$ spin with single ion anisotropy D = -0.024 meV in the same fields. Inset shows the appropriate energy spectrum for this calculation. Vertical lines indicate the three different fields for which measurements were performed.

observed in experiment (solid red circles), indicating that the experimentally observed features are likely related to Schottky behavior. To further test this hypothesis, the heat capacity was also measured in applied field of 0.25 T and 0.5 T (green and blue data points in Fig. 7.5), and compared with calculated values (blue and green lines). The applied field splits the $S^z = \pm 1$ states (inset to Fig. 7.5), resulting in broadening of the Schottky anomaly and a shift in the maximum value to higher temperatures. The experimental data reveal very similar behavior, confirming that this feature is closely related to the Schottky behavior anticipated for unpaired Mn spins.

The correspondence between the calculated Schottky anomaly and the experimentally determined heat capacity is, however, not perfect. Inspection of Fig. 7.5 reveals a significant discrepancy between the magnitude of the theoretical curves and the experimental data, even though the temperature at which the maxima occur agrees. This difference is particularly striking for the 0 T data, for which the measured heat capacity is uniformly larger than the theoretical prediction, indicating that the magnetic entropy associated with the full triplet $S = 1$ state is progressively removed over a fairly broad temperature interval. For non-interacting moments, the doublet ground state should remain unsplit. Hence the anticipated entropy associated with the Schottky anomaly in zero field is $S^\star = 2x[R\ln(3) - R\ln(2)] = 2xR\ln(3/2)$ (where $2x$ is the number of moles of free Mn ions). In contrast, the measured magnetic entropy between 50 mK and 500 mK (Fig. 7.4(b)) is considerably larger than this value. Comparison of the measured heat capacity in zero field with the calculated Schottky behavior indicates that much of this difference occurs at a temperature considerably above the energy scale set by the single ion anisotropy. Higher order terms in the crystal field expansion would only lead to splitting on a lower energy scale than the leading axial term and cannot account for this difference. Nor does it seem likely that the progressive removal of entropy above 0.2 K is due to a spread of values of D since the total entropy would still rise to $2xR\ln(3/2)$, and also since the anomaly centered at 100 mK is not especially broadened. The data therefore indicate that the interactions between the free moments play a significant role. Indeed, the magnitude of the Schottky anomaly itself appears to be smaller than anticipated for the given concentration, but superimposed on top of a large and only weakly temperature

dependent background, which must then arise from these interactions. This is also borne out by measurements made in applied field.

In the presence of a magnetic field the $S^z = \pm 1$ doublet is split, leading to an overall increase in the magnitude of the calculated heat capacity (blue and green lines in Fig. 7.5). For 0.25 T the measured heat capacity exceeds the calculated value for temperatures greater than 0.4 K, indicating the removal of magnetic entropy at higher temperatures, similar to the zero field data. The area under the calculated blue and green curves is the full magnetic entropy of the free $S = 1$ spins, corresponding to $S^{\dagger} = 2xR\ln(3)$. If some of this magnetic entropy is removed at higher temperature due to interactions between Mn moments, then there will be less magnetic entropy available at low temperatures, which is presumably why the measured heat capacity in 0.25 T falls below the calculated curve for temperatures below 0.4 K. Data for 0.5 T appear to follow the same general form: more magnetic entropy is removed at higher temperature than would be anticipated for isolated Mn ions, reducing the magnitude of the low temperature Schottky anomaly.

Measurements of the heat capacity for $x = 0.020$ were extended to higher temperatures in order to integrate the magnetic entropy over a wider temperature window (black data points in Fig. 7.6(a)). Two additional contributions to the entropy become significant above 0.5 K: the phonon contribution, and a magnetic contribution arising from thermal population across the spin gap associated with the intact dimer triplet states. However, a reasonably accurate estimate of the magnetic heat capacity due to the unpaired Mn ions (ΔC_{mag}, blue line) can be obtained by subtracting the heat capacity of the stoichiometric parent compound, $Ba_3Mn_2O_8$ (red squares). The corresponding change in entropy ΔS between 50 mK and 2 K (right hand axis) is 0.291 J/K mol, substantially surpassing $S^{\star} = 2xR\ln(3/2) = 0.135$ J/K mol.

For comparison, the heat capacity was also measured over this temperature range for a crystal with $x = 0.980$, containing approximately the same concentration of unpaired Mn moments as the $x = 0.020$ sample. For $x = 0.020$ the small concentrations of V impurities introduces unpaired magnetic Mn ions, which interact via the singlet "sea" arising from the majority of unbroken dimers. In contrast, for $x = 0.980$,

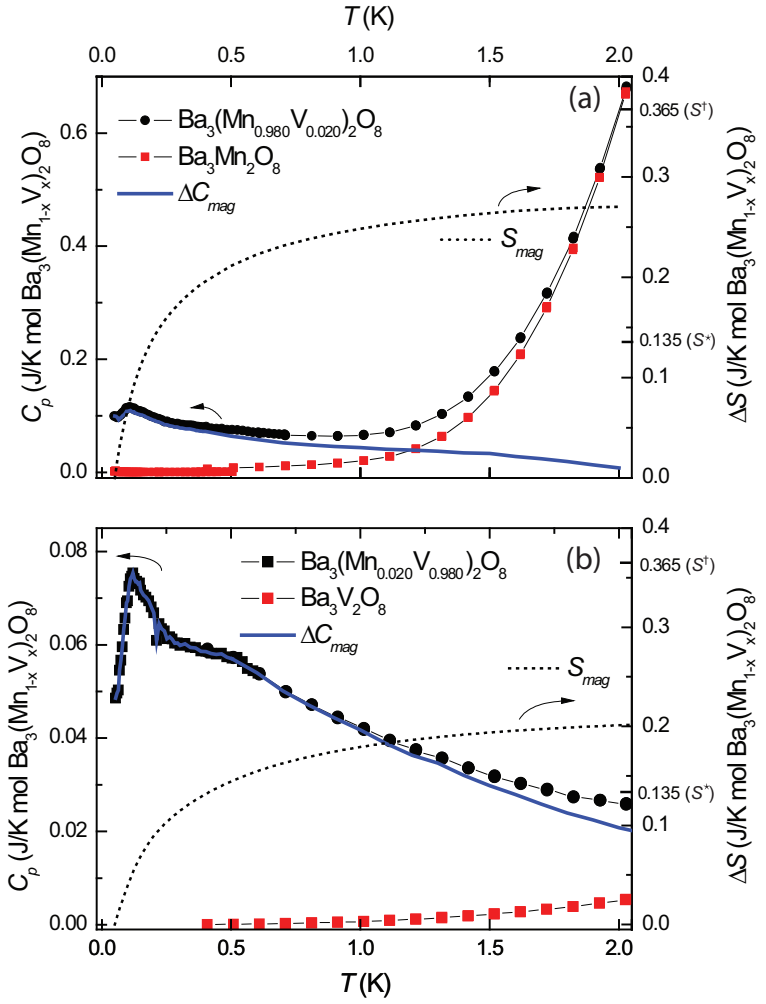

Figure 7.6: a) Heat capacity of $Ba_3(Mn_{0.978}V_{0.020})_2O_8$, $Ba_3Mn_2O_8$ and the difference at 0 T shown in black circles, red squares and blue line, respectively, plotted along the right axis. The change in entropy calculated from the difference is plotted as a black dotted line along the right axis. b) Heat capacity of $Ba_3(Mn_{0.020}V_{0.980})_2O_8$, $Ba_3V_2O_8$ and the difference at 0 T shown in black circles, red squares and blue triangles, respectively. The change in entropy calculated from the difference is plotted as a black dotted line along the right axis.

$Ba_3V_2O_8$ provides an "empty" magnetic background in which the Mn impurities interact. Data are shown in Fig. 7.6(b), together with an estimate of the magnetic contribution to the heat capacity (ΔC_{mag}, blue line) obtained by subtracting the heat capacity of $Ba_3V_2O_8$ (red squares). ΔC_{mag} rises with decreasing temperature, and appears to begin to curve over below approximately 0.5 K. Below 0.2 K a clear Schottky anomaly is observed, with the maximum centered at 110 mK. The magnitude of the anomaly is comparable to that found for $x = 0.020$, presumably for the same reason that a substantial amount of the total magnetic entropy is removed at higher temperatures. The integrated entropy between 50 mK and 4 K is 0.271 J/K mol. Measurements to higher temperature are hampered by systematic errors introduced by uncertainty in measurements of the sample mass for the two crystals used in these measurements. However, it is clear that the integrated entropy over this window far exceeds that which would be estimated if the $S^z = \pm 1$ doublet remains degenerate, $S^\star = 0.136$ J/K mol. Hence, for both x=0.020 and 0.980, it appears that interactions between unpaired Mn moments leads to progressive removal of magnetic entropy over a wide temperature range. And in both cases a relatively small number of moments remain to a low enough temperature to contribute to the observed Schottky anomaly associated with the single ion anisotropy zero field splitting. In neither case is there any evidence of a phase transition down to 50 mK.

7.3 Discussion

In the absence of long range magnetic order, it is reasonable to consider whether the low temperature state of $Ba_3(Mn_{1-x}V_x)_2O_8$ is a spin glass, the archetypal ground-state for systems with disorder. In canonical spin glass systems, the temperature dependence of the heat capacity and magnetic entropy scales with moment concentration [61, 62]. Such systems exhibit a only broad feature in the heat capacity, the maximum of which occurs at a temperature slightly above the freezing temperature, with roughly 80% of the total magnetic entropy is accounted for above T_F. For example, in CuMn, an increase in the Mn concentration by an order of magnitude increases the freezing temperature by greater than a factor of 5, such that the magnetic

entropy is collected over a much wider temperature range. However, the behavior in $Ba_3(Mn_{1-x}V_x)_2O_8$ is quite different; in this case the entropy is collected over an equivalent temperature range independent of vanadium concentration (Fig. 7.4(b)). Thus it is unlikely that the groundstate is a canonical spin glass.

An alternative groundstate for disordered systems is the random singlet phase. This state, which does not exhibit long range order, is characterized by formation of local singlets [63]. Microscopically, as temperature is decreased the pair of most strongly coupled moments forms a singlet; then as temperature is further decreased the pair of remaining moments with strongest coupling forms a singlet, and so on until all the moments are paired. This state was first proposed to account for the low-temperature susceptibility and heat capacity of lightly doped semiconductors, in particular Si:P [64, 65, 66, 67, 68], and has since been of much theoretical and experimental interest for one dimensional disorder systems [69, 70, 71, 72, 73, 74]. The dominant thermodynamic signature of this phase is the susceptibility which diverges as T^α with $-1 < \alpha < 0$ at low temperatures (i.e a sub-Curie law), as observed in both Si:P, Cd:S and the one dimensional systems $MgTiOBO_4$ and $MnMgB_2O_5$ [66, 67, 70, 72]. Additionally, it was found that the heat capacity of Si:P increases with decreasing temperature for the lowest concentrations over an appreciable range of temperatures reflecting the progressive removal of magnetic entropy upon cooling [68].

A scenario in which the ground state of $Ba_3(Mn_{1-x}V_x)_2O_8$ is a random singlet phase is qualitatively consistent with the experimental observations. Consideration of the relevant exchange energies serves to illustrate whether collective or local behavior is expected to dominate. Specifically, a comparison of the maximum exchange energy between two impurities ($J_{max}\mathbf{S}_i \cdot \mathbf{S}_j$) with the average total exchange energy resulting from interaction with all of the neighboring impurities ($\sum_i Z_i P_{x,i} J_{ij}$, where Z_i is the number of coordinating sites with exchange J_{ij} and $P_{x,i}$ is the probability that these sites are occupied) distinguishes whether a random singlet phase or collective magnetic order (for example a spin glass) is favored. For vanadium concentrations up to the maximum studied, $x = 0.046$, it is straightforward to show that the random singlet phase is favored. As an example, for the case of $x = 0.046$ we first consider

a free Mn moment for which the nearest unpaired Mn is a distance r_2 away (recall that J_2=0.256 meV is the strongest exchange interaction after J_0). In comparison, the average sum of further interactions acting on the free Mn moment, which would be appropriate for a mean field treatment, is $3(0.046)J_1 + 6(0.046)J_3 + 3(0.046)J_4 = 0.060$ meV. The clear energetic advantage of singlet formation continues when progressively smaller exchange couplings are considered after removal of all J_2-bonded pairs, and so on (a crude version of the "decimation" procedure first introduced to describe random singlet formation [63]). This is due to the combined actions of the hierarchy of exchange interactions found in $Ba_3Mn_2O_8$, the small size of the Mn moment ($S = 1$), and the low concentration of magnetic impurities. This crude analysis clearly shows that the exchange between a single pair of spins dominates over more collective behavior, implying that a random singlet state is theoretically favored over a spin glass state, at least for the concentration regime considered here.

To further test this view, a model of the random singlet phase in $Ba_3(Mn_{1-x}V_x)_2O_8$ was undertaken in order to make a quantitative comparison with the measured heat capacity data. The model is an approximation of the previously described "decimation" process [63], with three changes: (1) we do not recalculate the probability of finding successively weaker random singlet pairs after each round of decimation (this leads to an overestimate of the probability of smaller pairing distances); (2) the exchange interaction between two unpaired moments forming a singlet is not renormalized by other exchanges between neighboring moments; and (3) we explicitly include the effect of single ion anisotropy. Limitations of this model are discussed below. The total heat capacity is calculated by summing over the probability that two moments with exchange $J(r)$ will pair, $P_x(J(r))$ times the heat capacity for two moments with exchange $J(r)$:

$$C_{p,tot}(T) = \sum_{J(r)} P_x(J(r)) C_p(J(r), T) \tag{7.3}$$

Details of the heat capacity calculation for two moments with exchange J are given in the Appendix B.2. The exchange between neighboring impurities $J(r)$ was determined by the distance between impurities. For neighboring impurities a distance

$r \leq r_4$ apart, the exchange was approximated as the exchange determined from INS measurements of the undiluted system [27, 28]. For neighboring impurities at a distance $r > r_4$ the effective exchange is approximated as a decaying exponential as expected for localized moments: $J(r) = J'e^{-r/r'}$, where the parameters J' and r' were determined from fits of the known exchanges J_1 through J_4. The probability $P_x(J(r))$ was determined by finding the distance between an impurity and the neighboring impurity with which it has the strongest exchange and was calculated similarly to $P_x(r)$, shown in Fig. 7.2(b). An important distinction between $P_x(J(r))$ and the previously calculated probability $P_x(r)$ is that the relative hierarchy of exchange constants does not exactly follow that of the physical separation of sites, shown in Fig. 7.1 (b). Specifically, $J_2 > J_3 > J_1 > J_4$, whereas $r_1 < r_2 < r_3 < r_4$. $P_x(J(r))$ is determined similarly to $P_x(r_i)$, the probability that the nearest unpaired moment is a distance r_i away from a given unpaired moment: $P_x(J(r_i)) = \left(\prod_{j=0}^{i-1}(1-x)^{Z_j}\right) \times \left(1-(1-x)^{Z_i}\right)$. The probabilities are calculated for a sequence of exchanges, with corresponding distances and coordination numbers, in which each successive exchange is smaller than all the previous exchanges. Finally, for $r > r_4$, successive shells of widths dr_n are taken, such that the number of atoms in each shell corresponds to a 5% increase in probability (i.e. $P_x(J(r_n)) = 0.05$ where $r_n = r_{n-1} + dr_n$).

Both the estimated exchange model and also the probability functions used in this model are approximations. The "bare" exchange values, determined from INS measurements, were used but effective exchange values between unpaired Mn moments on broken dimers will be renormalized by the presence of the surrounding singlet states. In particular, geometric frustration naturally leads to a reduction in the effective exchange from the bare values, as can be understood from an example. Two unpaired Mn moments connected by the J_2 exchange have an antiferromagnetic exchange with the third intact singlet dimer of the frustrated triangular structure. These antiferromagnetic exchanges induce an effective second order ferromagnetic exchange between the unpaired moments, reducing the overall value of the exchange between the unpaired moments. The model further approximates the exchange for $r > r_4$, in which the real effective exchange most likely does not vary perfectly exponentially for intermediate r since the superexchange depends sensitively on bond angles and bond

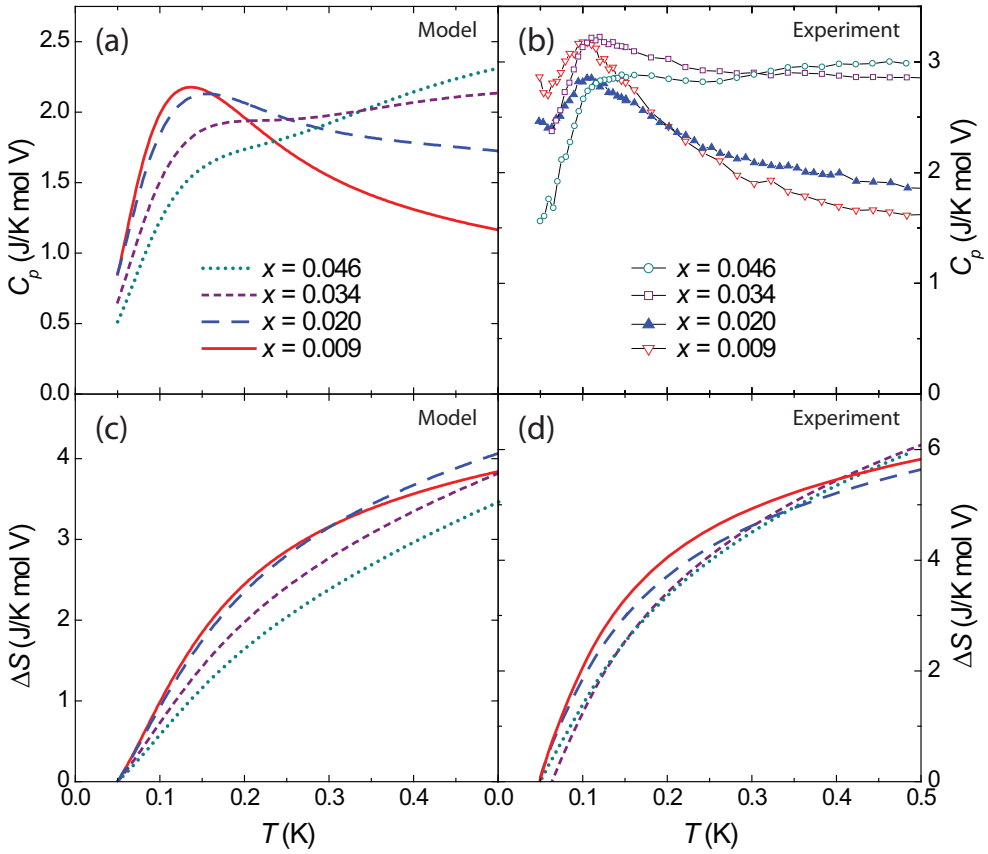

Figure 7.7: Calculated (a) heat capacity and (c) change in entropy of $Ba_3(Mn_{1-x}V_x)_2O_8$ scaled by vanadium concentration resulting from the random singlet model as described in the text. Experimental (b) heat capacity and (d) change in entropy shown for comparison.

lengths. Also, $P_x(J(r))$ overestimates the probability of smaller pairing distances. This can be understood by considering an impurity i with nearest neighboring impurity j. If there is a third impurity k which is closer to impurity j than impurity i, then impurity j pairs with impurity k and not impurity i, implying that impurity i pairs with a fourth impurity further away than impurity j, shifting probability to longer pairing distances. Nevertheless, as shown below, this crude model appears to capture the observed behavior at a semi-quantitative level, justifying its consideration in terms of an initial description of the data.

The calculated heat capacity and entropy for the different vanadium concentrations experimentally studied are shown in Fig. 7.7(a) and (c), respectively. The calculated data are in qualitative agreement with the experimental data, shown for comparison in panels (b) and (d). For $x = 0.009$ and $x = 0.020$, the model heat capacity increases as temperature decreases, reaching a maximum at the single ion Schottky peak before decreasing at lower temperatures. For $x = 0.034$ and $x = 0.046$ the model heat capacity decreases monotonically as temperature decreases, with a shoulder at the single ion anisotropy Schottky peak.

The model entropy is also consistent with the experimental data (Fig. 7.7(c) and (d), respectively). In spite of the five times difference in the vanadium concentration, which leads to a significant change in the probability distribution of exchange values of the random singlets, the change in entropy from 50 mK to 500 mK determined from the model rises to roughly the same value of $\sim$0.38 J/K mol V = 0.42 $R\ln(3)$ independent of vanadium concentration, in accordance with the experimental data. By extending the model calculations to both lower and higher temperatures, the change in entropy for all vanadium concentrations eventually reached the maximum available entropy, $R\ln(3)$. However, the smaller vanadium concentrations recover most of the unaccounted entropy below 50 mK while the higher vanadium concentrations recover most of the unaccounted entropy above 500 mK. In this sense it is somewhat coincidental that the experimentally accessible temperature window of 50 - 500 mK leads to an almost concentration independent change in entropy.

Further calculations of the heat capacity for the x=0.020 vanadium concentration in fields of 0.25 T and 0.50 T are shown in Fig. 7.8. The calculated heat capacity matches the qualitative behavior of the experimental data much better than the previous heat capacity calculations which were based solely single ion anisotropy (Fig. 7.5). In particular, the random singlet calculation, in addition to matching the temperature of the maxima of the experimental data, also exhibits a similar peak height and width as the experimental data.

Despite the successful description of the evolution of the T-dependence of the heat capacity as a function of composition, both the calculated heat capacity and entropy are uniformly smaller than the experimental data, reflecting limitations of the

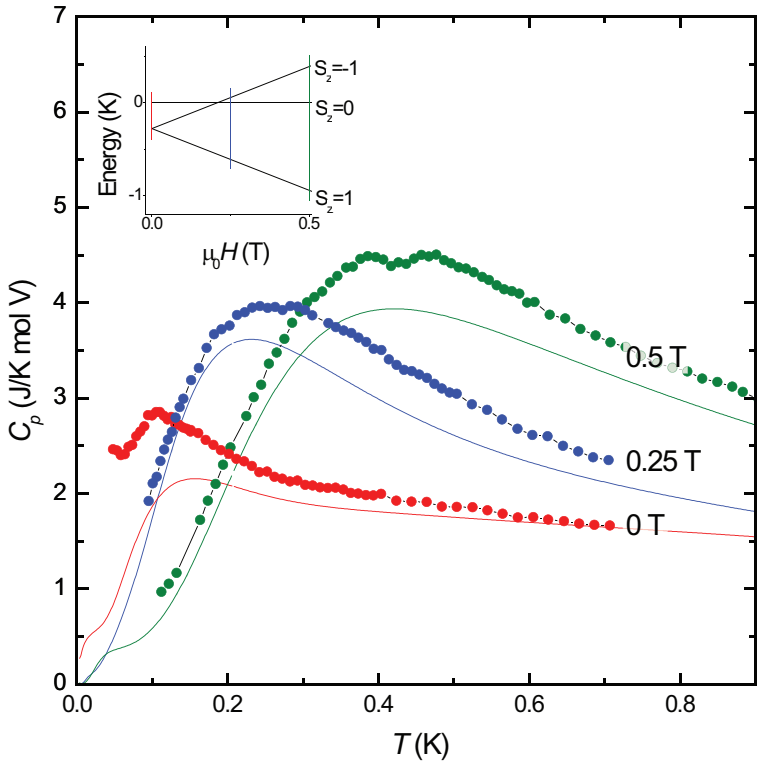

Figure 7.8: Calculated (solid lines) and experimental (solid circles) heat capacity of $Ba_3(Mn_{0.980}V_{0.020})_2O_8$ scaled by vanadium concentration in fields of 0 T, 0.25 T and 0.5 T in red, blue and green resulting from the random singlet model as described in the text.

simplified exchange model used for the calculations. In particular, both the effective exchange $J(r)$ and the pairing probability $P_x(J(r))$ used in the calculations were approximations as described earlier. However, the overall agreement is reasonable based on these approximations, lending considerable weight to the hypothesis that $Ba_3(Mn_{1-x}V_x)_2O_8$ realizes a random singlet phase at low temperature, at least for the range of concentrations studied in this report. Ongoing susceptibility measurements may be able to confirm this hypothesis.

Finally, although the current data clearly indicate the absence of long range order to 50 mK, an ordering transition cannot be ruled out to occur at a lower temperature. However, the relatively small magnetic entropy that remains at this temperature, and the progressively larger physical separation of unpaired moments due to random singlet behavior, makes long range order at a lower temperature rather unlikely.

Chapter 8

Summary and Outlook

In this brief chapter I will recap the work presented here before presenting some future directions to expand off these results.

8.1 Summary

The main thrust of this thesis has been the exploration for novel magnetic states, in particular in the spin dimer compound $Ba_3Mn_2O_8$. Some of the order was as predicted; some was unexpected. Ultimately, both the anticipated and unanticipated states demonstrate why spin dimer compounds are such a rich playground when searching for exotic ground states.

The phase diagram for the singlet-triplet regime of $Ba_3Mn_2O_8$ was mapped out through several different thermodynamic measurements [29, 31]. The significant anisotropy of this system, stemming from the easy axis single ion anisotropy, led to a single ordered state observed for fields parallel to the c axis and two states observed for fields away from the c axis. Further measurements of the angular evolution of these phases was Analysis of the minimal spin Hamiltonian was performed based on these thermodynamic results as well as the dominant exchanges pathways between spins in this system as determined from inelastic neutron scattering studies [26, 27, 28]. This analysis yielded two candidate incommensurate phases, which for fields away from the c axis, had modulation of the ordered moment. High field NMR

[33] and neutron scattering studies [50] circumstantially confirmed these proposed ordered states.

The triplet-quintuplet regime was explored through both magnetization and heat capacity measurements [30]. Only one previously spin dimer compound contained quintuplet ordered states, which were only cursorily studied, making this the first direct observation of a spin dimer triplet-quintuplet ordered state. Only one ordered state was found in this regime regardless of field direction. The absence of a second phase in this regime was attributed to poor signal-to-noise ratio in the high field environment. Significant asymmetry in this region was observed in both the phase diagram and the density of states. Zero point fluctuations, which are absent at the maximum field of this region but present at the minimum field, were found to induce this asymmetry.

Low field studies of the non-magnetically diluted compound $Ba_3(Mn_{1-x}V_x)_2O_8$ revealed an intriguing ground state without long range order down to 50 mK [32]. Heat capacity measurements revealed a Schottky anomaly centered at ∼110 mK, induced by to the single ion anisotropy, superimposed on a slowly varying background without any sharp features. The total heat capacity did not vary in a manner consistent with a spin glass phase, the archetypal site disordered ground state. Instead, numerical studies of the system found that the groundstate was consistent with a random singlet phase. Ongoing low temperature AC susceptibility measurements have the potential to confirm this hypothesis.

8.2 Future Directions

There are several clear avenues of further research that could build upon these results presented here in the search for novel order. The random singlet phase was presented as the possible groundstate for the lightly diluted system $Ba_3(Mn_{1-x}V_x)_2O_8$. This state, which has been the subject of much theoretical research [63, 64, 64, 69, **?**], has been previously experimentally observed only in lightly diluted semiconductors, primarily Si:P [66, 67, 68], and several one dimensional diluted chain compounds [70, 71, 72]. However, there are not any 3D insulating system with such a groundstate.

Searching for other materials, with the appropriate range of exchanges and impurity concentrations, could reveal more about this intriguing phase in a new and different context.

The effects of disorder in spin dimer compounds can be dramatic. In the most widely studied site diluted spin dimer compound $Tl(Cu_{1-x}Mg_x)Cl_3$, disorder in the form of non-magnetic Mg site dilution induces magnetic order at zero field [53, 75]. This order extends from zero field into the singlet-triplet ordered state, indicating that the zero field gap between the triplet and singlet states has been destroyed [76]. In contrast, Quantum Monte Carlo simulations of a non-magnetically doped square lattice spin dimer system predicted long range order at zero field ("order by disorder") but with an intact spin gap to the excited triplet states [58, 59]. Such a system still has a field regime where most of the dimers form singlets without long range magnetic order, such that the low field ordered state and high field ordered state are separated in field. Finding a new non-magnetically diluted system with small interdimer exchanges as compared to the intradimer exchange which also exhibits a zero field ordered state can elucidate whether the low field state can be purely impurity based ordering which is separated from the high field ordered state or whether the order must extend over the entire field range.

Ultimately, spin dimer compounds are worth studying because of the novel field induced order in these compounds. The form of the ordered states depends intimately on the nature of the microscopic interactions between dimers. The ability to "engineer" the form of that interaction by finding compounds with the appropriate exchange, or through application of chemical or external pressure on an existing compound, is what makes spin dimers such an intriguing playground when searching for novel order. For instance, the supersolid state, which has not been conclusively observed in any system, would be an exciting ordered state to find in a spin dimer compound [14]. It is this ability to observe intriguing quantum phases in a different setting that motivates further study of spin dimer compounds.

Appendix A

Dispersion of the Triplet Mode

The magnetic excitation dispersion, which is a basic property of a quantum magnet, is determined from the relevant interactions of the system. In $Ba_3Mn_2O_8$ the lowest energy excitation of the zero field singlet groundstate propagate according to the triplet dispersion. Inelastic neutron scattering studies (INS) performed by M. B. Stone mapped the complete triplet dispersion [26, 27, 28]. By fitting the experimental data to the theoretical form of the dispersion the dominant exchanges of this system were determined. In this appendix I will derive this theoretical form of the triplet dispersion following the previous derivation of C. D. Batista [49].

The random phase approximation (RPA) has been a useful technique for describing the dispersion of spin dimer systems including $KCuCl_3$, $TlCuCl_3$ and $BaCuSi_2O_6$ [77, 78, 79, 10]. The RPA dispersion for dimers linked by a Heisenberg exchange is:

$$\hbar\omega(\mathbf{Q}) = \sqrt{\Delta^2 + M^2\Delta\mathcal{J}(\mathbf{Q})R(T)} \tag{A.1}$$

Here M^2 is the transition matrix element, $M^2 = \frac{4}{3}S[S+1] = \frac{8}{3}$, $\mathcal{J}(\mathbf{Q})$ is the sum of all the interdimer interactions acting on a dimer, $\Delta = J_0$ in this approximation and $R(T)$ is the thermal population difference between the ground state and the three excited triplet states. Through simple analysis of the partition function for an isolated dimer

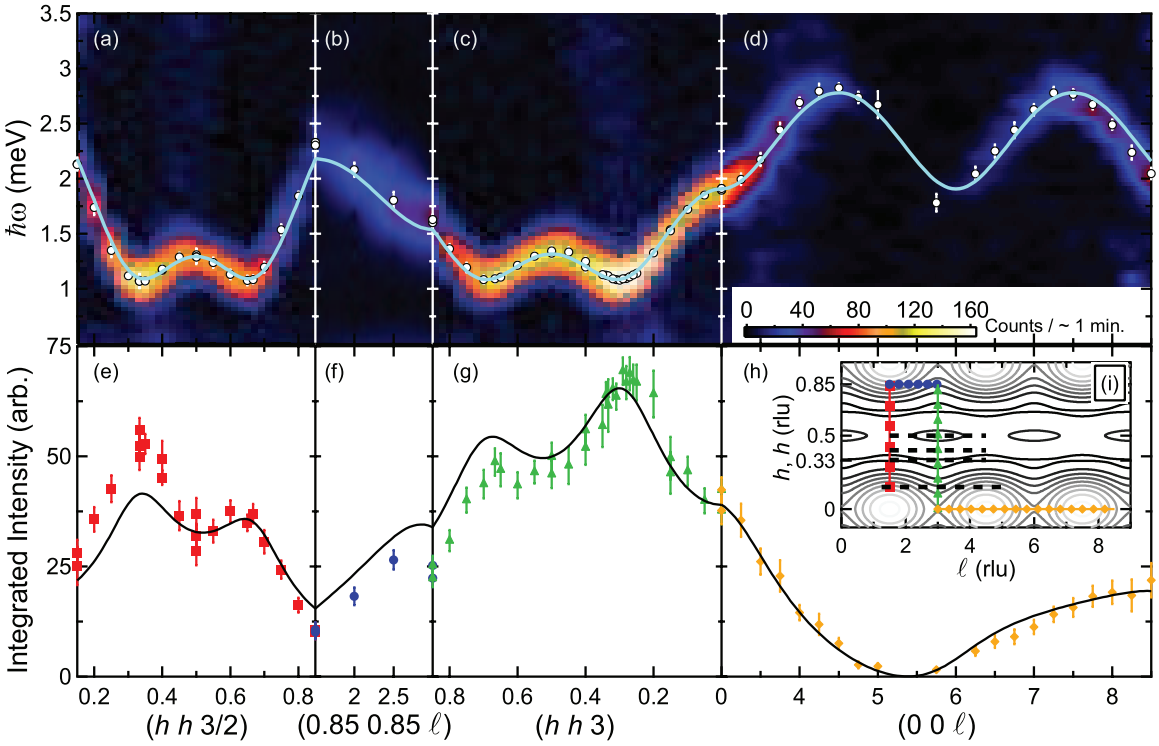

Figure A.1: INS studies and fitted form of triplet dispersion versus reciprocal lattice units (rlu) taken from work by M. B. Stone, *et al.* [27]. (a)-(d) Scattering intensity vs $\hbar\omega$ and $\mathbf{Q}$ for scans in (hhl) plane. Solid line is the fitted dispersion. (e)-(h) Integrated scattering intensity from Gaussian fits to constant $\mathbf{Q}$ scans. Solid line is the fitted dispersion. (i) Path through the (hhl) plane shown in (a)-(h).

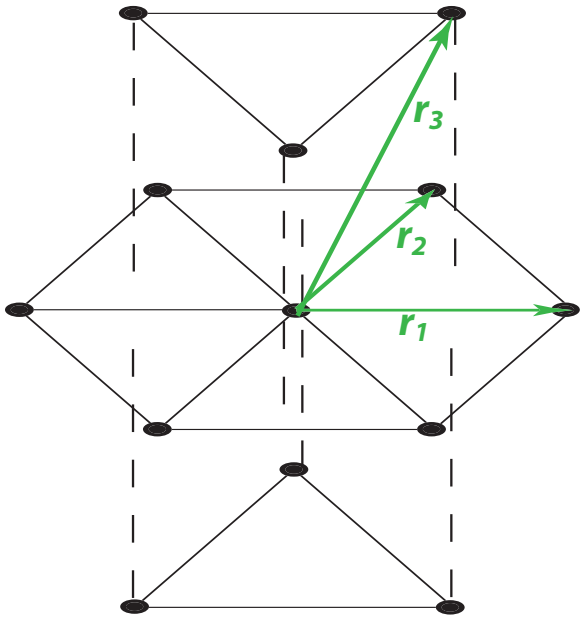

Figure A.2: Reduced magnetic dimer lattice illustrating basis vectors used in dispersion calculation

system, the form of $R(T)$ is:

$$R(T) = \frac{1 - e^{-\Delta\beta}}{1 + 3e^{-\Delta\beta} + 5e^{-3\Delta\beta}} \tag{A.2}$$

where $\beta = 1/k_B T$. At $T = 0$ K in the weakly coupled limit, where the interdimer exchanges are much less than the zero field gap between the singlet and excited triplet states, the dispersion simplifies:

$$\hbar\omega(\mathbf{Q}) = \Delta + M^2\mathcal{J}(\mathbf{Q})/2 = \Delta + \frac{4\mathcal{J}(\mathbf{Q})}{3} \tag{A.3}$$

Because $\mathcal{J}(\mathbf{Q})$ is determined in the dimer basis and the J_2 and J_3 exchanges connect the same dimers, it is impossible to extract the dispersion dependence of those two terms independently. Determining the exact functional form of the $\mathcal{J}(\mathbf{Q})$ requires determining the Fourier sum of all the relevant interdimer exchanges, $\frac{J_{i\mu j\nu}}{2}\mathbf{S}_{i\mu} \cdot \mathbf{S}_{j\nu}$. This is done by accounting for the hopping term of each of the exchanges in the magnetic dimer lattice (Fig. A.2). Considering first the six neighbors connected by

the J_2 and J_3 exchanges, (including a factor of 2 to account for the top and bottom of the dimer):

$$\begin{aligned}\omega_2(\mathbf{Q}) &= 2\left(\frac{J_2-J_3}{2}\right)[\cos(\mathbf{Q}\cdot\mathbf{r_1})+\cos(\mathbf{Q}\cdot\mathbf{r_2})+\cos(\mathbf{Q}\cdot(-\mathbf{r_1}+\mathbf{r_2}))\\ &\quad+\cos(\mathbf{Q}\cdot(-\mathbf{r_1}))+\cos(\mathbf{Q}\cdot(-\mathbf{r_2}))+\cos(\mathbf{Q}\cdot(\mathbf{r_1}-\mathbf{r_2}))]\\ &= 2\,(J_2-J_3)\,[\cos(\mathbf{Q}\cdot\mathbf{r_1})+\cos(\mathbf{Q}\cdot\mathbf{r_2})+\cos(\mathbf{Q}\cdot(\mathbf{r_1}-\mathbf{r_2}))] \qquad \text{(A.4)}\end{aligned}$$

Here J_3 component is negative because the s^+ and s^- pseudospin operators of dimers flip signs from the top to the bottom of a dimer which are connected by this bond (see theory section) . The J_2 component is positive because it connects the same half of dimer, which will square the sign of the s^+ and s^-, necessarily leaving it positive. Considering first the six neighbors connected by the J_1 exchange (recall that each dimer has a J_1 exchange with dimers on both the layer above and below):

$$\begin{aligned}\omega_1(\mathbf{Q}) &= \left(\frac{J_1}{2}\right)[\cos(\mathbf{Q}\cdot\mathbf{r_3})+\cos(\mathbf{Q}\cdot(\mathbf{r_3}-\mathbf{r_1}))+\cos(\mathbf{Q}\cdot(\mathbf{r_3}-\mathbf{r_2}))\\ &\quad+\cos(\mathbf{Q}\cdot(-\mathbf{r_3}))+\cos(\mathbf{Q}\cdot(-\mathbf{r_3}+\mathbf{r_1}))+\cos(\mathbf{Q}\cdot(-\mathbf{r_3}+\mathbf{r_2}))]\\ &= J_1\,[\cos(\mathbf{Q}\cdot\mathbf{r_3})+\cos(\mathbf{Q}\cdot(\mathbf{r_3}-\mathbf{r_1}))+\cos(\mathbf{Q}\cdot(\mathbf{r_3}-\mathbf{r_2}))] \qquad \text{(A.5)}\end{aligned}$$

Considering finally the six neighbors connected by the J_4 exchange (again recall that each dimer has a J_4 exchange with dimers on both the layer above and below):

$$\begin{aligned}\omega_4(\mathbf{Q}) &= \left(\frac{J_4}{2}\right)[\cos(\mathbf{Q}\cdot(\mathbf{r_3}-\mathbf{r_1}+\mathbf{r_2}))+\cos(\mathbf{Q}\cdot(\mathbf{r_3}-\mathbf{r_1}-\mathbf{r_2}))+\cos(\mathbf{Q}\cdot(\mathbf{r_3}+\mathbf{r_1}-\mathbf{r_2}))\\ &\quad+\cos(\mathbf{Q}\cdot(-\mathbf{r_3}-\mathbf{r_1}+\mathbf{r_2}))+\cos(\mathbf{Q}\cdot(-\mathbf{r_3}+\mathbf{r_1}-\mathbf{r_2}))+\cos(\mathbf{Q}\cdot(-\mathbf{r_3}+\mathbf{r_1}+\mathbf{r_2}))]\\ &= J_1\,[\cos(\mathbf{Q}\cdot(\mathbf{r_3}-\mathbf{r_1}+\mathbf{r_2}))+\cos(\mathbf{Q}\cdot(\mathbf{r_3}-\mathbf{r_1}-\mathbf{r_2}))+\cos(\mathbf{Q}\cdot(\mathbf{r_3}+\mathbf{r_1}-\mathbf{r_2}))]\end{aligned} \qquad \text{(A.6)}$$

The full dispersion is simply the sum of these three terms:

$$\mathcal{J}(\mathbf{Q}) = \omega_2(\mathbf{Q}) + \omega_1(\mathbf{Q}) + \omega_4(\mathbf{Q}) \tag{A.7}$$

Initial inelastic neutron scattering data taken on powder samples were fit to this functional form of the dispersion [26]. Further inelastic neutron scattering data taken on single crystal samples further refined this fit [27], while an erratum corrected the sign of some of the exchange constants [28]. This measurements ultimately yielded best fit values for the relevant exchange constants of: $J_0 = 1.642$ meV, $J_1 = 0.118$ meV, $J_2 - J_3 = 0.1136$ meV and $J_4 = 0.037$ meV.

Appendix B

Isolated Dimer With Single Ion Anisotropy Energy Spectrum

In this appendix I will calculate the energy spectrum for two spins with an antiferromagnetic exchange and a zero field splitting term:

$$\mathcal{H} = J\mathbf{S}_1 \cdot \mathbf{S}_2 + D\left((S_1^\nu)^2 + (S_2^\nu)^2\right) \tag{B.1}$$

This appendix has two parts: the first part, I will calculate the energy spectrum in the strong coupling limit, where $J \gg |D|$, to determine the change in the critical field for $\nu = z$ relative to $\nu = x$; in the second part, I will do the exact calculation of the energy spectrum for all values of $J/|D|$ for $\nu = z$, and use the energy spectrum to numerically determine the heat capacity for a range of exchange values J. These calculations rely heavily on the Clebsch-Gordon coefficients for two $S = 1$ spins (Fig. 2.4).

B.1 Strong Coupling Limit

H_{c1}, the critical field determining the onset of the singlet-triplet ordered state, is set by the exchange within a dimer, the exchange between dimers and zero field splitting. Neither the intradimer exchange nor the interdimer exchanges depend on field

direction. However, the zero field splitting does change depending on field direction relative to the crystalline easy axis anisotropy. In this section I determine the zero field splitting for two fields oriented along the c and a crystalline axes. These calculations are done in the dimer basis in the strong coupling limit where the intradimer exchange is much larger than the zero field splitting, $J_0 \gg |D|$, treating the zero field splitting as a perturbation on the intradimer exchange. The calculations neglect interactions between dimers, which enter the final form of H_{c1} but do not vary based on field direction independent of the zero field splitting. First I calculate the splitting for fields along the c axis and then I calculate the splitting for fields along a axis.

B.1.1 Fields along the c axis

For fields along the crystalline c axis, and by extension the quantization z axis along the c axis, the zero field splitting takes the following form: $\langle lm|D\left((S_1^z)^2+(S_2^z)^2\right)|lm\rangle$. The calculations for each of the dimers are done by determining the individual spin states forming each dimer state, yielding the following values:

$$\begin{aligned}
\langle 22|D\left((S_1^z)^2+(S_2^z)^2\right)|22\rangle &= 2D & \langle 21|D\left((S_1^z)^2+(S_2^z)^2\right)|21\rangle &= D \\
\langle 20|D\left((S_1^z)^2+(S_2^z)^2\right)|20\rangle &= \frac{2D}{3} & \langle 2\bar{1}|D\left((S_1^z)^2+(S_2^z)^2\right)|2\bar{1}\rangle &= D \\
\langle 2\bar{2}|D\left((S_1^z)^2+(S_2^z)^2\right)|2\bar{2}\rangle &= 2D & \langle 11|D\left((S_1^z)^2+(S_2^z)^2\right)|11\rangle &= D \\
\langle 10|D\left((S_1^z)^2+(S_2^z)^2\right)|10\rangle &= 2D & \langle 1\bar{1}|D\left((S_1^z)^2+(S_2^z)^2\right)|1\bar{1}\rangle &= D \\
\langle 00|D\left((S_1^z)^2+(S_2^z)^2\right)|00\rangle &= \frac{4D}{3} & &
\end{aligned} \tag{B.2}$$

Thus the $S^z=\pm 1$ triplet states have a gap of $|D|$ to the $S^z=0$ triplet state at zero field, and the zero field gap between the singlet and the $|1\pm 1\rangle$ states is $J_0-D/3$. The full energy spectrum as a function of field for fields along the c axis is shown in Figure B.1, with the $|00\rangle$, $|10\rangle$, $|1\pm 1\rangle$ and $|2m\rangle$ states shown in red, dashed green, solid green and blue, respectively.

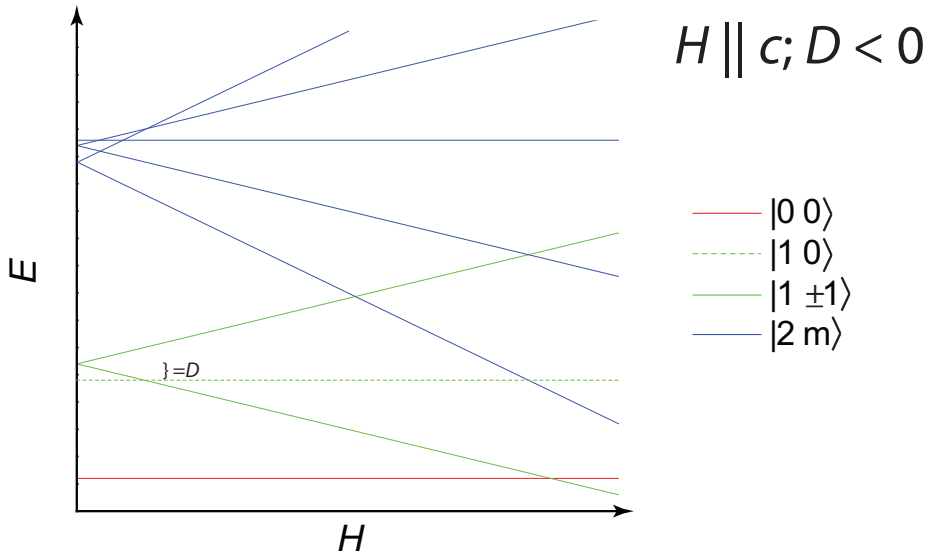

Figure B.1: Energy spectrum versus field for fields applied along the c axis in the strong coupling limit.

B.1.2 Fields along the a axis

For fields along the crystalline a axis, and by extension the quantization z axis along the a axis, the zero field splitting takes the following form: $\langle lm|D\left((S_1^x)^2+(S_2^x)^2\right)|lm\rangle$. The calculations for each of the dimers are done by determining the individual spin states forming each dimer state, converting the S^x operators into S^+ and S^- operators, yielding the following values:

$$\begin{aligned}
\langle 22|D\left((S_1^x)^2+(S_2^x)^2\right)|22\rangle &= D & \langle 21|D\left((S_1^x)^2+(S_2^x)^2\right)|21\rangle &= \frac{3D}{2} \\
\langle 20|D\left((S_1^x)^2+(S_2^x)^2\right)|20\rangle &= \frac{5D}{3} & \langle 2\bar{1}|D\left((S_1^x)^2+(S_2^x)^2\right)|2\bar{1}\rangle &= \frac{3D}{2} \\
\langle 2\bar{2}|D\left((S_1^x)^2+(S_2^x)^2\right)|2\bar{2}\rangle &= D & \langle 11|D\left((S_1^x)^2+(S_2^x)^2\right)|11\rangle &= \frac{3D}{2} \\
\langle 10|D\left((S_1^x)^2+(S_2^x)^2\right)|10\rangle &= D & \langle 1\bar{1}|D\left((S_1^x)^2+(S_2^x)^2\right)|1\bar{1}\rangle &= \frac{3D}{2} \\
\langle 00|D\left((S_1^x)^2+(S_2^x)^2\right)|00\rangle &= \frac{4D}{3} & & \qquad \text{(B.3)}
\end{aligned}$$

An important sign of the validity of these results is that the energy of the singlet state does not change based on quantization axis. An additional check on these results is that the sum of the energies of the three triplet states is the same as for the other quantization direction, even though each individual term is different. This equivalence is required because the three triplet states span the same state space regardless of quantization direction.

The zero field gap between the $|10\rangle$ state and the $|1 \pm 1\rangle$ states changes sign from positive to negative. Additionally, the zero field gap between the singlet and the $|1 \pm 1\rangle$ states is $J_0 + D/6$, confirming the functional form of the gap used in fitting for H_{c1} in section 5.2. The full energy spectrum as a function of field for fields along the a axis is shown in Figure B.2, with the $|00\rangle$, $|10\rangle$, $|1 \pm 1\rangle$ and $|2m\rangle$ states shown in red, dashed green, solid green and blue, respectively.

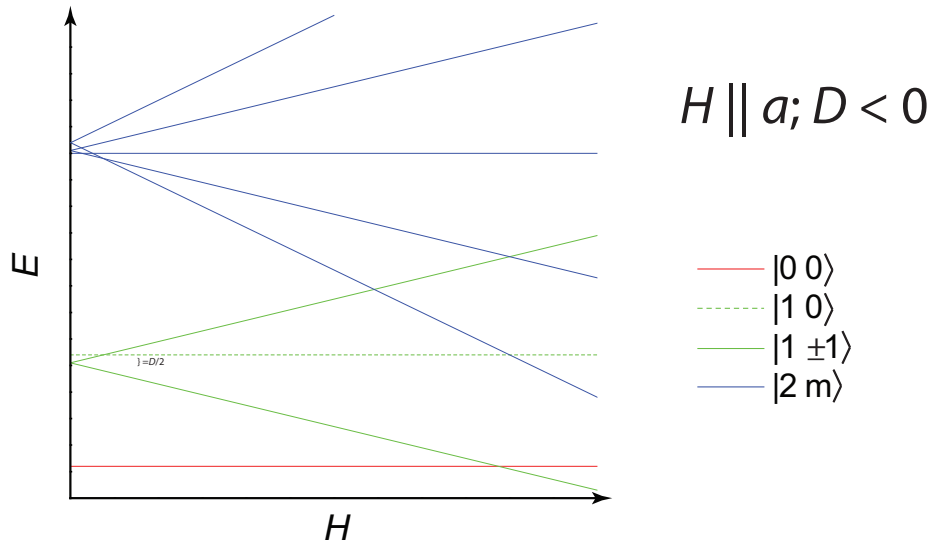

Figure B.2: Energy spectrum versus field for fields applied along the a axis in the strong coupling limit.

Although the splitting between the doublet and singlet of the triplet states changes sign depending on quantization axis it is important to note than *none* of the zero field properties of this system will change.

B.2 Exact Energy Spectrum

In the random singlet model used in chapter 7, the heat capacity is solved for at several different values of the exchange J. To solve for these heat capacities the exact energy spectrum as a function of the size of the exchange must be known. The strong coupling limit, used in the first section of this appendix chapter, assumed that $J \gg |D|$. The random singlet model, however, uses a wide range of J values, from $J \gg |D|$, to $J \sim |D|$ and $J \ll |D|$. In this section I derive the exact energy spectrum of the random singlet model Hamiltonian (Eq. B.1) as a function of the ratio of the exchange value divided by the single ion anisotropy, $J/|D|$. This calculation is not a perturbation on the dimer states, as the first section of appendix was. Once the functional form of the energy has been solved I will plot the resulting heat capacity curves for specific $J/|D|$ values.

The energy spectrum for this system is most easily determined initially in the dimer basis, with the z quantization axis along the crystalline c axis. In this case, all the dimer states are diagonal with the first term of the Hamiltonian, $J(r)\mathbf{S}_i \cdot \mathbf{S}_j$. Further, the single ion anisotropy term $D(S_i^z)^2$ must conserve total S^z and cannot connect states of opposite symmetry, implying that only the $|00\rangle$ and $|20\rangle$ states can have off-diagonal matrix elements [30]. The matrix elements for all the states are:

$$\begin{aligned}
\mathcal{H}|20\rangle &= \left(3J + \frac{2D}{3}\right)|20\rangle + \frac{2\sqrt{2}D}{3}|00\rangle \\
\mathcal{H}|00\rangle &= \frac{2\sqrt{2}D}{3}|20\rangle + \frac{4D}{3}|00\rangle \\
\mathcal{H}|2 \pm 2\rangle &= (3J + 2D)|2 \pm 2\rangle \\
\mathcal{H}|2 \pm 1\rangle &= (3J + D)|2 \pm 1\rangle \\
\mathcal{H}|1 \pm 1\rangle &= (J + D)|1 \pm 1\rangle \\
\mathcal{H}|10\rangle &= (J + 2D)|10\rangle
\end{aligned} \tag{B.4}$$

The energy eigenvalues for the non-diagonal components is solved by taking the determinant of for those two states (here the basis is $[|00\rangle, |20\rangle]$):

$$\begin{pmatrix} \frac{4D}{3} - \lambda & \frac{2\sqrt{2}2D}{3} \\ \frac{2\sqrt{2}2D}{3} & 3J + \frac{2D}{3} - \lambda \end{pmatrix}$$

The resulting energy eigenvalues are:

$$S^{\pm} = \frac{1}{2}\left(2D + 3J \pm \sqrt{(2D+3J)^2 - 16DJ}\right) \tag{B.5}$$

. and the resulting eigenvectors are:

$$\begin{aligned} |S^+\rangle &= \sin(\theta)|00\rangle + \cos(\theta)|20\rangle \\ |S^-\rangle &= \cos(\theta)|00\rangle - \sin(\theta)|20\rangle \\ \tan(\theta) &= \frac{4\sqrt{2}D}{6J - 6D + \sqrt{(2D+3J)^2 - 16DJ}} \end{aligned} \tag{B.6}$$

A few limits can simplify these expressions. Consider first the strong coupling limit ($J \gg |D|$):

$$\begin{aligned} \lim_{J/|D|\to\infty} S^+ = 3J + \frac{2D}{3} \qquad & \lim_{J/|D|\to\infty} |S^+\rangle = |20\rangle \\ \lim_{J/|D|\to\infty} S^- = \frac{4D}{3} \qquad & \lim_{J/|D|\to\infty} |S^-\rangle = |00\rangle \end{aligned} \tag{B.7}$$

These eigenvalues and eigenvectors match those shown in the first section of this appendix. Now consider the isolated moment limit ($J \to 0$):

$$\begin{aligned} \lim_{J\to 0} S^+ = 0 \qquad & \lim_{J/|D|\to\infty} |S^+\rangle = -\sqrt{\frac{1}{3}}|00\rangle + \sqrt{\frac{2}{3}}|20\rangle \\ \lim_{J\to\infty} S^- = 2D \qquad & \lim_{J/|D|\to\infty} |S^-\rangle = \sqrt{\frac{2}{3}}|00\rangle + \sqrt{\frac{1}{3}}|20\rangle \end{aligned} \tag{B.8}$$

These two states reach intuitive limits when written in terms of the original spin states. In particular, $|S^+\rangle$ is composed of two $S^z = 0$ spins while $|S^-\rangle$ is composed of the symmetric combination of an $S^z = 1$ spin on one half of the dimer and an $S^z = -1$ on the other half of the dimer.

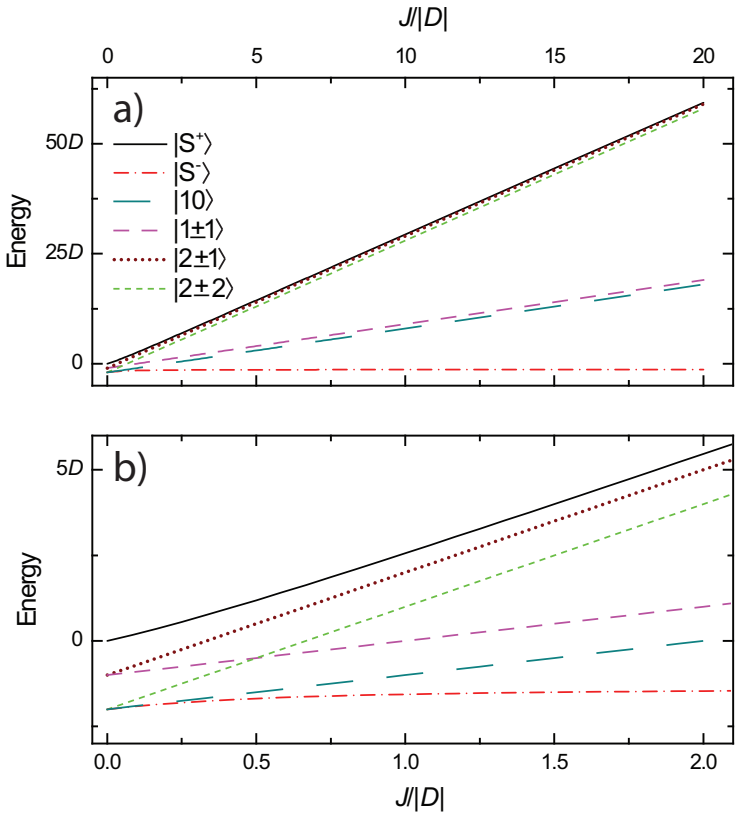

Figure B.3: Energy spectrum versus J, normalized by the single ion anisotropy $|D|$. Large $J/|D|$ range and small $J/|D|$ range shown in (a) and (b), respectively.

The energy spectrum is plotted versus the size of the exchange $J/|D|$ in Figure B.3. Panel (a) shows the spectrum for large values of $J/|D|$. In this limit the system approaches the isolated dimer model, where the singlet has gaps of J and $3J$ to the excited triplet and quintuplet states, respectively. Panel (b) shows the spectrum for small values of $J/|D|$. In this limit the system approaches the isolated moment model, where a dimer has total energy 0, D or $2D$ if it composed of two, one or zero $S^z = 0$ spins, respectively.

The energy for a pair of moments with exchange J can be easily calculated as a function of temperature:

$$E_J(T) = \frac{\sum_i E_{|M_i\rangle} e^{-\beta E_{|M_i\rangle}}}{\sum_i e^{-\beta E_{|M_i\rangle}}} \tag{B.9}$$

Here, the summation runs over all the different basis states ($|M_i\rangle = |S^{\pm}\rangle, |2 \pm 2\rangle, |2 \pm$

$1\rangle, |1\pm1\rangle, |20\rangle)$, $E_{|M_i\rangle}$ is the energy of a given state and $\beta = 1/k_BT$. The heat capacity for a pair of moments with exchange J is easily calculated from the energy:

$$C_p(J,T) = \frac{d(E_J(T))}{dT} \tag{B.10}$$

Several different heat capacity curves for a range of $J/|D|$ values are plotted on a log scale in Figure B.4. For $J = 0$ (solid black line), the system reduces to the isolated moment case and the heat capacity has a peak induced by the two gaps of the single ion anisotropy (a gap of $|D|$, $2|D|$ between the $|S^-\rangle, |10\rangle, |2 \pm 2\rangle$ ground states and the $|2 \pm 1\rangle, |1 \pm 1\rangle$ first excited states and $S^+\rangle$ second excited states, respectively). For the largest J values of $J = 30|D|, 10|D|$ and $3|D|$ (blue, orange and teal lines, respectively) there is a single peak centered at roughly $0.4J$ arising from both the singlet-triplet and singlet-quintuplet gaps. For $J = |D|$ (red line), there is a single peak with a shoulder at lower temperatures. For $J = 0.3|D|$ (green line) there are split peaks, one centered roughly at the same position as the single ion anisotropy peak and a second at lower temperature. Finally for the smallest non-zero J values of $J = 0.1|D|$ and $0.03|D|$ (magenta and gray lines, respectively) there are three peaks stemming from three gaps from the $|S^-\rangle$ groundstate: the gap to the first excited state, $|10\rangle$; the gap to the second excited states $|2 \pm 2\rangle$; and finally the single ion anisotropy gap to the third excited states, $|1 \pm 1\rangle, |2 \pm 1\rangle$ and $|S^+\rangle$. The model shown in Figs. 7.7 and 7.8 used a superposition of heat capacity curves taken from exchange values mostly within this range. The different model curves used differently weighted superpositions, such that the higher (lower) vanadium concentrations are weighted more towards larger (smaller) J values based on the probability distributions $P_x(J(r))$.

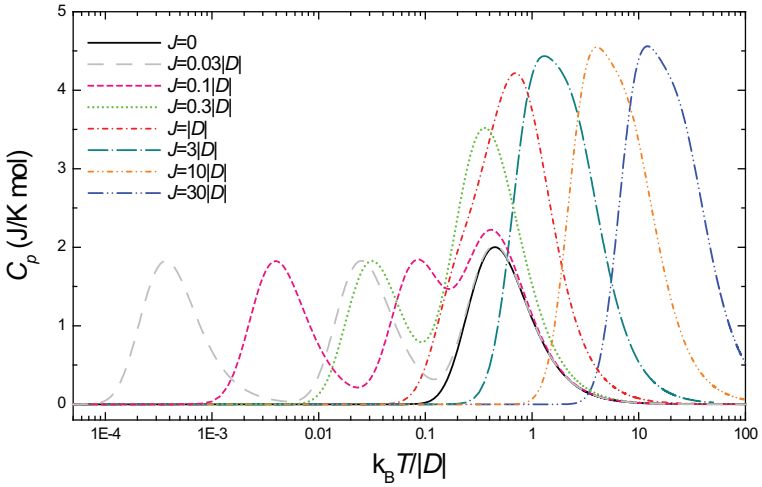

Figure B.4: Heat capacity curves versus normalized temperature for specific $J/|D|$ values plotted on a log scale. Mol refers to one mole of spins.

Appendix C

$Ba_3((Mn_{1-}x)V_x)_2O_8$ in singlet-triplet regime

In chapter 7, I presented studies of the low field properties of the diluted compound $Ba_3(Mn_{1-x}V_x)_2O_8$. I also performed heat capacity and magnetocaloric effect measurements of the high field behavior of this compound. These measurements revealed unexpected behavior, including new transitions that I will discuss in this appendix. Further measurements will be required to determine the exact nature of these new transitions.

Extensive quantum Monte Carlo studies have been performed on a spin dimer system based on a square lattice of $S = \frac{1}{2}$ spins which have been diluted with non-magnetic $S = 0$ sites [58, 59]. Those calculations found that at 0 K, in addition to the Bose-Einstein condensate ordered state (canted antiferromagnetic order) observed in the undiluted system, a Bose glass state arises in certain field ranges. The expected glass states occurs symmetrically at low and high triplet densities, i.e. for fields just above H_{c1} and fields just below H_{c2}. The field extent of the Bose glass increases with doping until a critical concentration at which long range order disappears. However, there have not been any extensive studies of a diluted spin system at high fields. In this section I present the first extensive studies of the high field properties of a diluted spin dimer system, including both heat capacity and MCE results.

Heat capacity and MCE measurements of single crystals of $Ba_3(Mn_{1-x}V_x)_2O_8$

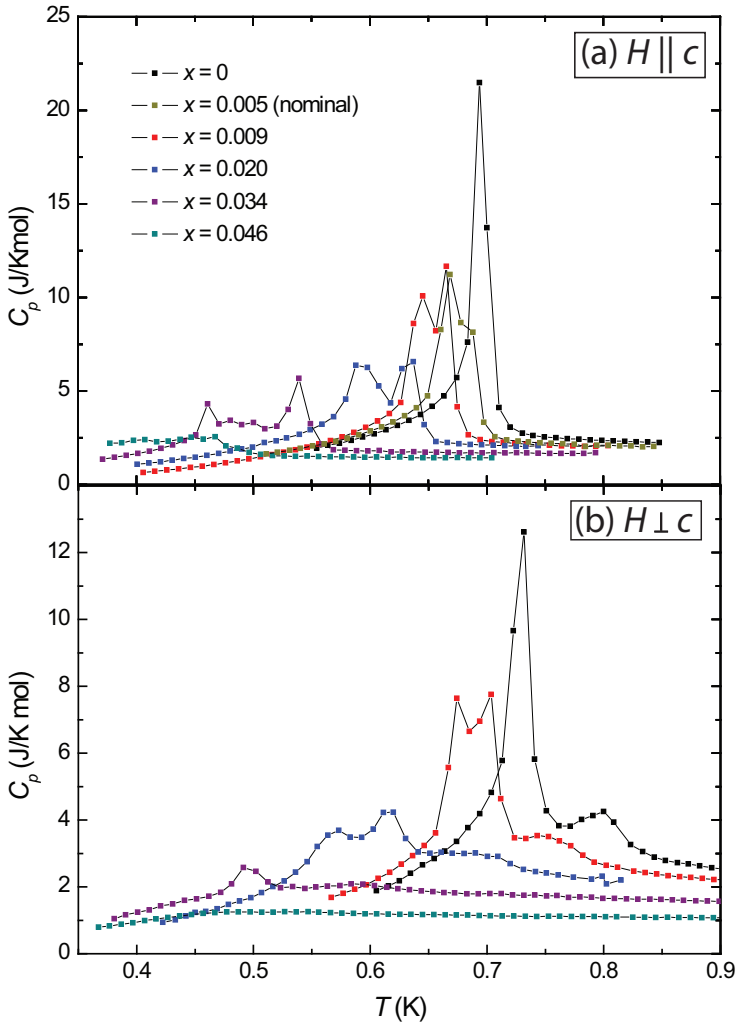

Figure C.1: Heat Capacity of $Ba_3(Mn_{1-x}V_x)_2O_8$ at 13 T for fields applied both parallel (a) and perpendicular (b) to the c axis.

were performed in a commercial PPMS calorimeters in fields both parallel and perpendicular to the c axis between 10 T and 14 T in both a ^{3}He refrigerator down to 0.35 K and a dilution refrigerator down to 50 mK. These measurements revealed both strong evidence of a splitting of the λ-like transition into phase I and at a minimum a broadening, if not a splitting, of the transition into Ising-like phase II.

Heat capacity measurements for fields along the c axis taken at 13 T for several different vanadium concentrations are presented in Figure C.1(a). The curve with $x = 0$, shown in black, reveals a single sharp transition at 0.694 K. As vanadium concentration increases, the single sharp peak broadens and splits into two peaks at lower temperatures. The critical temperatures of the two peaks in the $x = 0.020$ sample are 0.593 K and 0.635 K. The height of the transitions decreases as doping increases, although because the transitions also broaden it is unclear whether the total entropy under the transitions changes with doping.

Heat capacity measurements for fields perpendicular to the c axis taken at 13 T for several different vanadium concentrations are shown in Figure C.1(b). The undiluted sample showed two transitions, a Ising-like transition into phase II at 0.800 K and a λ-like transition at 0.732 K into phase I. As x increases these transitions broaden as observed for fields along the c axis. The λ-like transition evolves into two transitions, such that in $x = 0.020$ sample the split transitions are at 0.573 K and 0.615 K. However, the Ising-like transition broadens but does not split into two separate peaks, making identification of the critical field for this transition difficult.

Magnetocaloric effect measurements of the $x = 0.020$ sample for fields parallel and perpendicular to the c axis are shown in Figure C.2(a) and (b), respectively. Both of these measurements exhibited temperature independent features at H_{c1} arising from the same Maxwell's relation which induced equivalent features in the undiluted copmound. Split transitions are observed for fields parallel to the c axis, in accordance with the heat capacity data. Phase transitions, determined from peaks in the field derivative of the temperature in the same manner as done with the undiluted samples, are marked with open circles. For fields perpendicular to the c axis, multiple rapid rises and falls of the temperature were observed, indicative of the split λ-transition and broadened Ising transition observed in heat capacity measurements.

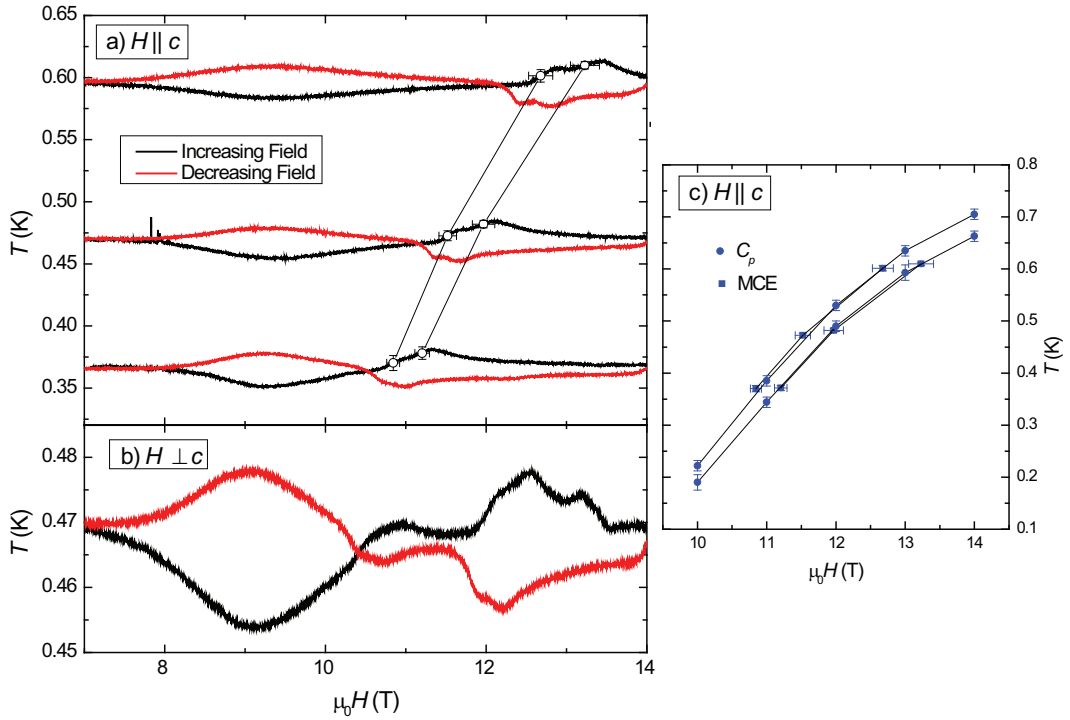

Figure C.2: MCE measurements of $Ba_3(Mn_{0.980}V_{0.020})_2O_8$ for fields applied both parallel (a) and perpendicular (b) to the c axis. Open circles mark phase transitions. c) Phase diagram for x=0.020 sample for fields parallel to the c axis determined from heat capacity (circles) and MCE (squares).

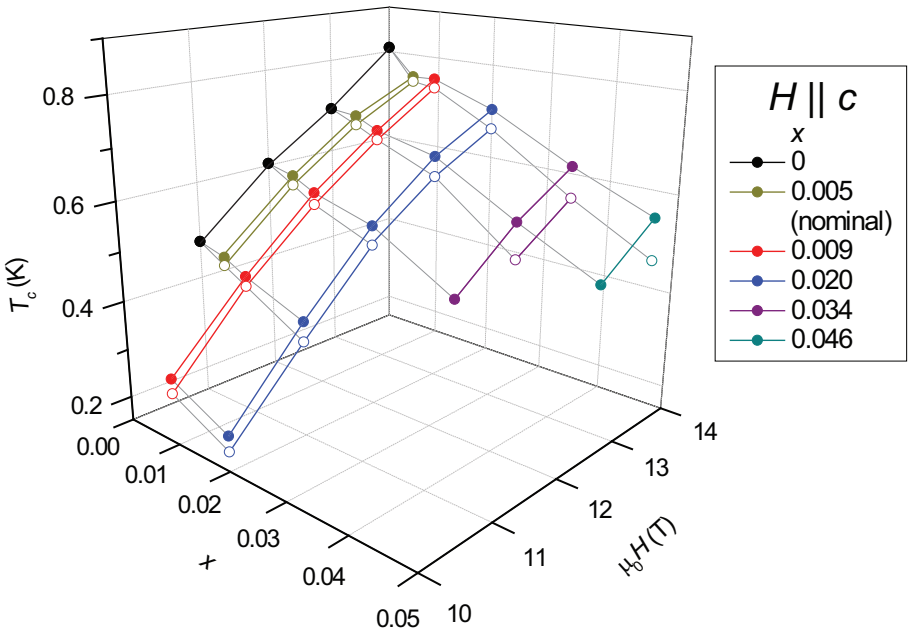

Figure C.3: Phase diagram determined for fields parallel to c determined from heat capacity.

However, ambiguity in the choice of the appropriate feature in the field derivative of the temperature made identification of the transitions difficult.

The phase diagram of the $x = 0.020$ sample for fields parallel to the c axis determined from both heat capacity and MCE is presented in Figure C.2(c). The splitting between the transitions, which is independent of field, is 45 mK. Unfortunately, determining the phase diagram for fields perpendicular to the c axis is much more difficult because the positions of the critical fields and critical temperatures in both the heat capacity and MCE measurements are ambiguous due to the broadness of the critical features. The full phase diagram of critical temperature versus both field and vanadium concentration for fields along the c axis determined from heat capacity is presented in Figure C.3. The splitting between the transitions, which is field independent, increases with vanadium concentration, while the critical temperatures decrease with vanadium concentration.

The heat capacity presents no evidence at temperatures above the phase transitions of Bose glass like behavior, which would exhibit a slow removal of entropy

without any sharp features. Further experiments will be necessary to determine the nature of the additional high field magnetic phases induced by disorder in this material.

Bibliography

[1] T. Matsubara and H. Matsuda *Prog. Theor. Phys.*, vol. 16, p. 416, 1956.

[2] T. M. Rice *Science*, vol. 298, p. 760, 2002.

[3] S. E. Sebastian, N. Harrison, P. Sengupta, C. D. Batista, S. Francoual, E. Palm, T. Murphy, N. Marcano, H. A. Dabkowska, and B. D. Gaulin *P. Natl. Acad. Sci. USA*, vol. 105, p. 20157, 2008.

[4] K. Kodama, M. Takigawa, M. Horvatić, C. Berthier, H. Kageyama, Y. Ueda, S. Miyahara, F. Becca, and F. Mila *Science*, vol. 298, p. 395, 2002.

[5] T. Nikuni, M. Oshikawa, A. Oosawa, and H. Tanaka *Phys. Rev. Lett.*, vol. 84, p. 5868, 2000.

[6] C. Rüegg, N. Cavadini, A. Furrer, H.-U. Güdel, K. Krämer, H. Mutka, A. Wildes, K. Habicht, and P. Vorderwisch *Nature (London)*, vol. 423, p. 62, 2003.

[7] C. Rüegg, A. Furrer, D. Sheptyakov, T. Strässle, K. W. Krämer, H.-U. Güdel, and L. Mélési *Phys. Rev. Lett.*, vol. 93, p. 257201, 2004.

[8] F. Yamada, T. Ono, H. Tanaka, G. Misguich, M. Oshikawa, and T. Sakakibara vol. 77, p. 013701, 2008.

[9] T. Giamarchi, C. Rüegg, and O. Tchernyshyov *Nat. Phys.*, vol. 4, p. 198, 2008.

[10] Y. Sassago, K. Uchinokura, A. Zheludev, and G. Shirane *Phys. Rev. B*, vol. 55, p. 8357, 1997.

[11] M. Jaime, V. F. Correa, N. Harrison, C. D. Batista, N. Kawashima, Y. Kazuma, G. A. Jorge, R. Stern, I. Heinmaa, S. A. Zvyagin, Y. Sasago, and K. Uchinokura *Phys. Rev. Lett.*, vol. 93, p. 087203, 2004.

[12] S. E. Sebastian, P. Tanedo, P. A. Goddard, S.-C. Lee, A. Wilson, S. Kim, S. Cox, R. D. McDonald, S. Hill, N. Harrison, C. D. Batista, and I. R. Fisher *Phys. Rev. B*, vol. 74, p. 180401(R).

[13] S. E. Sebastian, N. Harrison, C. D. Batista, L. Balicas, M. Jaime, P. A. Sharma, N. Kawashima, and I. R. Fisher *Nature*, vol. 441, p. 617, 2006.

[14] P. Sengupta and C. D. Batista *Phys. Rev. Lett.*, vol. 98, p. 227201, 2007.

[15] P. W. Anderson *Mat. Res. Bull.*, vol. 8, p. 153, 1973.

[16] T. Jolicœur and J. C. Leguillou *Phys. Rev. B*, vol. 40, p. 2727, 1989.

[17] B. Bernu, P. Lecheminant, C. Lhullier, and L. Pierre *Phys. Rev. B*, vol. 50, p. 10048, 1994.

[18] H. T. Diep, ed., *Frustrated Spin Systems*. Singapore: World Scientific, 2005.

[19] M. T. Weller and S. J. Skinner *Acta Crystallogr., Sect. C: Cryst. Struct. Commun.*, vol. 55, p. 154, 1999.

[20] K. Inoue and H. Iwamura *Angew. Chem. Int. Ed. Engl.*, vol. 34, p. 927, 1995.

[21] Y. Hosokoshi, Y. Nakazawa, K. Inoue, K. Takizawa, H. Nakano, M. Takahashi, and T. Goto *Phys. Rev. B*, vol. 60, p. 12924, 1999.

[22] H. Tusjii, B. Andraka, Y. Hosokoshi, K. Inoue, and Y. Takano *J. Magn. Magn. Mater.*, vol. 310, p. e415, 2007.

[23] M. Uchida, H. Tana, M. Bartashevich, and T. Goto *J. Phys. Soc. Jpn.*, vol. 70, p. 1790, 2001.

[24] M. Uchida, H. Tanaka, H. Mitamura, F. Ishikawa, and T. Goto *Phys. Rev. B*, vol. 66, p. 054429, 2002.

[25] H. Tsujii, B. Andraka, M. Uchida, H. Tanaka, and Y. Takano *Phys. Rev. B*, vol. 72, p. 214434, 2005.

[26] M. B. Stone, M. D. Lumsden, Y. Qiu, E. C. Samulon, C. D. Batista, and I. R. Fisher *Phys. Rev. B*, vol. 77, p. 134406, 2008.

[27] M. B. Stone, M. D. Lumsden, S. Chang, E. C. Samulon, C. D. Batista, and I. R. Fisher *Phys. Rev. Lett.*, vol. 100, p. 237201, 2008.

[28] M. B. Stone, M. D. Lumsden, S. Chang, E. C. Samulon, C. D. Batista, and I. R. Fisher *Phys. Rev. Lett.*, vol. 105, p. 169901(E), 2010.

[29] E. C. Samulon, Y.-J. Jo, P. Sengupta, C. D. Batista, M. Jaime, L. Balicas, and I. R. Fisher *Phys. Rev. B*, vol. 77, p. 214441, 2008.

[30] E. C. Samulon, Y. Kohama, R. D. McDonald, M. C. Shapiro, K. A. Al-Hassanieh, C. D. Batista, M. Jaime, and I. R. Fisher *Phys. Rev. Lett*, vol. 103, p. 047202, 2009.

[31] E. C. Samulon, K. A. Al-Hassanieh, Y.-J. Jo, M. C. Shapiro, L. Balicas, C. D. Batista, and I. R. Fisher *Phys. Rev. B*, vol. 81, p. 104421, 2010.

[32] E. C. Samulon, M. C. Shapiro, and I. R. Fisher arXiv:1011.6423.

[33] S. Suh, K. A. Al-Hassanieh, E. C. Samulon, J. S. Brooks, W. G. Clark, P. L. Kuhns, L. L. Lumata, A. Reyes, I. R. Fisher, S. E. Brown, and C. D. Batista arXiv:0905.0718.

[34] M. B. Stone, A. Podlesnyak, G. Ehlers, A. Huq, E. C. Samulon, M. C. Shapiro, and I. R. Fisher arXiv:1012.0099.

[35] M. H. Whitmore, H. R. Verdún, and D. Singel *Phys. Rev. B*, vol. 47, p. 11479, 1993.

[36] S. Hill private communication.

[37] M. Tachiki and T. Yamada *J. Phys. Soc. Jpn.*, vol. 28, p. 1413, 1970.

[38] F. Mila *Eur. Phys. J. B*, vol. 6, p. 201, 1998.

[39] T. Giamarchi and A. M. Tsvelik *Phys. Rev. B*, vol. 59, p. 11398, 1999.

[40] B. M. Wanklyn in *Crystal Growth (Int. Ser. Monogr. Sci. Solid State.)* (B. R. Pamplim, ed.), Oxford: Pergamon Press, 1974.

[41] www.magnet.fsu.edu.

[42] J. C. Lashley, M. F. Hundley, A. Migliori, J. L. Sarrao, P. G. Pagliuso, T. W. Darling, M. Jaime, J. C. Cooley, W. L. Hults, L. Morales, D. J. Thoma, J. L. Smith, J. Boerio-Goates, B. F. Woodfield, G. R. Stewart, R. A. Fisher, and N. E. Phillips *Cryogenics*, vol. 43, p. 369, 2003.

[43] G. M. Schmiedeshoff, A. W. Lounsberry, D. J. Luna, S. J. Tract, A. J. Schramm, S. W. Tozer, V. F. Correa, S. T. Hannahs, T. P. Murphy, E. C. Palm, A. H. Lacera, S. L. Bud'ko, P. C. Canfield, J. L. Smith, J. C. Lashley, and J. C. Cooley *Rev. Sci. Instr.*, vol. 77, p. 123907, 2006.

[44] D. Hall, *Magnetic Measurements with Metal Film Cantilever: A User's Guide*. National High Magnetic Field Laboratory, 1999.

[45] S. E. Sebastian. PhD thesis, Stanford University, 2006.

[46] J. A. Detwiler, G. M. Schmiedeshoff, N. Harrison, A. H. Lacerda, J. C. Cooley, and J. L. Smith *Phys. Rev. B*, vol. 61, p. 402, 2000.

[47] S. E. Sebastian, P. A. Sharma, M. Jaime, N. Harrison, V. Correa, L. Balicas, N. Kawashima, C. D. Batista, and I. R. Fisher *Phys. Rev B*, vol. 72, p. 100404(R), 2005.

[48] K. A. Al-Hassanieh and C. D. Batista In preparation.

[49] C. D. Batista private communication.

[50] M. B. Stone and M. D. Lumsden private communication.

[51] S. Blundell, *Magnetic in Condensed Matter*. Oxford University Press, 2001.

[52] S. T. Beliaev *Zh. Éksp. Teor. Fiz.*, vol. 34, p. 433, 1958. [Sov. Phys. JETP **7**, 299 (1958)].

[53] A. Oosawa, T. Ono, and H. Tanaka *Phys. Rev. B*, vol. 66, p. 020405, 2002.

[54] J. A. Mydosh, *Spin Glasses: An Experimental Introduction*. London: Taylor and Francis, 1993.

[55] S. B. Oseroff, S.-W. Cheong, B. Atkas, M. F. Hundley, Z. Fisk, and J. L. W. Rupp *Phys. Rev. Lett.*, vol. 74, p. 1450, 1995.

[56] T. Masuda, A. Fujioka, Y. Uchiyama, I. Tsukada, and K. Uchinokura *Phys. Rev. Lett.*, vol. 80, p. 4566, 1998.

[57] S. Ohsugi, Y. Tokunaga, K. Ishida, Y. Kitaoka, M. Azuma, Y. Fujishiro, and M. Takano *Phys. Rev. B*, vol. 60, p. 4181, 1999.

[58] T. Roscilde and S. Haas *Phys. Rev. Lett.*, vol. 95, p. 207206, 2005.

[59] T. Roscilde *Phys. Rev. B*, vol. 74, p. 144418, 2006.

[60] S. Manna, S. Majumder, and S. K. De *J. Phys.: Condens. Matter*, vol. 21, p. 236005, 2009.

[61] L. E. Wenger and P. H. Keesom *Phys. Rev. B*, vol. 13, p. 4053, 1976.

[62] D. L. Martin *Phys. Rev. B*, vol. 21, p. 1902, 1980.

[63] S. K. Ma, C. Dasgupta, and C. K. Hu *Phys. Rev. Lett.*, vol. 43, p. 1434, 1979.

[64] R. N. Bhatt and P. A. Lee *Phys. Rev. Lett.*, vol. 48, p. 344, 1982.

[65] R. N. Bhatt and D. S. Fisher *Phys. Rev. Lett.*, vol. 68, p. 3072, 1992.

[66] K. Andres, R. N. Bhatt, P. Goalwin, T. M. Rice, and R. E. Walstedt *Phys. Rev. B*, vol. 24, p. 244, 1981.

[67] R. B. Kummer, R. E. Walstedt, V. Narayanamurti, and G. E. Devlin *Phys. Rev. Lett.*, vol. 40, p. 1098, 1978.

[68] M. Lakner and H. v. Löhneysen *Phys. Rev. Lett.*, vol. 63, p. 648, 1989.

[69] D. S. Fisher *Phys. Rev. B*, vol. 50, p. 3799, 1994.

[70] J. C. Fernandes, R. B. Guimarães, M. A. Continentino, H. A. Borges, J. V. Valarelli, and A. Lacerda

[71] M. A. Continentino, B. Boechat, R. B. Guimarães, J. C. Fernandes, and L. Ghivelder *J. Magn. Magn. Mater.*, vol. 226-230, p. 427, 2001.

[72] J. C. Fernandes, F. S. Sarrat, R. B. Guimarães, R. S. Freitas, M. A. Continentino, A. C. Doriguetto, Y. P. Mascarenhas, J. Ellena, E. E. Castellano, J.-L. Tholence, J. Dumas, and L. Ghivelder vol. 67, p. 104413, 2003.

[73] C. Monthus, O. Golinelli, and T. Jolicœur *Phys. Rev. Lett.*, vol. 79, p. 3254, 1997.

[74] A. Saguia, B. Boechat, and M. A. Continentino *Phys. Rev. Lett.*, vol. 89, p. 117202.

[75] M. Fujisawa, T. Ono, H. Fujiwara, H. Tanaka, V. Sikolenko, M. Meissner, P. Smeibidl, S. Gerischer, and H. A. Graf *J. Phys. Soc. Jpn.*, vol. 75, p. 033702, 2006.

[76] H.-J. Mikeska, A. Ghosh, and A. K. Kolezhuk *Phys. Rev. Lett.*, vol. 93, p. 217204, 2004.

[77] T. Kato, K. Takatsu, H. Tanaka, W. Shiramura, M. Mori, K. Nakajima, and K. Kakurai *J. Phys. Soc. Jpn.*, vol. 67, p. 752, 1998.

[78] N. Cavadini, W. Henggeler, A. Furrer, H.-U. Güdel, K. Krämer, and H. Mutka *Eur. Phys. J. B*, vol. 7, p. 519, 1999.

[79] N. Cavadini, G. Heigold, W. Henggeler, A. Furrer, H.-U. Güdel, K. Krämer, and H. Mutka *Phys. Rev. B*, vol. 63, p. 172414, 2002.